Influence of particle size and morphology of Pt_3Co/C on the oxygen reduction reaction

Dissertation

University of Cape Town

Prepared for:

Dr Pieter Levecque

Dr Bernard Schwanitz

Department of Chemical Engineering

Centre for Catalysis Research

National Hydrogen Catalysis Competence Centre

University of Cape Town

Prepared by:

Ntandoyenkosi Hlabangana

August 2015

The copyright of this thesis vests in the author. No quotation from it or information derived from it is to be published without full acknowledgement of the source. The thesis is to be used for private study or non-commercial research purposes only.

Published by the University of Cape Town (UCT) in terms of the non-exclusive license granted to UCT by the author.

University of Cape Town

Abstract

Polymer electrolyte fuel cells have shown great potential in providing clean energy with no emissions. The kinetics of the cathode reaction, i.e. the oxygen reduction reaction (ORR) are sluggish necessitating high loadings of the catalyst metal, i.e. platinum. Platinum is a limited resource and expensive. Its price has been one of the major drawbacks in wide scale commercialisation of fuel cells. In an effort to improve the activity of the catalyst and therefore reduce Pt loadings on the catalyst, Pt can be alloyed with transition metal elements (e.g. Ni, Co and Fe) to form bimetallic catalysts. Alloying has been known to improve the activity and stability of a catalyst for the ORR. The enhanced activity of the alloys originates from the modified electronic structures of the Pt in these alloy catalysts which reduces the adsorption of spectator species therefore increasing the number of active sites for the ORR (Wang et al., 2012 (2)).

The aim of this study was to gain a better understanding of the influence of Pt alloy particle size and active surface morphology on the ORR activity. The Pt alloy that was investigated was Pt_3Co/C. The surface morphology was modified by varying the Pt/Pt_3Co loading on a carbon support. The catalysts were prepared using thermally induced chemical deposition. The support used was Vulcan-XC-72R. The effects of varying the metal loadings on the ORR was investigated. The loadings that were investigated were 20, 40, 60 and 80 wt. % Pt and Pt_3Co. The alloy catalysts were subjected to annealing at 900 °C and acid leaching. The catalysts were analysed using electrochemical characterisation techniques such as cyclic voltammetry, CO stripping voltammetry, rotating disk electrode and rotating ring disk electrode. Physical characterisation of the catalysts was also implemented. The techniques used were x-ray diffraction, thermogravimetric analysis and transmission electron microscopy.

The Pt particles on the carbon support were found not to agglomerate significantly despite the loading being increased. This trend was also observed for the Pt_3Co/C catalysts even after heat treatment and leaching. The lack of agglomeration was credited to a new reactor system developed in this work. The particle growth increased from low loadings to high loadings for both the Pt/C and Pt_3Co/C catalysts. Particle growth was more significant for the Pt_3Co/C catalysts at high loadings. At lower loadings (20 and 40 wt. %) the particle sizes between the Pt/C and Pt_3Co/C catalysts were comparable despite the Pt_3Co/C catalysts undergoing annealing and leaching.

The mass specific activity of the Pt/C catalysts was not improved by alloying with the exception of the 20 wt. % catalyst which saw an enhancement factor of 1.66. The surface specific activity of the Pt/C catalysts was improved significantly with factors of 2.40 and 3.11 being recorded for the 20 and 80 wt. % Pt_3Co/C catalysts respectively. The enhancement factors of the intermediate loadings (40 and 60 wt. %) were lower and fairly similar at 1.30 and 1.35 respectively.

Acknowledgements

I would not be where I am today without the support and guidance received from several key people. I owe them my sincerest gratitude.

I would like to thank Pieter, who has been the foundation on which I stand for the past 18 months. Your patience, encouragement, guidance and support steered me through my Masters. I will be forever grateful to have had a supervisor like you.

Bernard, who only came on board on my project in the final year but still took it in his stride. Thank you for all your insight and the guidance that you provided.

Archie, Colleen, and Rhiyaad, you three were my pseudo-supervisors! I cannot thank you enough for all the support you provided me throughout my Masters. Whenever I had a problem or question you always made yourselves available and assisted me in whichever way you could.

Caelin, my partner through this journey. Even though our projects were completely different we still found a way to do everything together from the beginning to the end. Thank you for being a friend, advisor and constant companion though this journey. I could not have done it without you!

Sibongile who was my late-night campus buddy, thank you for "pulling all-nighters with me", for being my coffee and oats buddy and a sympathetic ear.

Sibusiso who stayed late many a night to listen to all grumblings and frustrations, thank you for your patience, support and encouragement. You always found a way to pick me up when I low and helped me carry my burdens.

The TEM and SEM team Miranda, Mohammed and Innocent and Hong Su from XRD thank you for always availing yourselves to me and sometimes "sneaking in" some of my samples for analysis in-between appointments.

I would like to thank all my family and friends. Thank you for being understanding when I disappeared for weeks on end to focus on my work.

Lastly I would like to thank everyone from HySA Catalysis for giving me the opportunity to work with you!

"*Even to your old age and grey hairs, I am He, I am He who will sustain you, I have made you and I will carry you; I will sustain you and I will rescue you*" Isaiah 46 v 4

Table of Contents

Abstract ii
Acknowledgements iii
Glossary vii
Nomenclature viii
List of Figures ix
List of Tables xii
1. Introduction 1
2. Literature review 2
2.1. Polymer electrolyte membrane fuel cells 2
2.2. Oxygen reduction reaction catalysts 3
2.2.1. Oxygen reduction reaction mechanism 3
2.2.2. Current state of catalysts 4
2.3. Alloys 6
2.3.1. Overview 6
2.3.2. Pt–Co alloys as ORR catalyst 8
2.3.3. Leaching of cobalt 10
2.3.4. Heat treatment of alloy 11
2.4. Catalyst Durability 13
2.4.1. Corrosion mechanism and consequences 13
2.4.2. Carbon corrosion 15
2.5. Catalyst surface structure and morphology 17
2.5.1. Extended surfaces 17
2.5.2. Change in catalyst loading for Pt/Pt alloy nanoparticles 19
2.6. Electrochemical analysis techniques 20
2.6.1. Cyclic voltammetry 20
2.6.2. CO stripping voltammetry 22
2.6.3. Rotating disk electrode and rotating ring disk electrode 23
3. Objectives and Hypotheses 25
3.1. Problem statement 25
3.2. Objectives 25
3.3. Key Questions 25
4. Experimental plan 26
4.1. Thermally induced chemical deposition 26

4.2. Heat treatment 28
4.3. Leaching 28
4.4. Electrochemical characterisation 29
4.4.1. Cell setup and experiment preparation 29
4.4.2. Cyclic voltammetry 30
4.4.3. Linear sweep voltammetry (rotating disk electrode and rotating ring disk electrode) 31
4.4.4. CO stripping 33
4.5. Physical characterisation 33
4.5.1. Transmission electron microscopy 33
4.5.2. Energy-dispersive X-ray spectroscopy 34
4.5.3. Thermogravimetric analysis 34
4.5.4. X-ray diffraction 34
5. Results and discussion 35
5.1. Benchmarking 36
5.2. Thermogravimetric analyses (TGA) of precursors 38
5.3. Optimisation of ink drying methodology 40
5.4. Analyses of the Pt/C results 41
5.4.1. XRD 41
5.4.2. TEM analysis 42
5.4.3. Thermogravimetric analysis 45
5.4.4. Electrochemical characterisation 46
5.4.5. Activity of Pt/C catalysts 48
5.4.6. Rotating ring disk results 51
5.5. Analyses of the Pt_3Co/C results 52
5.5.1. Thermally induced chemical deposition of alloys 52
5.5.2. Heat treatment 53
5.5.3. XRD data for heat treated and leached Pt_3Co/C 57
5.5.4. Particle size, distribution and composition via TEM and SEM 59
5.5.5. Thermogravimetric analysis 62
5.5.6. Electrochemical characterisation 62
5.5.7. Activity of Pt_3Co/C catalysts 64
5.5.8. Rotating ring disk results 66
5.6. Summary of Pt_3Co/C and Pt/C results 66
6. Conclusions 68

7. References 69
8. Appendices 78
A1. TEM analysis of Pt_3Co/C catalyst 78

Glossary

Abbreviation	Description
PEFC	Polymer electrolyte fuel cell
CV	Cyclic voltammetry
XRD	X-ray diffraction
ECSA	Electrochemical surface area
GDL	Gas diffusion layer
MEA	Membrane electrode assembly
TEM	Transmission electron microscopy
NSTF	Nanostructured thin film
ORR	Oxygen reduction reaction
PEM	Proton exchange membrane
TGA	Thermogravimetric analysis
RDE	Rotating disk electrode
RRDE	Rotating ring disk electrode
SEM	Scanning electron microscopy
SHE	Standard hydrogen electrode
RHE	Reversible hydrogen electrode
OD	Outer diameter
EXAFS	Extended X-ray Absorption Fine Structure

Nomenclature

Symbol	Unit	Description
D	cm^2/s	Diffusion co-efficient
i	mA/cm^2	Current density
i_d	mA/cm^2	Diffusion limiting current density
i_k	mA/cm^2	Kinetic current density
$i_{k\ (0.9\ V)}$	mA/cm^2	Kinetic current density at 0.9 V vs RHE
i_{2e^-}	mA/cm^2	2 electron current density
i_{4e^-}	mA/cm^2	4 electron current density
i_{Disk}	mA/cm^2	Disk current density
i_{Ring}	mA/cm^2	Ring current density
$i_{k,\ mass}$	mA/cm^2	Mass activity
$i_{k,\ mass\ (0.9\ V)}$	mA/cm^2	Mass activity at 0.9 V vs. RHE
$i_{k,\ spec}$	mA/cm^2	Surface specific activity
$i_{k,\ spec\ (0.9\ V)}$	mA/cm^2	Surface specific activity at 0.9 V vs. RHE
<L>	nm	Average crystallite size
n	-	Number of electrons
N	%	Collection efficiency of the ring
$X_{H_2O_2}$	%	Percentage hydrogen peroxide formed on the ring relative to the total current
wt. % Pt	%	Weight percent platinum supported on carbon
wt. % Pt_3Co	%	Weight percent platinum-cobalt supported on carbon
ω	rpm	Rotation speed of the electrode
ν	cm^2/s	Kinematic viscosity
λ	nm	X-ray wavelength
Θ	radians	Bragg angle
β	-	Peak width

List of Figures

Figure 2.1: (a) Single PEM fuel cell (Adapted from Wang et al., 2011). (b) Three phase boundary in an electrode (Adapted from Litster & McLean, 2004). 2
Figure 2.2: Scheme of oxygen reduction mechanism (Yue et al., 2010). 3
Figure 2.3: Variation of the oxygen reduction activities for different metals compared to the oxygen binding energies (Nørskov et al., 2004). 5
Figure 2.4: The specific activity of Pt alloys for ORR expressed as kinetic densities (Stamenkovic et al., 2006) 7
Figure 2.5: Model of activity as a function of the adsorption energy of oxygen. The plot in red is the actual measured activity relative to that of Pt (Stamenkovic et al., 2006). 7
Figure 2.6: Interatomic distances calculated for Pt, Pt_3Co and PtCo (Chen et al., 2009) 8
Figure 2.7: Correlation between the d-band centre and the oxygen adsorption energy (Adapted from Stamenkovic et al., 2006) 9
Figure 2.8: Effect of the Pt-Pt neighbour distance on the specific activity (Min et al., 2000) 9
Figure 2.9: (a) Influence of the Co/Pt ratio on the mean particle size. (b) Correlation of oxygen electrode performance of Pt and Pt-Co catalysts with the mean interatomic distance (Adapted from Salgado et al., 2004) 10
Figure 2.10: The effect of pre-leaching Pt-Co catalysts on the dissolution of Co (Gasteiger et al., 2005) 11
Figure 2.11: Pt_3Co atomic nanoparticles. The white and blue spheres represent Pt ad Co atoms respectively (Wang et al., 2013) 11
Figure 2.12: Specific activity of low T (600 °C) and high T (950 °C) Pt_3Co at 900 mV/RHE compared to Pt/C (Koh et al., 2007) 12
Figure 2.13: Cyclic voltammetry plots comparing Pt-Co alloys with Pt/C (Adapted from Koh et al., 2007) 13
Figure 2.14: Schematic of degradation of catalyst particle (Wang et al., 2011) 14
Figure 2.15: Mechanism for the degradation of support and loss of ECSA. Taken from Shao et al. (2007). 15
Figure 2.16: (a) SEM image of NSTF catalyst (b) SEM cross section of NSTF catalyst electrode when transferred on to PEM. The membrane is coated with catalyst. (Debe et al., 2006) 17
Figure 2.17: (a) Fuel cell performance of 0.4 mg/cm^2 of Pt/C electrodes (b) Fuel cell performance of 0.15 mg/cm^2 NSTF electrodes (Sihna et al., 2011) 18
Figure 2.18: The influence of the catalyst loading on the activity of Pt/C catalysts (a) mass activity (b) surface specific activity (Fabbri et al., 2014) 19
Figure 2.19: Relationship between the mass activity and particle size (Wang et al., 2010) 19
Figure 2.20: Amount of hydrogen peroxide formed with an increase in metal loading (Adapted from Fabbri et al., 2014) 20
Figure 2.21: Cyclic voltammogram of a Pt electrode in 0.5 M H_2SO_4 solution at a scanning rate of 50 mV/s (Adapted from Ren et al., 2004) 21
Figure 2.22: The decrease in CV ECSA with an increase in particle size (Wang et al., 2012(2)) 22
Figure 2.23: Rotating ring disk electrochemistry (Collman & Decreau, 2008) 24
Figure 4.1: Illustration of the (a) stainless steel tube (b) graphite boat in which the thermally induced chemical decomposition occurred. 28

Figure 4.2: Three-compartment electrochemical cell (Gamry Instruments) with (a) Luggin capillary (b) Pt coil (c) glassy carbon working disk electrode (Pine instruments) (Adapted from Taylor et al. (2013)..... 29
Figure 5.1: Three cyclic voltammetry experiments measured separately for a commercial 40 wt. % Pt/C catalyst. Cyclic voltammetry was carried out in an Ar saturated 0.1 M $HClO_4$ solution at room temperature at a sweep rate of 50 mV/s..... 36
Figure 5.2: Linear sweep voltammetry of a commercial catalyst (a) test 1 (b) test 2 (c) test 3. The oxygen reduction current densities for the cathodic sweeps (5 mV/s, 1600 rpm) of the catalysts were recorded in an oxygen saturated 0.1 M $HClO_4$ solution at room temperature..... 37
Figure 5.3: Thermogravimetric analysis of platinum acetylacetonate..... 38
Figure 5.4: Thermogravimetric analysis of Cobalt (II) chloride hexahydrate..... 39
Figure 5.5: Thermogravimetric analysis of (a) Cobalt acetate (b) Cobalt acetylacetonate..... 39
Figure 5.6: Results from ink drying experiment. (a) Ink dried on a lab bench with a beaker over the electrode. (b) Ink dried in a fume hood with hood pulled down to allow for air flow. (c) Ink dried in an oven at 60 °C with a beaker over the electrode. (d) Ink dried on a rotating shaft at 700 rpm. 40
Figure 5.7: XRD graphs for Pt/C catalysts (a) 20 wt. % (b) 40 wt. % (c) 60. wt. % (d) 80 wt. %..... 41
Figure 5.8: Tem images of Pt/C (a) 20 wt. % (b) 40 wt. % (c) 60 wt. % (d) 80 wt. %..... 43
Figure 5.9: Histograms showing the particle size distribution of 100 Pt particles from Pt/C catalysts of loadings (a) 20 wt. % (b) 40 wt. % (c) 60 wt. % (d) 80 wt. %..... 44
Figure 5.10: TEM image of a 60 wt. % Pt/C catalyst prepared used the reactor pictured in the image (Taylor et al., 2013)..... 45
Figure 5.11: Cyclic voltammograms of Pt/C catalysts measured in an Ar saturated 0.1 M $HClO_4$ solution at a sweep rate of 50 mV/s using a 5.61 mm (OD) glassy carbon working electrode (Pine instruments, E7R9 Series)..... 46
Figure 5.12: CO stripping data collected in an O_2 saturated 0.1 M $HClO_4$ solution at a sweep rate of 50 mV/s using a 5.61 mm (OD) glassy carbon working electrode (Pine instruments, E7R9 Series)..... 47
Figure 5.13: Cathodic sweep data at 1600 rpm data measured in an O_2 saturated 0.1 M $HClO_4$ solution at a sweep rate of 20 mV/s using a 5.61 mm (OD) glassy carbon working electrode (Pine instruments, E7R9 Series). (a) Rotating disk electrode curves. (b) Tafel plot showing mass transport corrected current densities (i_k) calculated using data from curves in (a). (c) Surface specific activity data corrected for Pt/C catalyst (a) Mass activity data corrected for Pt/C catalysts..... 49
Figure 5.14: Rotating ring disk curves showing the hydrogen peroxide formation and the current collected by the ring. Results were obtained measured in an O_2 saturated 0.1 M $HClO_4$ solution at a sweep rate of 20 mV/s using a 5.61 mm working electrode (Pine instruments, E7R9 Series)..... 51
Figure 5.15: TEM image of a sample 40 wt. % Pt_3Co catalyst..... 53
Figure 5.16: TEM images of samples after annealing in reducing atmosphere (a) 500 °C for 4 hours (b) 800 °C for 7 hours (c) 900 °C for 2 hours..... 54
Figure 5.17: Particle size distribution of a 100 particles measured from TEM images for (a) 500 °C for 4 hours (b) 800 °C for 7 hours (c) 900 °C for 2 hours..... 55
Figure 5.18:Comparison of XRD curves before and after annealing at (a) 500 °C for 4 hours (b) 800 °C for 7 hours (c) 900 °C for 2 hours..... 56
Figure 5.19: Comparison of the change in lattice constants before and after annealing at different XRD peaks..... 57
Figure 5.20: XRD curves for carbon supported Pt_3Co catalysts measured before and after treatment (annealing and leaching) (a) 20 wt. % (b) 40 wt. % (c) 60 wt. % (d) 80 wt. % Pt_3Co catalysts..... 58

Figure 5.21: TEM images of heat treated and leached catalysts (a) 20 wt. % (b) 40 wt. % (c) 60 wt. % (d) 80 wt. % Pt_3Co catalysts..... 60
Figure 5.22: TEM particle size distribution for a 100 particles that have been heat treated and leached (a) 20 wt. % (b) 40 wt. % (c) 60 wt. % (d) 80 wt. % Pt_3Co/C catalysts 61
Figure 5.23: Cyclic voltammograms of Pt_3Co/C catalysts measured in an Ar saturated 0.1 M $HClO_4$ solution at a sweep rate of 50 mV/s using a 5.61 mm (OD) glassy carbon working electrode (Pine instruments, E7R9 Series)..... 62
Figure 5.24: CO stripping data collected in an O_2 saturated 0.1 M $HClO_4$ solution at a sweep rate of 50 mV/s using a 5.61 mm (OD) glassy carbon working electrode (Pine instruments, E7R9 Series) ... 63
Figure 5.25: Cathodic sweep data at 1600 rpm data measured in an O_2 saturated 0.1 M $HClO_4$ solution at a sweep rate of 20 mV/s using a 5.61 mm (OD) glassy carbon working electrode (Pine instruments, E7R9 Series). (a)Rotating disk electrode curves. (b) Tafel plot showing mass transport corrected current densities (i_k) calculated using data from curves in (a). (c) Surface specific activity data corrected for Pt_3Co alloy (a) Mass activity data corrected for Pt_3Co alloy..... 64
Figure 5.26: Rotating ring disk curves showing the hydrogen peroxide formation and the current collected by the ring. Results were obtained measured in an O_2 saturated 0.1 M $HClO_4$ solution at a sweep rate of 20 mV/s using a 5.61 mm working electrode (Pine instruments, E7R9 Series)..... 66
Figure 8.1: TEM images of Pt_3Co/C catalysts with no treatment (a) 20 wt. % (b) 40 wt. % (c) 60 wt. % (d) 80 wt. % 78
Figure 8.2: Particle size distribution of Pt_3Co/C catalyst before treatment 79

List of Tables

Table 4.1: List of chemicals and gases used 26
Table 4.2: Precursor and carbon measurements 27
Table 4.3: Summary of theoretical diffusion limiting currents for 5.61 mm (OD) working electrode (Pine Instruments, E7R9 series) and 5 mm (OD) working electrode (Pine Instruments, E3 series) 32
Table 5.1: Experimental ECSA of a commercial catalyst 36
Table 5.2: Experimentally measured diffusion limiting current values of a 40 wt. % commercial catalyst compared to the theoretical values 38
Table 5.3: D-spacings for the Pt/C catalysts 42
Table 5.4: Average crystallite size (nm) of Pt/C catalysts. Particle sizes calculated using the Scherrer equation. 42
Table 5.5: Summary of TEM data 44
Table 5.6: TGA data collected for Pt/C catalysts. 46
Table 5.7: Experimental ECSA values for Pt/C catalysts 47
Table 5.8: CO stripping ECSA values 48
Table 5.9: Comparison of diffusion limiting current values of commercial catalysts and 5 mm (OD) Pt disks 50
Table 5.10: Comparison of mass and surface specific activities of Pt/C catalysts at 0.9 vs. RHE (V) 50
Table 5.11: Summary of Cl removal methods 52
Table 5.12: XRD average crystallite size (nm). Particle sizes calculated using the Scherrer equation. 56
Table 5.13: Average crystallite size (nm) of the Pt_3Co/C catalyst. Particle sizes calculated using the Scherrer equation. 58
Table 5.14: Lattice constants for Pt_3Co/C catalysts 59
Table 5.15: SEM-EDX values of Pt_3Co after heat treatment and leaching 61
Table 5.16: TGA readings after each stage of treatment 62
Table 5.17: Experimental ECSA values for Pt_3Co/C catalysts 63
Table 5.18: CO stripping ECSA values 64
Table 5.19: Mass and Surface specific activity for cathodic sweep data of Pt_3Co/C catalysts at 0.9 vs. RHE (V) and 1600 rpm 65
Table 5.20: Comparison of mass and surface specific activity between Pt/C and Pt_3Co/C 67

1. Introduction

In recent years the search for alternative forms of clean energy has increased. Polymer electrolyte fuel cells (PEFC) have generated much interest as an alternative to traditional conventional internal combustion engines, secondary batteries and other power sources (Zhang et al., 2013). The benefits of fuel cells over other energy equipment are: they are quiet, have no moving parts and have zero emissions. However, there are several drawbacks associated with this technology. The oxygen reduction reaction (ORR) which occurs on the cathode of PEFC requires high catalyst loadings because of its slow kinetics. The catalyst metal often used is platinum (Pt). It is well-known that Pt is expensive because it is a limited natural resource and its price will probably increase as time goes on. The cost of the catalyst is therefore one the factors hindering wide scale commercialisation of fuel cells. For example, in order for fuel cells to be implemented commercially for automobiles a five-fold enhancement of the catalytic activity is required (Wang et al., 2011). In order to reduce the cost it is essential to either decrease the amount of Pt used by increasing the mass specific activity or an alternative non-noble metal catalyst activity with an acceptable performance will need to be found (Zhang et al., 2013). A significant amount of research has been done on how the catalytic activity can be improved. It has been found that alloying is one way in which that goal can be achieved (Stamenkovic et al., 2006). Bimetallic alloys have shown enhancement factors of up to 3 over Pt/C (Wang et al., 2011).

Another problem encountered with Pt/C catalysts is their low durability. When in operation the catalysts agglomerate or detach from the carbon support (Zhang et al., 2013). The support is also susceptible to oxidation which would degrade the performance of the fuel cell and reduce its lifetime (Zhang et al., 2013). In their study Wang et al. (2011) demonstrated that using bimetallic alloys can improve the durability of the catalyst.

The aim of the research presented was to gain a better understanding of the influence of Pt alloy particle size and active surface morphology on the ORR activity. The alloy considered was Pt_3Co/C.

The investigation was limited to the comparison of the performance of Pt/C and Pt_3Co/C at increasing metal loadings. Analyses of the catalysts was limited to the following electrochemical characterisation techniques: cyclic voltammetry, CO stripping voltammetry, rotating disk electrode and rotating ring disk electrode. The following physical characterisation techniques were used: thermogravimetric analysis, x-ray diffraction, transmission electron microscopy and energy dispersive x-ray spectroscopy.

2. Literature review

2.1. Polymer electrolyte membrane fuel cells

A fuel cell is a device that converts chemical energy into electrical energy. Figure 2.1(a) shows a typical hydrogen fuelled PEFC. Hydrogen is fed to the anode, where is it oxidized to form protons (H^+) and electrons. The electrons released generate an electrical current whilst the H^+ ions pass through the non-electrically conducting membrane. At the cathode side of the fuel cell, oxygen is reduced by the electrons and then combines with the H^+ ions from the membrane to form water. A schematic of these reactions and pathways is shown in Figure 2.1(a). Figure 2.1(b) shows an enlarged section of the cathode side of a fuel cell, which consists of the interaction between the proton exchange membrane (PEM), the catalyst layer and the gas diffusion layer (GDL). In the electrode, the importance of transport processes is emphasized. A successful and effective electrode is one that can balance all the transport processes of the three phases found in the catalyst layer (Litster and McLean, 2004). The three phases are the protons, the electrons and the gases.

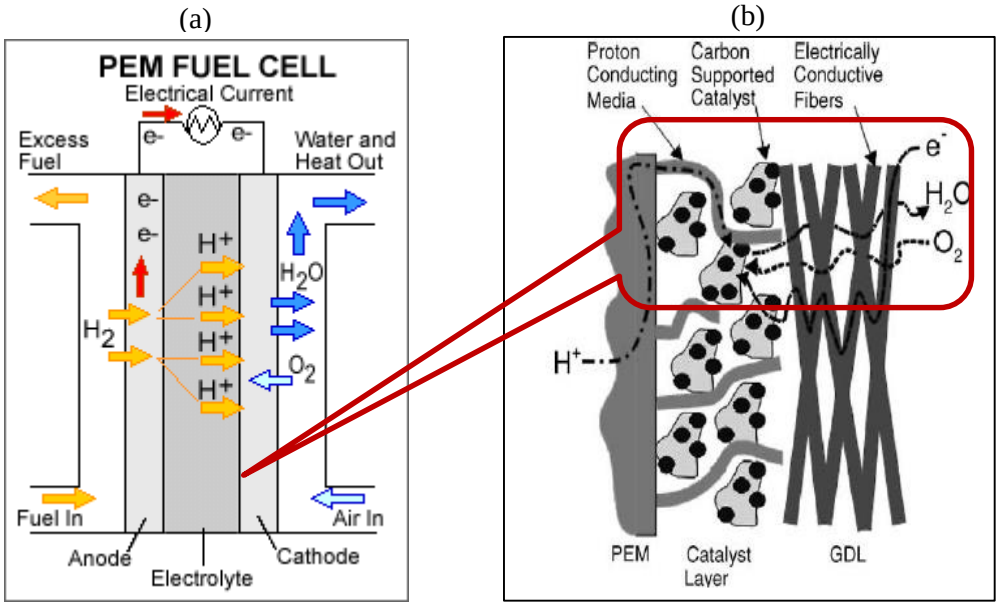

Figure 2.1: (a) Single PEM fuel cell (Adapted from Wang et al., 2011). (b) Three phase boundary in an electrode (Adapted from Litster & McLean, 2004).

Figure 2.1(b) also displays the catalyst layer in detail. The catalyst particles are depicted as the dark spheres and are usually either Pt or Pt alloys. This is the site of the cathode and anode half-cell reactions shown below. Equation (2.1) represents the oxidation reaction at the anode. Equation (2.2) is known as the oxygen reduction reaction (ORR) at the cathode.

$$H_2 \rightarrow 2H^+ + 2e^- \tag{2.1}$$

$$\frac{1}{2}O_2 + 2H^+ + 2e^- \rightarrow H_2O \tag{2.2}$$

The kinetics of equation (2.2) are much slower than that of equation (2.1) (Nørskov et al., 2004). This is exacerbated by the multi-electron process nature of the reaction which contains a number of reaction intermediates and elementary steps (Rabis et al., 2012). As a result, the overpotential associated with the ORR is relatively large (0.3 – 0.4 V) and high catalyst loadings are often needed to overcome this (Rabis et al., 2012).

2.2. Oxygen reduction reaction catalysts

2.2.1. Oxygen reduction reaction mechanism

There is still no consensus over the exact mechanism for the oxygen reduction reaction. Some of this is owing to a lack of appropriate experimental techniques, which are able to accurately determine the composition and coverage of surface intermediates that form during the ORR (Markiewicz et al., 2015). As this study is limited to the study of ORR in acidic electrolyte the discussion on the mechanism and catalysts will be limited to that.

It has been suggested that there are mainly two possible mechanisms through which the oxygen reduction reaction occurs. These are a direct 4-electron reduction pathway and a sequential pathway with two 2-electron steps (Zhang et al., 2008). Nørskov et al. (2004) described mechanisms for the two pathways, the dissociative and the associative mechanism. These two pathways are depicted in Figure 2.2.

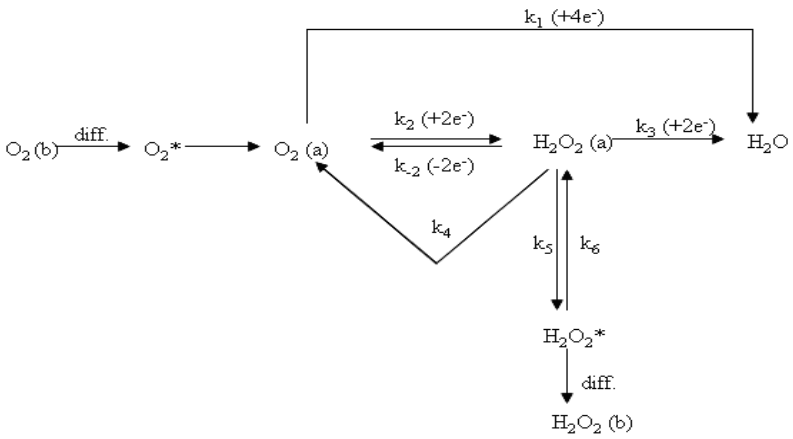

Figure 2.2: Scheme of oxygen reduction mechanism (Yue et al., 2010).

2.2.1.1. Dissociative mechanism

In the dissociative mechanism O_2 dissociates and adsorbs on an active site on the catalyst surface where it is hydrogenated to form an OH* intermediate. The intermediate then further reacts with a proton and an electron to form water and regenerate the catalyst active site. Reaction (2.3), (2.4) and (2.5) demonstrate this mechanism (Nørskov et al., 2004). This mechanism is suggested for the 4-electron pathway.

$$\frac{1}{2}O_2 + * \rightarrow O^* \quad (2.3)$$

$$O^* + H^+ + e^- \rightarrow OH^* \quad (2.4)$$

$$OH^* + H^+ + e^- \rightarrow H_2O + * \quad (2.5)$$

2.2.1.2. Associative mechanism

In the associative mechanism O_2 does not dissociate before it is hydrogenated. This process is shown in reactions (2.6) to (2.10) (Nørskov et al., 2004). This mechanism is suggested for the 2-electron pathway.

$$O_2 + * \rightarrow {O_2}^* \quad (2.6)$$

$${O_2}^* + (H^+ + e^-) \rightarrow {HO_2}^* \quad (2.7)$$

$${HO_2}^* + (H^+ + e^-) \rightarrow H_2O + O^* \quad (2.8)$$

$$O^* + (H^+ + e^-) \rightarrow HO^* \quad (2.9)$$

$$HO^* + (H^+ + e^-) \rightarrow H_2O + * \quad (2.10)$$

Equations (2.9) and (2.10) are also found in the dissociative mechanism. The steps (2.6) to (2.8) are known as the associative mechanism. An alternative to forming water in equation (2.8) is to form H_2O_2 (Nørskov et al., 2004). Hence this mechanism is also termed a peroxo mechanism.

Although there is a debate about which mechanism is followed exactly and what the reaction steps are, there is some strong experimental evidence that the ORR proceeds via peroxide formation (Rabis et al., 2012). Ideally a 4-electron pathway forming only water regardless of electrolyte would be preferred. Hydrogen peroxide diffuses into the PEM and results in radical oxidative degradation in the membrane (Holton & Stevenson, 2013). Recent work between researchers of HySA/Catalysis and collaborators at the Paul Scherer Institute (PSI) has indicated that the dissociative pathway is the observed mechanism in the ORR particularly at higher Pt loadings, i.e. reduced Pt-Pt interatomic distances (Fabbri et al., 2014).

2.2.2. Current state of catalysts

2.2.2.1. Catalyst metal

The complexity of the ORR has caused many challenges for the selection of the catalyst material. The material needs to be stable under extremely corrosive conditions and be chemically active enough to activate oxygen (Holton & Stevenson, 2013). It is well known that noble metals are inert and resistant to corrosion and oxidation in the presence of moisture. These properties make them attractive for the use as catalyst material in the ORR.

The most commonly used catalyst is Pt. It has been proven that Pt is one of the best catalysts for ORR. In their study, Nørskov et al. (2004) were able to predict and compare the activities of different metals in the ORR. They were able to construct a volcano-plot from the activities and the oxygen binding energies they calculated using density functional theory (DFT). This is illustrated in Figure 2.3. From Figure 2.3 it can be seen that Pt is the best metal for the ORR, however there is room for improvement towards the peak of the volcano plot.

Alloying of the Pt metal is one way in which the improvement can be achieved. Additionally alloying can reduce the cost of the catalyst metal.

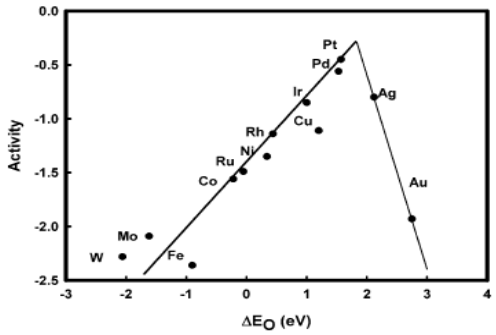

Figure 2.3: Variation of the oxygen reduction activities for different metals compared to the oxygen binding energies (Nørskov et al., 2004).

One possible explanation for the difference in activity of different metals was proposed by Nørskov et al. (2004) and pertains to the bonding of the oxygen to metals. Metals that form either weaker or stronger bonds with oxygen than Pt have several drawbacks. If the metal binds too strongly, e.g. nickel, then the proton transfer steps become strongly activated and therefore very slow. Conversely if the metal binds too weakly, e.g. gold, then the proton transfer is exothermic and should be fast. Unfortunately the oxygen will be more stable in the gas phase than it is on the surface. As a result the transfer of protons and electrons cannot occur.

Therefore Pt has been found to be one of the most efficient metals for the ORR regardless of which mechanism (dissociative or associative) proceeds. However, Pt is a precious metal with high costs associated with it. As a result, in order for fuel cell technology to become reasonably competitive on a commercial scale in automotive applications, the US Department of Energy (DoE) set an MEA catalyst loading target for 2020 (U.S. Department of Energy, 2013): Pt group metal total loading - 0.125 $mg_{pgm}/cm^2_{electrode\ area}$.

The current Pt group metal loading that has been achieved is 0.15 $mg_{pgm}/cm^2_{electrode\ area}$ (U.S. Department of Energy, 2013).

2.2.2.2. Support material

Catalyst supports have several important functions. A good support must have the following properties (Wang Y. et al., 2011):

- Very good electronic conductivity
- High corrosion resistance
- High surface area
- Strong cohesive force to catalyst metal
- Easy formation of uniform dispersion of catalyst particles on their surface

Some of the most common supports utilized currently are high surface area carbon blacks like Vulcan XC-72R and Ketjenblack (Dicks, 2006). Carbon supports have several durability problems that affect their performance in automobile applications. These durability problems will be discussed in greater detail later in this work.

A great deal of research has recently gone into the possibility of replacing carbon with inorganic supports. Some of these include carbides, nitrides, and borides, electronically conducting polymers and conducting metal oxides (Wang Y et al., 2011). However carbon is still the leading support material used. This is because of its excellent physical properties, its abundance in nature making it affordable and its processibility and relative stability in both acidic and basic solutions (Huang & Wang, 2014).

2.3. Alloys

2.3.1. Overview

Many researchers have explored the prospects of alloying Pt with other metals. The common metals tested for alloying are the 3d transition metals. Some of the metals explored for alloying are nickel (Ni), cobalt (Co), iron (Fe), titanium (Ti), vanadium (V), ruthenium (Rh) and chromium (Cr) (Stamenkovic et al., 2006). Binary and ternary alloying has been extensively researched. Alloying has been found to improve the activity of a Pt catalyst. Figure 2.4 compares the specific activities of different bimetallic alloys compared to Pt. From Figure 2.4, Pt-Co, Pt-Ni and Pt-Fe show large improvements in catalytic activity. The Pt-Ti and Pt-V showed an improvement on the Pt catalyst but not as much as the other Pt alloys. Dealloyed ternary alloys e.g. $PtNi_3M$ (where M is Co and Cu) have also been shown to

significantly enhance the activity and in some cases 1.7 × more than binary alloys like $PtNi_3$ (Mani et a., 2010) .

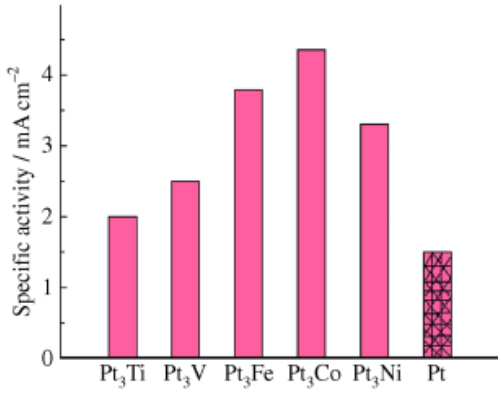

Figure 2.4: The specific activity of Pt alloys for ORR expressed as kinetic densities (Stamenkovic et al., 2006)

Figure 2.5 is a model of activity proposed by Stamenkovic et al. (2006). It illustrates how the volcano plot suggested by Nørskov et al. (2004) can be improved by alloying. The model developed by Stamenkovic et al. (2006) estimates which bond energies of Pt alloys would give the peak of the "volcano". It is able to predict the trend in catalytic activity. The model was able to estimate which Pt alloys can give the highest activity. The results produced are good enough for an initial estimate of catalytic activity.

Figure 2.5: Model of activity as a function of the adsorption energy of oxygen. The plot in red is the actual measured activity relative to that of Pt (Stamenkovic et al., 2006).

Various explanations have been offered in literature for the enhanced activity of alloys. The most prominent factors identified in literature are the Pt-Pt interatomic distance, the surface area, the increased Pt d-band vacancy and the distribution of the surface (Salgado et al., 2004). Alloying causes a lattice contraction, leading to a more favourable Pt-Pt distance for the dissociative mechanism (Zhang et al., 2008). The d-band vacancy can be increased after alloying, producing a strong metal – O_2

interaction then weakening the O-O bonds (Zhang et al., 2008). Paulus et al. (2002) and Wang et al. (2013) saw a shift in the onset potential (approximately 50 mV higher than Pt) of Pt-OH_{ad} with alloy catalysts and attributed it to intermetallic bonding between Pt and the alloying metal.

Of the literature covered for this report, there is no consensus on which alloy is the best. However, generally literature cites the Pt-Co alloy systems as being one of the most active and stable catalysts in acidic environments (Wang et al., 2013). Enhancement factors of as much as five have been reported when alloying Pt-Co (Paulus et al., 2002). As mentioned above, the scope of this study has therefore been limited to Pt-Co alloys.

2.3.2. Pt–Co alloys as ORR catalyst

As reported previously Pt-Co alloys have been known to improve the ORR activity. Comparing Pt-Co alloys across literature is made difficult because of the myriad of factors affecting the activity. These factors include the method of preparation, the degree of alloying, the particle size, shape, orientation and of course composition with the method of preparation affecting the degree of alloying (Salgado et al., 2004).

The origin of enhanced activity has been explored in-depth in literature. As stated previously one of the factors responsible for the enhanced activity is the shortening of the Pt-Pt bond length (Zhang et al., 2008). The decrease in bond length after alloying was observed by Chen et al. (2009) and is demonstrated in Figure 2.6 below.

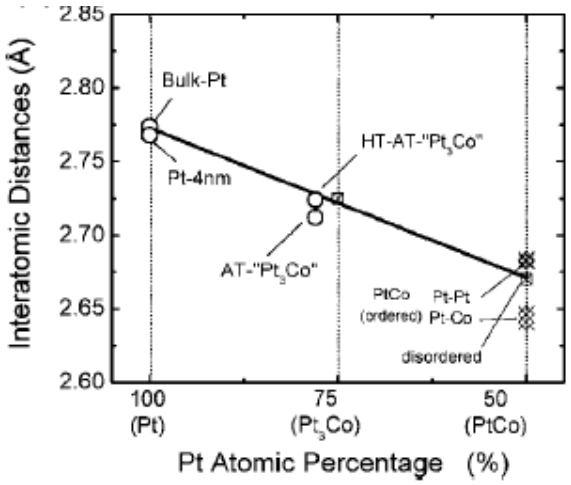

Figure 2.6: Interatomic distances calculated for Pt, Pt_3Co and PtCo (Chen et al., 2009)

Additionally the interatomic distance was shown to decrease with an increase in Co atomic concentration (Chen et al., 2009). Figure 2.7 shows a correlation between the d-band centre and the oxygen adsorption energy (ΔE_0).

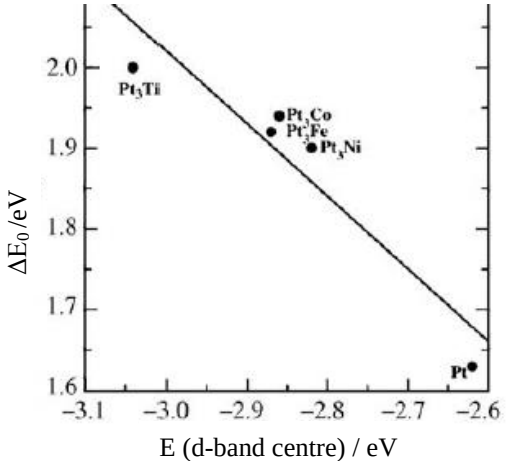

Figure 2.7: Correlation between the d-band centre and the oxygen adsorption energy (Adapted from Stamenkovic et al., 2006)

Stamenkovic et al. (2006) provided a relationship between the d-vacancy centre and ΔE_0 as shown in Figure 2.7. ΔE_0 is known as a good indicator for activity as explained in Section 2.3.1. However, ΔE_0 is determined by the average energy of the d-states on the surface atoms to which the adsorbate binds i.e. the d-band centre. The Figure 2.8 below shows the relationship between the specific activity and the Pt-Pt interatomic bond length obtained by EXAFS. It is clear that the ORR activity increases with a decrease in the bond length.

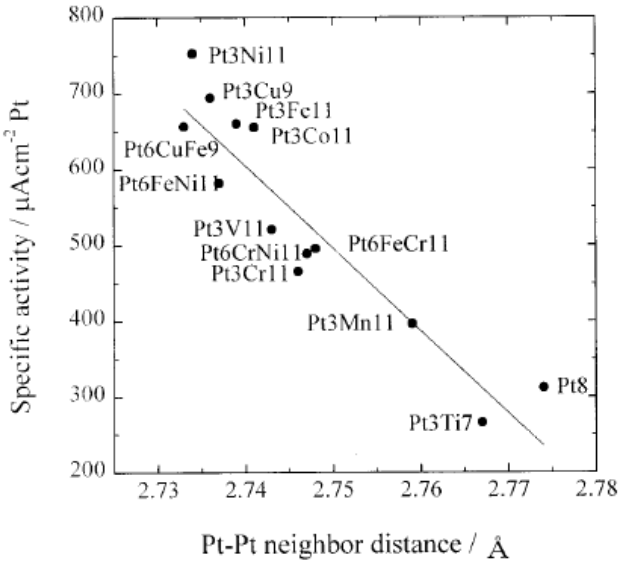

Figure 2.8: Effect of the Pt-Pt neighbour distance on the specific activity (Min et al., 2000)

Paulus et al. (2002) tested carbon supported bimetallic Pt-Co catalysts with 50 and 75 at. % Pt against Pt/C. In their work PtCo (i.e. 50 at. % Pt) produced a greater enhancement of mass activity relative to Pt_3Co. Salgado et al. (2004) reported that increasing the Co content causes a decrease in metal particle size and an improvement in activity for the ORR. The influence of the Pt:Co on the mean particle distance is shown in Figure 2.9 (a). Figure 2.9 (b) shows the effect of the mean interatomic distance and Pt:Co ratio on the performance of the catalyst. From Figure 2.9 it is clear that increasing the Pt:Co is favourable for the ORR. Smaller particles yield a larger ECSA and an improved activity of the catalyst (Paulus et al., 2002). The improvement in activity for PtCo over Pt_3Co is also because the alloy metals are oxidised on the surface with one or more OH ligands attached. This could influence the OH_{ad} formation on nearby Pt atoms hindering the formation of oxides on them (Paulus et al., 2002). However, the stability of the Pt_3Co alloy is greater than that of PtCo (Antolini et al., 2006).

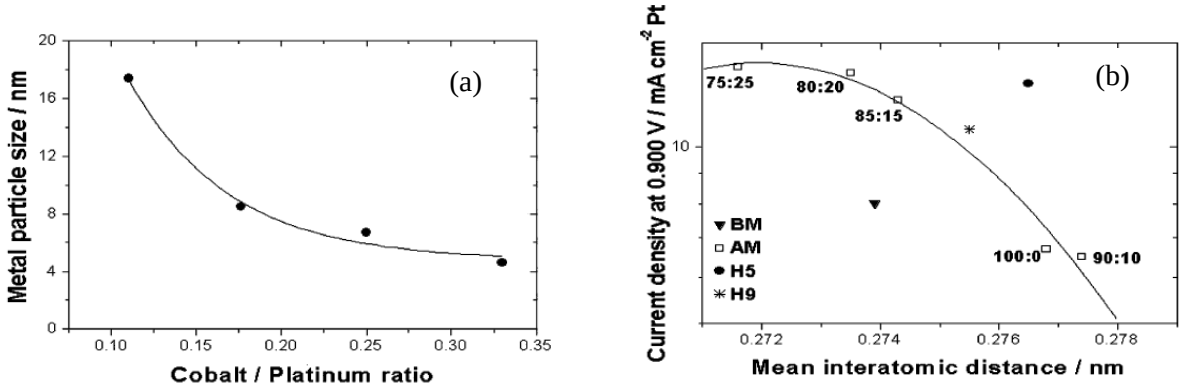

Figure 2.9: (a) Influence of the Co/Pt ratio on the mean particle size. (b) Correlation of oxygen electrode performance of Pt and Pt-Co catalysts with the mean interatomic distance (Adapted from Salgado et al., 2004)

In some literature it has been demonstrated that the larger the second metal content, i.e. Co, past an optimal point causes an increase in the 5d vacancy therefore the Pt-O bond becomes stronger and the back-donation turns out to be difficult (Rabis et al., 2012). The overall result of this is a lowering in the ORR rate.

2.3.3. Leaching of cobalt

Transition metals such as Ni, Co and Fe have been found to leach out of the catalyst alloy during operation (Holton & Stevenson, 2013). There are several causes of leaching of the base metals (Holton & Stevenson, 2013):

- The deposition of excess base metal in the alloy
- The use of too low alloying temperatures which result in incomplete alloying
- The base metal may be thermodynamically unstable in the alloy

The leaching out of the base metal may contaminate the MEA. The leached out cations (e.g. Co^{2+}) cause a degradation of the catalyst conductivity, higher ohmic losses and lowering of the activity (Gasteiger et al., 2005).

It has been shown that the amount of base metal that leaches out during operation can be minimized by pre-leaching the alloy (Gasteiger et al., 2005). This effect is illustrated in Figure 2.10. The multiple pre-leached alloy catalyst showed the least amount of leaching under operation (less than 4%).

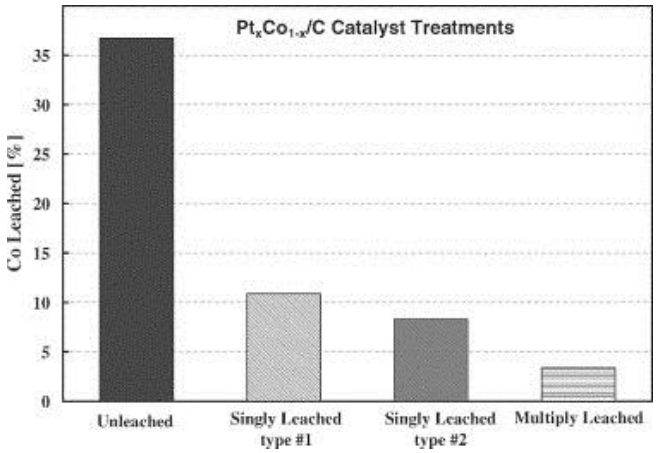

Figure 2.10: The effect of pre-leaching Pt-Co catalysts on the dissolution of Co (Gasteiger et al., 2005)

Pre-leaching produces a Pt-skin structure as shown in Figure 2.11 with a stable intermetallic Pt and Co arrangement in the centre. Particles with a Pt-skin display some of the highest mass activities and displayed enhanced durability even after 5000 cycles (Wang et al., 2013).

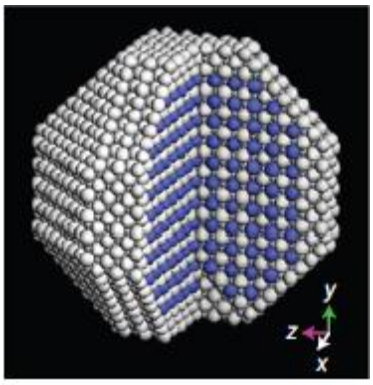

Figure 2.11: Pt_3Co atomic nanoparticles. The white and blue spheres represent Pt ad Co atoms respectively (Wang et al., 2013)

2.3.4. Heat treatment of alloy

Thermal treatments of the alloys have been known to improve the catalyst activity. In order to create a Pt skin on the topmost layer of the catalyst by inducing Pt segregation, thermal treatment under ultra-high vacuum (UHV) has been used on bimetallic catalysts (Pt_3M) (Wang et al., 2011). Another common method is annealing in a reducing atmosphere, i.e. in a gas stream of H_2/Ar .The potential pitfalls of

such treatments at particularly higher temperatures (>600 °C) are sintering and therefore loss of the electrochemical surface area (ECSA). Koh et al. (2007) annealed Pt_3Co at 600 °C and at 950 ° C. They found that higher temperature annealing (950 °C) produced particles (5 nm) in a single ordered phase. Lower temperature annealing produced multiple phases which are generally undesired. Other studies however reported only a single phase after annealing with various temperatures (Wang et al., 2010).

In general, the particle size increases with annealing owing to the agglomeration of particles, i.e. sintering (Wang et al., 2010). Figure 2.12 illustrates the effect of using lower temperatures for annealing. Annealing at 600 °C produced enhanced activity compared to annealing at 950 °C.

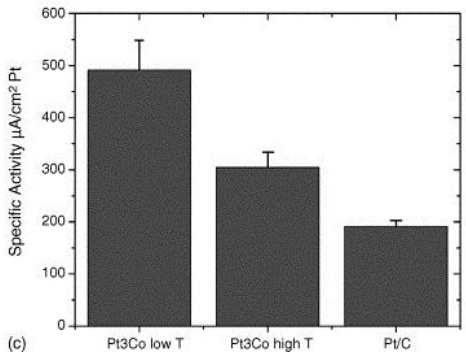

Figure 2.12: Specific activity of low T (600 °C) and high T (950 °C) Pt_3Co at 900 mV/RHE compared to Pt/C (Koh et al., 2007)

Wang et al. (2011) investigated the post treatment of their PtNi/C alloy by annealing at 400 °C. They observed improved activity and durability of the alloy as a result. They also reported that annealing reconstructed the surface of the catalyst reducing the low coordination sites.

Koh et al. (2007) offered an explanation as to why the activity of low temperature annealing is better than high temperature annealing. Comparing the voltammograms in Figure 2.13 one can see that there is a delay in Pt-OH formation for the high temperature catalyst. This delay has been linked with ORR activity. More importantly the capacitive current of the low temperature catalyst is higher. This correlates to a higher surface area (Tabet-Aoul & Mohamedi, 2012).

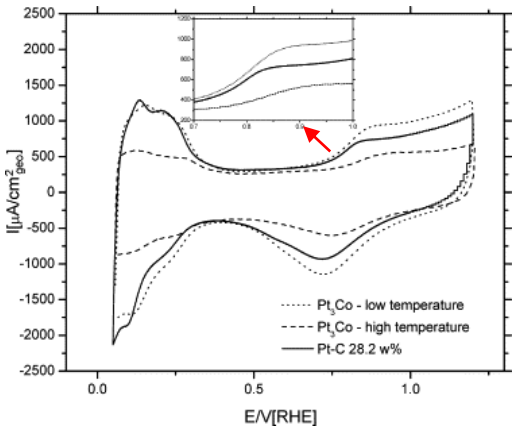

Figure 2.13: Cyclic voltammetry plots comparing Pt-Co alloys with Pt/C (Adapted from Koh et al., 2007)

Increasing the annealing temperature also decreases the H_{upd} region which corresponds to a reduction in the electrochemical surface area (Wang et al., 2010). Some literature cites moderate temperatures (400-500 °C) as preferable because this would still ensure the benefits of annealing are experienced without the pronounced effect of sintering. These benefits are (Wang et al., 2010):

- Reduced surface defects
- Reduced low coordination surface sites
- Reduced oxophilicity
- Enhanced stability

However, Wang et al. (2013) compared Pt_3Co annealed at 400 °C and 700 °C. The alloy at 700 °C still had a particle size of only 5 nm measured using scanning transmission electron microscope (STEM). Higher temperature annealing can provide much higher mass activity and greater durability under potential cycling (Wang et al., 2013).

2.4. Catalyst Durability

2.4.1. Corrosion mechanism and consequences

For a catalyst to be successful for the ORR it must not only be active but it also needs to be stable in the harsh environment of a fuel cell. The enhanced activity of a Pt/C or Pt_3Co/C catalyst is meaningless if it is not stable under fuel cell operating conditions.

The typical issues in relation to catalyst durability for Pt and Pt-Co alloys are Pt dissolution, Oswald ripening, leaching out of Co, and carbon corrosion of the support. It has been reported that the processes of Oswald ripening, Pt migration and sintering occur at a higher rate for Pt/C compared to the re-

deposition and particle sintering of Pt alloys (Colon-Mercado & Popov, 2006). Figure 2.14 shows one example of the mechanisms of the degradation of the catalyst, i.e. the dissolution of the Pt and its precipitation.

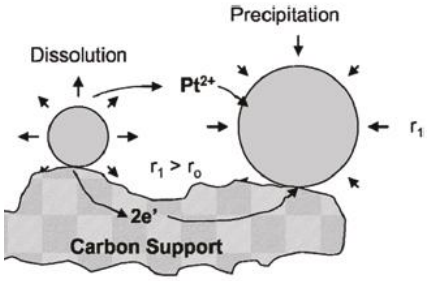

Figure 2.14: Schematic of degradation of catalyst particle (Wang et al., 2011)

As mentioned previously the leaching out of Co is a durability concern. Generally, when tested in a fuel cell stack after 1000 h the Co leaches out onto the surface leaving a "Pt-skeleton" structure (Maillard et al., 2010).

A Pt-skeleton schematic was shown in Figure 2.11. This structure has a Pt-Co core and a Pt shell. On the surface the leached Co forms Co-O, i.e. surface oxides. The leached out Co cations can poison ion exchange sites (Zhang et al., 2008). In a fuel cell proton exchange takes place in the membrane and ionomer within the catalyst layer. The number of ion-exchange sites is however limited. Metal cations (i.e. Co^{2+}) occupy and poison these ion-exchange sites because the cations have a higher affinity for sulfonic groups than protons (Zhang et al., 2008). The consequences of poisoning the ion-exchange site are (Zhang et al., 2008):

- A reduction of membrane conductivity due to dehydration leading to higher membrane resistance.
- An increase in the resistance of the catalyst layer due to ionomer resistance.
- A degradation of the membrane with some metal cations e.g. Fe due to Fenton's effect.
- The decrease in oxygen diffusion in the ionomer film.

This leads to the conclusion that the structure is not stable under real stack operating conditions after prolonged periods. Despite this, alloy catalysts have been reported to show high durability comparable to that of Pt/C (Gasteiger et al., 2005) and other studies found that the durability was enhanced through alloying (Wang et al., 2011).

The formation of the Pt-skin enhanced the activity and durability of the catalyst (Wang et al., 2013). In an alloy both the base metal and the Pt dissolve into the electrolyte (Colon-Mercado & Popov, 2006). Pt in the catalyst alloy has been reported to dissolve in the electrolyte and redeposit itself on the surface

of a larger particle in a phenomenon known as Oswald ripening (Colon-Mercado & Popov, 2006). However, despite the dual effect of the dissolution of the Pt and the base metal, the surface loss experienced by alloy has been found to be less than that of Pt/C. The movement of Pt on the surface was found to be hindered by the presence of an alloy metal therefore suppressing the sintering effect (Antolini et al., 2006).

2.4.2. Carbon corrosion

The carbon support can be corroded by oxidation. Carbon corrosion is induced by the transitioning between start-up and shut-down and fuel starvation (Wu et al., 2008). The most commonly cited reaction for the oxidation of carbon is a 4-electron pathway shown below (Ball et al., 2007):

$$C + 2H_2O \rightarrow CO_2 + 4H^+ + 4e^- \quad (11)$$

Carbon corrosion can cause particle sintering and loss of active area (Colon-Mercado & Popov, 2006). It makes the electrode more prone to flooding and accelerates the growth and redistribution of catalyst particles (Zhang et al., 2008). The oxidation of the support is what leads to the Pt/Pt alloys falling off the surface and the reduction of the ECSA (Shao et al., 2007). This is shown is Figure 2.15.

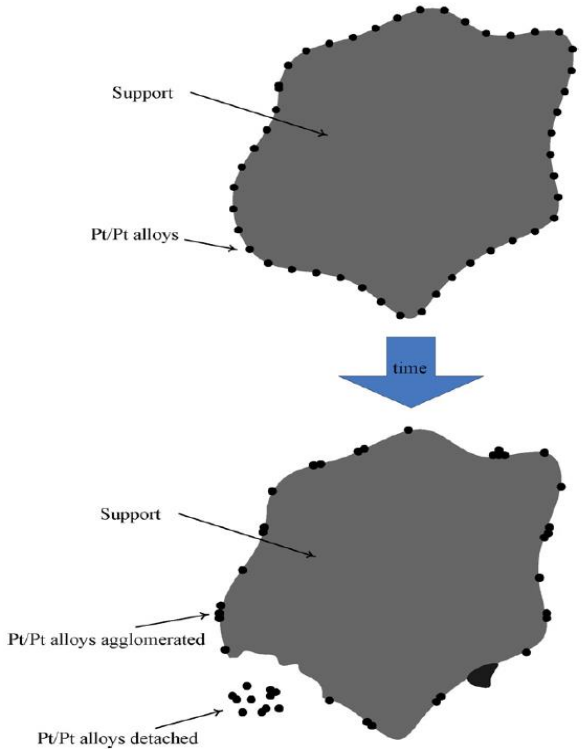

Figure 2.15: Mechanism for the degradation of support and loss of ECSA. Taken from Shao et al. (2007).

2.4.2.1. Start-up/shut down cycling

Carbon corrosion is not severe under normal operating conditions. The corrosion is accelerated under extreme operating conditions. Particularly at 1.2 V, carbon corrosion is thermodynamically favourable.

Start-up and shut down is an example of some of the harsh operating conditions which exacerbate corrosion. A fuel cell in an automotive mobile is expected to withstand approximately 30 000 start-ups and shut downs in its lifetime (Zhang et al., 2009). Therefore its durability under such conditions is pertinent to fuel cell development.

2.4.2.2. Load cycling (Potential)

Load cycling is used to investigate the performance changes during operation under various conditions (Zhang et al., 2009). The fuel cell will experience various load changes in its lifetime. The cell will cycle from high to low current and the potential will also vary as a consequence. If the fuel is relatively pure H_2, the anode potential will remain close to the reversible hydrogen potential due to the facile nature of the H_2 oxidation reaction (Borup et al., 2007). The cathode, however, will experience potential swings to match variable power demands (Borup et al., 2007). This variation of the cathode potential alters several properties of the electrode material in particular the degree of oxide coverage of both Pt and C and the hydrophobicity of the surfaces (Borup et al., 2007).

2.4.2.3. Role of catalyst metal on corrosion

The oxidation of carbon can further be catalysed by the presence of Pt. Since the degradation is accelerated by Pt, it has been suggested that the presence of an efficient Pt catalyst for the ORR is increasingly detrimental to the support (Shao et al., 2007). Therefore if Pt alloys are more active than Pt then they could possibly corrode the support at a higher rate. Additionally higher Pt loadings have been associated with greater carbon corrosion (Shao et al., 2007).

2.4.2.4. Alternative support materials

Owing to the corrosion issues with carbon, alternative non-carbon support materials have been investigated. These materials include mesoporous silicas, nitrides, carbides, metal oxides and conducting polymers, some of which have demonstrated superior performance in activity, stability and poison tolerance (Wang Y et al., 2011). However inorganic supports still have several drawbacks when compared to carbon some of which include the following (Wang Y et al., 2011):

- Lower electronic conductivity
- Higher solubility in aqueous and acidic environments
- Less thermal stability at high temperatures, e.g. conductive polymers at > 100 °C
- Lower surface area
- Less electrochemical and chemical stability

2.5. Catalyst surface structure and morphology

Traditionally the catalyst metal is placed on a support. Supports are used in catalysis for various reasons. They can minimize mass transfer limitations, reduce sintering and enhance the mechanical stability of the catalyst (Wang et al, 2011). They can also increase the surface area of the active metal. Pt or Pt alloy nanoparticles can be dispersed on a carbon support. The loading of the catalyst material can be varied to improve the catalyst performance. As mentioned previously the use of a carbon support can also reduce the durability of the catalyst through carbon corrosion. Dissolution of the catalyst metal can occur as well.

However, the catalyst metal can be also formed into an extended surface. In an extended surface the catalyst is formed into a three-dimensional thin structure (Gancs et al., 2008). 3M developed a nanostructured thin film (NSTF) catalyst devoid of a carbon support (Debe et al., 2006).

2.5.1. Extended surfaces

When dealing with nanoparticles, several issues arise. These particles have more edges and corners which have low coordination numbers. They exhibit preferential oxidation for OH^- which blocks oxygen from adsorbing onto the atoms (Wang et al., 2011). They are also more susceptible to migration and dissolution which both result in poor durability and fast decay (Wang et al., 2011).

As mentioned above 3M developed a nanostructured thin film (NSTF) catalyst. The catalyst is formed as a part of electrodes to form "nanowhiskers". Figure 2.16 shows scanned electron microscope (SEM) images of the NSTF catalyst and the catalyst loaded on the membrane. As seen in Figure 2.16(a) the NSTF consists of elongated particles that are formed by vacuum coating catalyst onto organic crystallite whiskers (Debe et al., 2006).

(a) (b)

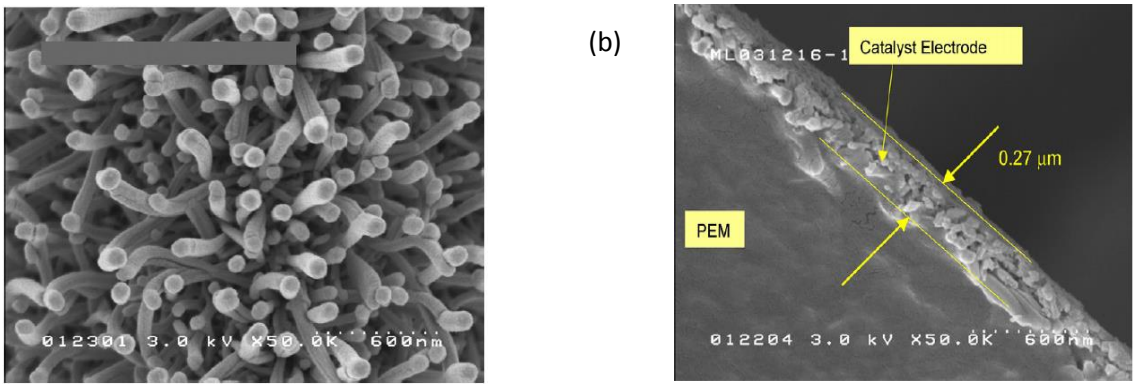

Figure 2.16: (a) SEM image of NSTF catalyst (b) SEM cross section of NSTF catalyst electrode when transferred on to PEM. The membrane is coated with catalyst. (Debe et al., 2006)

2.5.1.1. Advantages of nanostructured thin film catalysts

The advantages of these surfaces over Pt nanoparticles supported on carbon are varied. The NSTF catalysts demonstrate enhanced specific activity and greater resistance to Pt dissolution and hence reduced loss of ECSA at reduced Pt loadings (Sinha et al., 2011).

The performance loss due to cyclic voltammetry cycling is much less for NSTF catalysts than Pt/C nanoparticles. ECSA loss of NSTF catalysts stabilized to approximately 33% after 9000 cycles whilst the ECSA of Pt/C was reduced by 90% after 2000 cycles (Debe et al., 2006). This illustrates the better stability of the NSTF catalysts. These catalysts have shown to have high thermal, chemical and electrochemical stability under operating conditions (Gancs et al., 2008). Therefore as well as having greater specific activity, they are also more stable than Pt nanoparticles.

There are several suggestions for the enhanced activity and stability of NSTF catalysts. These include: the nature of the metal/support interaction, enhanced ionic transport, metal faceting, lattice strain and surface defects.

2.5.1.2. Shortcomings of nanostructured thin film catalysts

NSTF catalysts do have some shortcomings. In a study conducted by Sihna et al. (2011) it was found that the catalysts did not perform well at low relative humidity (RH), i.e. dry conditions. Figure 2.17 compares the fuel cell performance of the Pt/C nanoparticles and NSTF catalysts by varying the RH. From Figure 2.17 one can see that the NSTF does not perform well at lower RH values and the Pt/C performs better in these conditions. This is due to their low proton conductivity over Pt surface under dry operation, which reduces catalyst utilization.

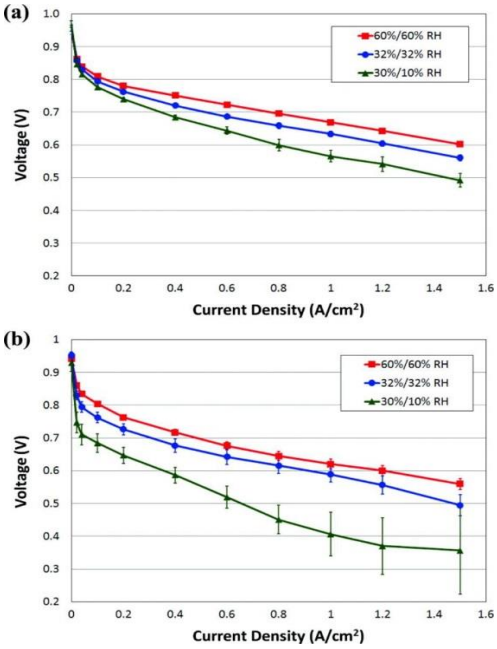

Figure 2.17: (a) Fuel cell performance of 0.4 mg/cm^2 of Pt/C electrodes (b) Fuel cell performance of 0.15 mg/cm^2 NSTF electrodes (Sihna et al., 2011)

2.5.2. Change in catalyst loading for Pt/Pt alloy nanoparticles

When the amount of catalyst metal that is deposited on the carbon support is varied several interesting results are observed.

When the Pt loading is increased, the ECSA decreases due to the agglomeration of Pt particles to form a thin film over the support surface (Schwanitz et al., 2011). This leads to an increase in the specific activity of the catalyst as shown in Figure 2.18. This is due the increase in edges and corner sites which have low coordination numbers. Larger particles have less surface area but they have increased specific activity. An increase in loading also leads to a decrease in the mass activity as shown in Figure 2.18 (a). The trend in the mass activity can be explained by the dispersion of Pt on the surface. Catalysts with high loadings have relatively thick layers or agglomerates, therefore some of the Pt particles do not participate in the ORR (Fabbri et al., 2014).

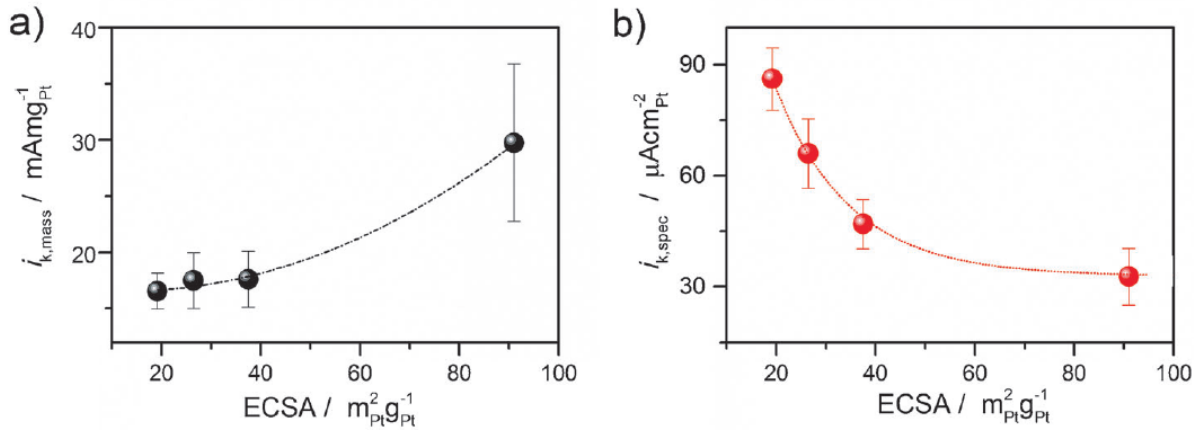

Figure 2.18: The influence of the catalyst loading on the activity of Pt/C catalysts (a) mass activity (b) surface specific activity (Fabbri et al., 2014)

Figure 2.19 illustrates how the mass activity varies with a change in the particle size. From Figure 2.19 it can be seen that there exists an ideal particle size where the mass activity is greatest.

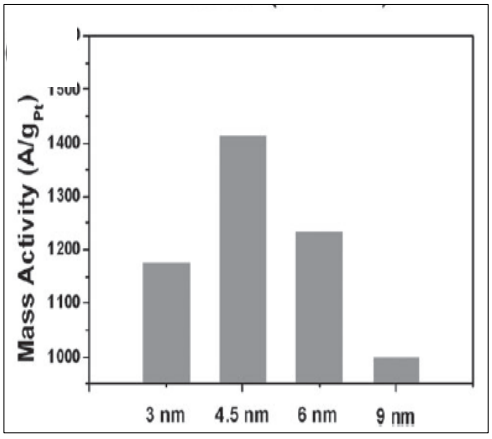

Figure 2.19: Relationship between the mass activity and particle size (Wang et al., 2010)

Gummalla et al. (2015) also investigated the effect of particle size of Pt_3Co/C alloys on the performance of the catalyst. The particle sizes they investigated were 4 .9 nm, 8.1 nm and 14.8 nm. If the particle size is too large then the mass activity is lowered due to poor Pt utilisation. However if the particle is too small then it will not be as stable. Additionally the amount of leached out Co under fuel cell operating conditions is lower for larger particles.

Lower Pt loadings correlate with a greater formation of hydrogen peroxide (Fabbri et al, 2014). This is shown in Figure 2.20 below.

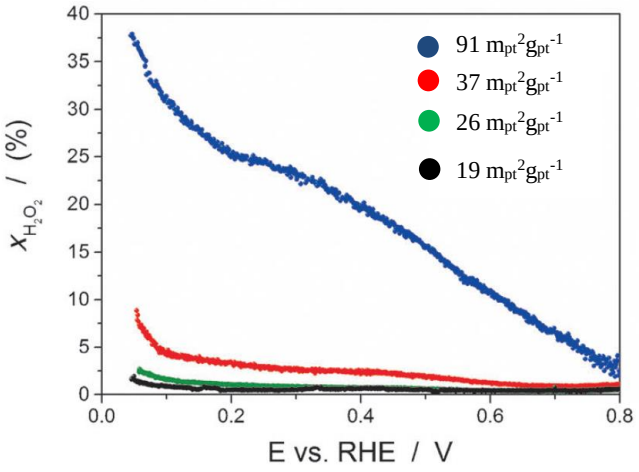

Figure 2.20: Amount of hydrogen peroxide formed with an increase in metal loading (Adapted from Fabbri et al., 2014)

The correlation between the hydrogen peroxide and catalyst is possibly caused by the occurrence of the 2-electron reaction pathway at low loadings with isolated parti cles whereas for high loadings the H_2O_2 formed may be re-adsorbed onto the surface by neighbouring particles to form water (Fabbri et al., 2014). For bulk Pt the 4 – electron pathway dominates (Antoine & Durand, 2000).

2.6. Electrochemical analysis techniques

Diagnostic tools to measure the performance of a fuel cell are an integral part of research. They are essential in the prediction, control and optimisation of the electrochemical and transport processes in a PEFC (Wu et al., 2008). Additionally they can help in distinguishing the structure-property performance relationships between a fuel cell and its components (Wu et al., 2008).

Common electrochemical characterisation techniques include cyclic voltammetry (CV), CO stripping voltammetry, rotating disk electrode and rotating ring disk electrode. The electrochemical instruments used operate by generating an input electrical signal and measuring the corresponding output signal (Zhang et al., 2008). Typically the input and output signals are voltage, current and charge.

2.6.1. Cyclic voltammetry

Cyclic voltammetry (CV) is an important electrochemical analysis technique which offers insight into kinetic and thermodynamic details of a chemical system and provides some experimental information

(Wang et al., 2012(1)). CV can be used to determine the electrochemical surface area. CV is performed with a two or three-electrode arrangement in which the potential relative to a reference electrode is scanned at a working electrode while the resulting current which flows through a counter electrode is monitored (Wang et al., 2012(1)).

The potential of the system is swept back and forth between two set voltage limits whilst the current is recorded (Wu et al., 2008). The sweeping of the potential is carried out linearly and there is a wide range in which the sweep rate can be controlled (Zhang et al., 2008). The curve obtained from a set of CV measurements is known as a cyclic voltammogram. An example of a cyclic voltammogram for a Pt electrode is shown in Figure 2.21. From Figure 2.21 it can be seen that when the voltage potential sweeps past a potential that is related to an electrochemical reaction, the current will increase causing a peak (Wu et al., 2008). The reverse electrochemical reaction will be observed on the reverse scan (Wu et al., 2008). The forward positive sweep represents the oxidation reaction taking place on the anode whilst the backward sweep is the reduction reaction on the cathode.

The shaded area in Figure 2.21 is known as the hydrogen desorption region. This region corresponds to the release of hydrogen ions. The area directly below the hydrogen desorption (H_{des}) region (also known as the hydrogen under potential deposition region, H_{upd}) is known as the hydrogen adsorption (H_{ads}) region. This corresponds to hydrogen adsorbing onto the Pt surface. The oxygen adsorption and desorption areas (O_{ads} and O_{des} respectively) in which oxygen adsorbs and desorbs on the Pt surface are also labelled in Figure 2.21.

The featureless region between the H_{ads} and O_{ads} corresponds to double layer charging. Peaks in this region correspond to impurities such as heavy metal deposition and contaminants (Climent & Feliu, 2011). The multiple peaks observed in the H_{ads} and H_{des} correspond to different Pt orientations i.e. Pt (100), Pt (110) and Pt (111) (Climent & Feliu, 2011).

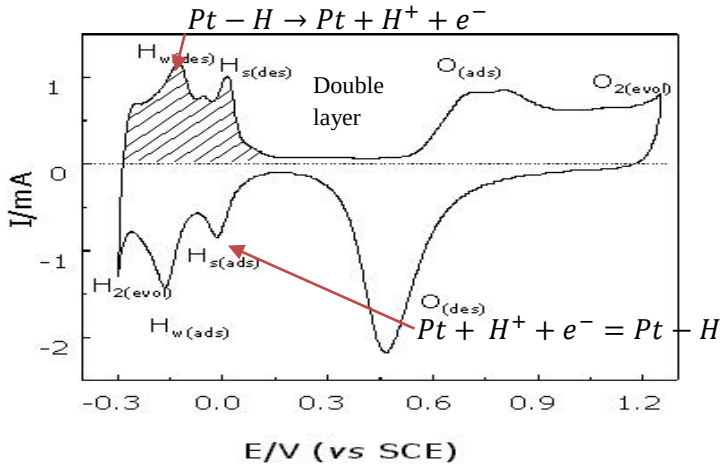

Figure 2.21: Cyclic voltammogram of a Pt electrode in 0.5 M H_2SO_4 solution at a scanning rate of 50 mV/s (Adapted from Ren et al., 2004)

In order to estimate the ECSA using this method a conversion factor is used to estimate the charge in the hydrogen desorption region. That factor is 210 $\mu C/cm^2_{pt}$ and is not an experimental value but a modelled one (Shinozaki et al., 2007).

The disadvantages of using this technique for supported catalysts is that carbon masks the hydrogen adsorption and desorption characteristics e.g. double layer charging and redox behaviour of surface active groups of carbon (Wu et al., 2008).

If particle size is varied the H_{upd} peaks shrink as the particle size is increased as a result of the decrease in specific surface area as shown in Figure 2.22 (Wang et al., 2012(2)).

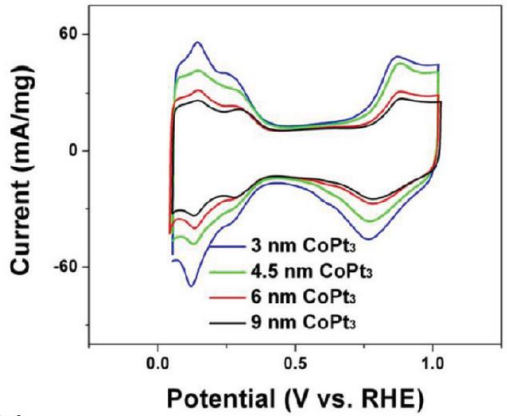

Figure 2.22: The decrease in CV ECSA with an increase in particle size (Wang et al., 2012(2)).

2.6.2. CO stripping voltammetry

CO stripping voltammetry can also be used to determine the ECSA. CO is a poison in fuel cells because it strongly adsorbs on Pt (Wang et al., 2012(1)). This property of CO can be used to determine the ECSA through the oxidation of adsorbed CO at room temperature (Wang et al., 2012(1)). It operates under the same principles as CV. The conversion factor to estimate the ECSA is also a modelled value and found to be 420 $\mu C/cm^2_{pt}$.

It has been found that the CO stripping peak charge can provide information on the active surface sites of the catalyst layer and the CO stripping peak potential can give insight into the composition of an unsupported metal alloy surface (Wu et al., 2008). CO stripping can give rise to double voltammeric peaks with one peak corresponding to a low potential and the other to a high potential (Fabbri et al, 2014). The double peak has been attributed to effect of increasing Pt loading above the threshold of particle agglomeration (Maillard et al., 2005). Pt agglomerates show a high electrocatalytic activity and are accountable for the low potential peak while the high potential peak is attributed to isolated Pt nanoparticles with a lower activity (Maillard et al., 2005). CO stripping is also useful for exploring the reaction mechanism of a metal alloy with enhanced CO tolerance (Wu et al., 2008). Furthermore

exposing the CO to Pt and the subsequent removing of the CO by electrochemical stripping is an excellent method of cleaning and activating Pt (Wu et al., 2008).

2.6.3. Rotating disk electrode and rotating ring disk electrode

2.6.3.1. Rotating disk electrode

Reactants are transported to and from an electrode via diffusion and convection. The dominant transport mechanism for species around the surface of an electrode immersed in a stagnant electrolyte is diffusion (Zhang et al., 2008). Natural convection might also occur owing to the impact of environmental vibration and uneven temperature distribution in the electrolyte. This effect is however minimal (Zhang et al., 2008).

Forced convection can significantly increase the mass transport rate. The convection can be achieved by creating a relative motion of the electrode with respect to the electrolyte (Zhang et al., 2008). The relative movement is created by rotating the electrode. This technique is called the rotating disk electrode (RDE). Supported catalysts are therefore deposited onto a glassy carbon disc and can be readily tested in an ordinary electrochemical glass cell (Mayrhofer et al., 2008). This method is used to determine the kinetic current densities from RDE data using the general mass-transport correlations of the RDE as explained in Section 4. The RDE gives information about the catalytic activity of the ORR (Mayrhofer et al., 2008).

2.6.3.2. Rotating ring disk electrode

Rotating ring disk electrode (RRDE) is a technique for estimating how much H_2O_2 is produced during the ORR as well as the overall ORR activity (Paulus et al., 2001). H_2O_2 can cause damage to the fuel cell (Zhang et al., 2008). If one can quantify the amount of hydrogen peroxide produced during the ORR, the ratio between the four-electron pathway versus two electron reaction pathway can be determined, which is important for screening new catalysts (Paulus et al., 2001).

A RRDE is obtained when a coaxial ring electrode is added outside the disk electrode as shown in Figure 2.23 (Zhang et al., 2008). The ring electrode detects the product that is swept away after being formed at the disk electrode (Zhang et al., 2008). The potential of the ring electrode (E_R) is typically set at a value high enough to cause the immediate reaction of the product coming from the disk electrode (Zhang et al., 2008). The E_R is used to identify the product on the disk electrode and the current (i_R) observed on the ring electrode can also be used to determine how much of the product is formed (Zhang et al., 2008).

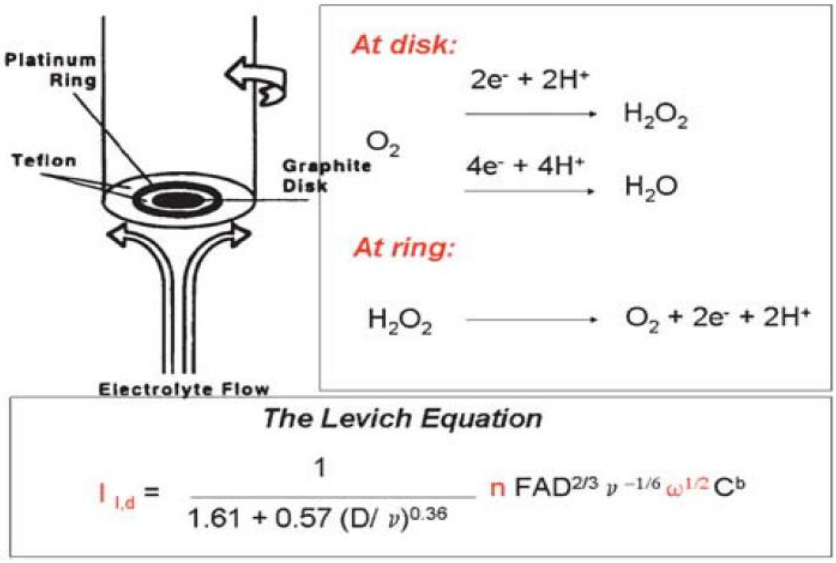

Figure 2.23: Rotating ring disk electrochemistry (Collman & Decreau, 2008)

3. Objectives and Hypotheses

3.1. Problem statement

The kinetics and mechanism of the oxygen reduction reaction still remains one of the main obstacles affecting the performance of a PEM fuel cell and hence the wide scale commercialisation of the technology. A great amount of research has been done in order to understand factors affecting the activity of the reaction. This is necessary if the ultimate goal of reducing the Pt loading used whilst improving the activity and durability of the catalyst can be achieved. Research has shown that alloying of the Pt metal can improve the activity and durability of the catalyst. At the same time the exact role of particle size, metal loading and surface morphology in the ORR is still a topic of debate. It is essential to understand how particle size and surface morphology affect the reaction mechanism and kinetics of the ORR when Pt-Co alloys are used. Combining the effects of alloying with extended surfaces can lead to effective catalysts with reduced Pt loadings.

3.2. Objectives

The aims of this study are therefore to:

- Investigate the effect of increasing the loading of Pt_3Co on a carbon support on the particle size, interparticle distance and surface morphology.
- Investigate the effect of increasing the loading of Pt_3Co on a carbon support on the surface and mass specific activity for the ORR.

The hypotheses guiding this study are then as follows:

- As the loading of the Pt/Pt-Co metals is increased the particle size will increase as the metals agglomerate on the carbon support.
- The specific activity will increase and the mass activity will decrease as the loading is increased due to the particle size effect. This will be observed for both Pt and Pt-Co catalysts.
- At all loadings/surface morphologies Pt-Co alloys will demonstrate higher mass and specific activities than Pt.

3.3. Key Questions

The key questions that this study aims to investigate therefore are:

- What is the particle size and surface morphology as the Pt-Co loadings are increased?
- What are the trends in specific and mass activity of the catalyst as the Pt-Co loadings are increased?
- What is the relationship between increased loading and hydrogen peroxide formation for Pt-Co catalysts?

4. Experimental plan

This section below outlines the experimental plan followed in order to produce the catalysts as well as to conduct physical and electrochemical characterisation. All catalysts were prepared at the University of Cape Town in the Department of Chemical Engineering. The Table 4.1 shows all the chemicals and gases used in this study.

Table 4.1: List of chemicals and gases used

Chemical	Chemical Formula	Supplier	Purity/Composition
Platinum acetylacetonate	$Pt(C_5H_7O_2)_2$	Sigma-Aldrich	97 %
Cobalt (II) chloride hexahydrate	$CoCl_2.6H_2O$	Sigma-Aldrich	98 %
Alumina powder			
Nafion solution (alcoholic based)	-	Ion Power	5 wt. %
Isopropanol	C_3H_7OH	Kimix Chemicals	99.9 %
Ultra-pure water	H_2O	Millipore, 18.2 Ω	100 %
Perchloric acid	$HClO_4$	Sigma-Aldrich	70 %
Sulphuric acid	H_2SO_4	Kimix Chemicals	95 %
Hydrogen peroxide	H_2O_2	Sigma-Aldrich	35 %
Vulcan XC-72R	C	Electrochem Inc.	-
Argon	Ar	Air Liquide	99.999 %
Oxygen	O_2	Afrox	99.998 %
Carbon monoxide	CO	Afrox	95%
Hydrogen	H_2	Air Liquide	99.999 %
Argon-Hydrogen Mixture	Ar, H_2	Air Liquide	5 vol.% H_2 and 95 vol.% Ar

4.1. Thermally induced chemical deposition

All catalysts were prepared by the thermal decomposition of metal organic precursors. The Pt precursor used was platinum acetylacetonate ($Pt(acac)_2$) and the cobalt precursor was cobalt chloride hexahydrate ($CoCl_2.6H_2O$). The Pt alloy prepared was Pt_3Co/C. Pt/C catalysts were also prepared with the same total metal loading as Pt_3Co/C. The various masses that were weighed out to make the catalysts are shown in Table 4.2 below.

Table 4.2: Precursor and carbon measurements

Catalyst	Metal loading (wt. %)	Vulcan XC-72R (mg)	$Pt(acac)_2$ (mg)	$CoCl_2.6H_2O$ (mg)
Pt/C	20	125	63.0	-
	40	125	168.0	-
	60	125	378.0	-
	80	50	403.2	-
	90	50	907.2	
Pt_3Co/C	20	125	57.2	11.5
	40	125	152.6	30.8
	60	125	343.4	63.3
	80	50	366.3	73.9

To prepare each Pt/C catalyst, the masses in Table 4.2 were weighed into a graphite boat and placed in a stainless steel tube as shown in Figure 4.1. The tube was inserted into a tubular furnace and an argon gas was flown through it at 100 ml/min. The temperature of the furnace was raised to 100 °C in 30 minutes and then held at that temperature for a further 30 minutes. This is to remove all the water from the sample. The gas lines at the entrance and exit of the reactor were then closed, to maintain an argon atmosphere inside the reactor chamber. The temperature was then ramped to 350 °C in an hour and the temperature was maintained at 350 °C for a further hour. This was the end of the procedure. The furnace was cooled and once the furnace reached room temperature the catalyst was removed from the furnace. The Pt/C catalysts were then ready for electrochemical and physical characterisation whilst the alloy catalysts were further processed. A similar procedure was followed for the Pt_3Co/C, however, they were synthesized at different furnace conditions. The furnace was raised to 100 °C in 30 minutes and then held at that temperature for a further 30 minutes. The temperature was then ramped to 450 °C in an hour and the temperature was maintained at 450 °C for a further two hours.

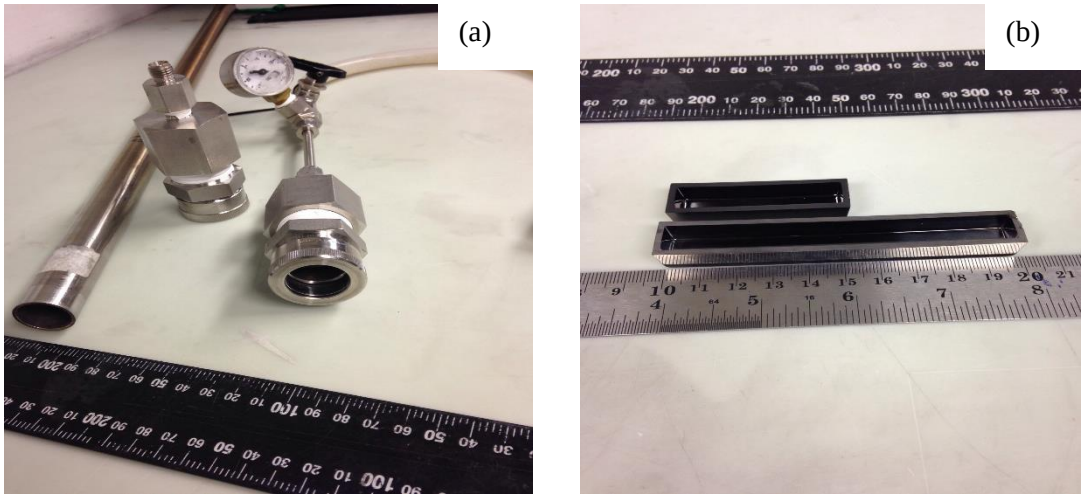

Figure 4.1: Illustration of the (a) stainless steel tube (b) graphite boat in which the thermally induced chemical decomposition occurred.

4.2. Heat treatment

The alloy samples were treated using temperature controlled reduction (TPR) in a Micromeritics Autochem HP II 2950 Chemisorption Analyser. Each sample was placed in a U-shaped glass tube, sealed off with quartz wool and placed in a furnace with a thermocouple to measure the temperature of the sample. The temperature was ramped to 120 °C at 10 °C/min under Argon gas (50 ml/min and 1.01 bar) and held at that temperature for 60 minutes to remove any water and then cooled down to 60 °C at 10 °C/min. The gas was changed and a gas mixture of 5 vol. % H_2 and 95 vol. % Ar , was flowed through the tube at 50 ml/min and 1.01 bar. The temperature was taken to 900 °C at 10 °C/min and held at that temperature for 2 hours. The gas was switched back to Argon (50 ml/min and 1.01 bar) and the furnace was cooled to ambient. The alloy samples were then ready for physical characterisation.

4.3. Leaching

After heat treatment it was necessary to pre-leach the alloys. The alloy powder was stirred with 100 ml 0.5 M H_2SO_4 acid (Sigma-Aldrich) and heated at 80 °C under reflux for 24 hours. The sample was rinsed using ultrapure water (18.2 MΩ.cm deionised water) several times. The pH of the rinsed water was checked to ensure that all the acid had been removed from the powder. The alloy was dried in an oven at 40 °C for 2 hours. The alloy sample was then ready for electrochemical and physical characterisation.

4.4. Electrochemical characterisation

4.4.1. Cell setup and experiment preparation

Electrochemical characterisation was carried out in a three-compartment electrochemical cell (Gamry Instruments) as shown in Figure 4.2 below. A SP-300 bipotentiostat (Bio-logic Science Instruments) and rotation control (Gamry instruments) were used. The counter electrode used was a Pt coil and the reference electrode was a $Hg/HgSO_4$ reference electrode used in an electrolyte filled Luggin capillary (Gamry Instruments). All potentials were reported in terms of the reversible hydrogen electrode scale (RHE). The electrolyte solution was 0.1. M $HClO_4$ and was used in all experiments. It was prepared using ultra-pure water (18.2 MΩ.cm deionised water) and concentrated $HClO_4$ (Sigma Aldrich).

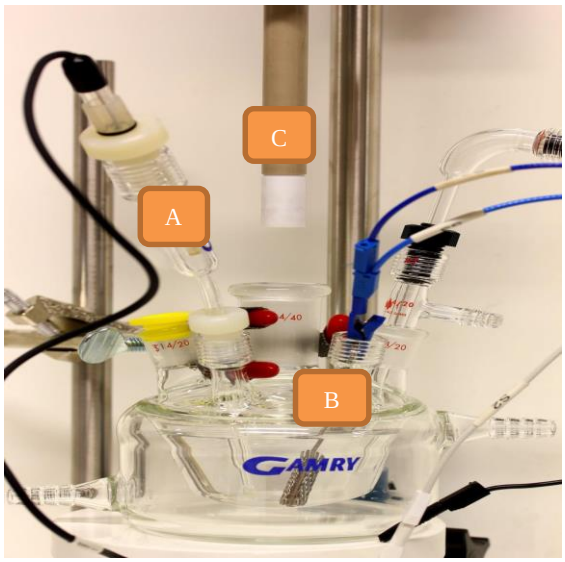

Figure 4.2: Three-compartment electrochemical cell (Gamry Instruments) with (a) Luggin capillary (b) Pt coil (c) glassy carbon working disk electrode (Pine instruments) (Adapted from Taylor et al. (2013)

All glassware was cleaned before use. The glassware was submerged in a 1:3 (volume ratio) solution of hydrogen peroxide (Sigma-Aldrich) and concentrated sulphuric acid (Kimix chemicals) respectively, and left to soak overnight. The clean glassware was removed from the cleaning solution and rinsed several times (minimum of 10 rinses for each piece of glassware) using ultra-pure water (18.2 MΩ.cm deionised water). When handling the H_2O_2/H_2SO_4 solution, in addition to wearing nitrile gloves, heavy duty rubber gloves, a face shield and an apron were worn for additional protection.

The 5.61 mm diameter (outer diameter, OD) glassy carbon (GC) working electrode (Pine instruments, E7R9 Series) was used for RRDE measurements. Before an ink was deposited onto the GC electrode it was thoroughly polished to a mirror finish using first a 1 µm alumina solution (Buehler) for 2 minutes in a "number 8" pattern. It was then rinsed with ultra-pure water (18.2 MΩ.cm deionised water). This was followed by polishing in a 0.05 µm alumina solution (Buehler) for a further 2 minutes. The GC was rinsed in ultra-pure water (18.2 MΩ.cm deionised water) and then sonicated for a minute in each of the following solutions in this order:

ultra-pure water ⟶ isopropanol ⟶ ultra-pure water

It was then allowed to dry at ambient conditions before catalyst ink was deposited.

Surface impurities were removed from the Pt coil counter electrode by holding it in the flame of a blow torch for 15 seconds and immediately rinsing it with ultra-pure water (18.2 MΩ.cm deionised water). This was done to cool the coil before inserting it into the electrochemical cell.

The reference electrode was calibrated each day before use. Calibration was done using the hydrogen oxidation/reduction reaction on a Pt working electrode. 0.1 M $HClO_4$ acid was prepared and poured in the three-compartment cell. H_2 gas was bubbled through the cell for 30 minutes to fully saturate the solution with the gas. The reference electrode was then placed in the cell as well as the counter electrode. A voltmeter was then used to measure the potential between the reference electrode and the counter electrode. The measured voltage was used as the reference point for all electrochemical characterisation that day.

Characterisation was then carried out sequentially in the following order:

Cyclic voltammetry ⟶ RDE ⟶ RRDE ⟶ CO stripping

A fresh solution of electrolyte was prepared before a set of electrochemical measurements was carried out.

4.4.2. Cyclic voltammetry

Cyclic voltammetry was used to determine the ECSA of a catalyst sample. Additionally it was necessary to clean the catalyst surface of any impurities. The electrolyte was deoxygenated with argon gas by bubbling the electrolyte for 30 minutes. Before the working electrode was inserted into the electrolyte the bubble flowrate was reduced slightly to prevent bubbles forming on the surface of the working electrode during measurements. After insertion of the working electrode, its potential was cycled between 0.05 and 1 V vs. RHE at 100 mV/s for ≥50 cycles. The scan rate was then reduced to 20 mV/s and cycled between 0.05 and 1 V vs. RHE for 5 cycles.

The final cycle taken at a scan rate of 20 mV/s was used to estimate the ECSA. The voltammogram was analysed by integration and averaging the charge estimated in the hydrogen desorption region. In this region it was assumed that the charge associated with a polycrystalline Pt surface was 210 $\mu C/cm^2_{pt}$ (Trasatti & Petrii, 1991). This was used to estimate the ECSA in "cm^2_{pt}/g_{pt}". Equations 4.1 illustrates this.

$$ECSA\left(\frac{cm^2_{pt}}{g_{pt}}\right) = \frac{charge\ (\mu C)}{210\left(\frac{\mu C}{cm^2_{pt}}\right).catalyst\ loading(g_{pt})} \quad (4.1)$$

4.4.3. Linear sweep voltammetry (rotating disk electrode and rotating ring disk electrode)

Rotating disk electrode tests are necessary to determine the activity of the catalyst. After cyclic voltammetry whilst argon gas is still bubbling through the cell, a background current for the rotating disk electrode was recorded. The background current is the capacitive current. It is necessary to remove any contributions of capacitive current, by subtracting it from the ORR current.

At varying rotation speeds i.e. 400, 900, 1600 and 2500, capacitive current curves are recorded as the potential of the working electrode is swept linearly. The potential is swept from 1.0 V to 0 V vs. RHE at 20 mV/s. This is known as the cathodic sweep. The reverse sweep is also measured from 0 V to 1.0 V vs. RHE. This is known as the anodic sweep.

In order to obtain the experimental ORR curves, the gas was switched to oxygen and the bubble flowrate was increased. The electrolyte was saturated with oxygen by bubbling for 30 minutes. The procedure followed when the background current curves were obtained was repeated, i.e. potential sweeping under rotation control. The cathodic sweep was used to determine the activity of the catalysts. In analysing the cathodic sweep data, the experimental diffusion limiting current (i_d) was compared to a theoretical value ($i_{d,\,theoretical}$). The i_d was seen as the flat section of the experimental cathodic sweep and was taken to be the minimum value in that section of the curve. The $i_{d,\,theoretical}$ was calculated using the Levich equation shown below.

$$i_{d,theoretical} = 0.62nFAD^{\frac{2}{3}}\omega^{\frac{1}{2}}\nu^{-\frac{1}{6}}C \tag{4.2}$$

Where: *n* is the number of electrons transferred in the half reaction, F is the Faraday constant, A is the electrode area, D is the diffusion coefficient, ω is the angular rotation speed of the working electrode, ν is the kinematic viscosity of the solution and C is the reactant concentration.

In the Table 4.3 below, the theoretical values of the diffusion limiting current compared with different rotation speeds are shown. The table shows values for both the 5.61 mm (OD) glassy carbon working electrode (Pine instruments, E7R9 Series) and the 5 mm (OD) glassy carbon working electrode (Pine instruments, E3 Series).

Table 4.3: Summary of theoretical diffusion limiting currents for 5.61 mm (OD) working electrode (Pine Instruments, E7R9 series) and 5 mm (OD) working electrode (Pine Instruments, E3 series)

		$I_{d,theorectical}$			
		5.61 mm (OD)		**5 mm (OD)**	
Rotation speed,ω (rpm)	**Rotation speed,ω (rad/s)**	**(mA)**	**(mA/cm^2)**	**(mA)**	**(mA/cm^2)**
400	41.9	0.747	3.02	0.593	3.02
900	94.2	1.12	4.53	0.890	4.53
1600	168	1.49	6.04	1.19	6.04
2500	262	1.87	7.55	1.48	7.55

The Koutecky-Levich equation shown below was subsequently used to calculate the kinetic current (i_k) using the experimental cathodic sweep at 1600 rpm.

$$\frac{1}{i} = \frac{1}{i_k} + \frac{1}{i_d} \tag{4.3}$$

Where: i is the measured current and i_d is the experimental diffusion limiting current. The kinetic current ($i_{k,\,0.9}$) at 0.9 V vs. RHE was then normalised by the ECSA in order to obtain the specific activity ($i_{k,\,spec}$). Similarly, the mass specific activity ($i_{k,\,mass}$) was calculated by normalisation of the kinetic current ($i_{k,\,0.9}$) at 0.9 V vs. RHE by the mass of the catalyst metal on the electrodes.

Where rotating ring disk measurements were needed they were taken in conjunction with the rotating disk electrode measurements in an oxygen saturated electrolyte. Using a bipotentiostat (Bio-logic Science Instruments), the ring was set at a potential of 1.2 V vs. RHE throughout all the disk measurements described above. The collection efficiency (N) of the ring was taken to be 0.37 (Pine Instruments).

In order to calculate the number of electrons exchanged during the ORR (consider 1 molecule of O_2). The mass balance equations and the charge were used as demonstrated in the equations below. Note that 2-electron current is from the formation of H_2O_2 and 4-electron currents from the formation of H_2O on the disk (Antoine and Durand, 2000).

$$i_{2e^-} = \frac{i_{ring}}{N} \tag{4.4}$$

$$i_{disk} = i_{2e^-} + i_{4e^-} \tag{4.5}$$

$$\frac{i_{disk}}{n} = \frac{i_{2e^-}}{2} + \frac{i_{4e^-}}{4} \tag{4.6}$$

Therefore:

$$n = \frac{4.i_{disk}}{i_{disk}+\frac{i_{ring}}{N}} \quad (4.7)$$

Where: n is the average number of electrons exchanged during the reduction of a molecule of oxygen, i_{ring} is the current measured at the ring, i_{disk} is the current measured on the disk and N is the collection efficiency.

The ratio ($X_{H_2O_2}$) of a molecule of hydrogen peroxide formed per molecule of oxygen consumed was calculated as shown in the equation below.

$$X_{H_2O_2} = \frac{2i_{ring}/_N}{i_{disk}+i_{ring}/_N} \quad (4.8)$$

The ratio ($X_{H_2O_2}$) was plotted against the percent weight loading of the catalysts.

4.4.4. CO stripping

CO stripping was used as an alternate method to determine the ECSA. The working electrode was held at a potential of 0.1 V vs. RHE while the electrolyte was saturated with CO for 20 minutes. This is the potential at which CO adsorbs to the catalyst surface. The gas was then changed and Ar was bubbled into the electrolyte for 20 minutes in order to purge the CO. The potential was still held at 0.1 V vs RHE in this interval. Five cyclic voltammograms were then recorded at a sweep rate of 20 mV/s from 0 to 1.0 V vs. RHE. The first sweep corresponds to the oxidation of CO from the catalyst surface and the subsequent sweeps were cyclic voltammograms free from CO. The ECSA was calculated the equation below and assuming 420 μC/cm^2_{pt} per monolayer of CO adsorbed onto the catalyst metal surface.

$$ECSA\left(\frac{cm^2{}_{pt}}{g_{pt}}\right) = \frac{charge(\mu C)}{420\frac{\mu C}{cm^2{}_{pt}} \times catalyst\ loading(g_{pt})} \quad (4.9)$$

4.5. Physical characterisation

4.5.1. Transmission electron microscopy

Transmission electron microscopy (TEM) measurements were carried out at the Electron Microscope Unit at the University of Cape Town using a F20-FEI Tecnai™ operating at 200 kV. TEM was used to examine the particle dispersion and nanoparticle size on the carbon support. The samples were prepared by mixing a small amount in acetone with the sample and then sonicating this mixture for *ca*. 10 minutes. The sonicated mixture was then pipetted onto a copper coated grid for analysis. The grid was then placed under a lamp for a few seconds to evaporate the acetone. The sample was then ready for analysis. Particle sizes were determined manually with the assistance of ImageJ software.

4.5.2. Energy-dispersive X-ray spectroscopy

Energy-dispersive X-ray spectroscopy (EDX) coupled to a Scanning Electron Microscope (SEM) was carried out at the Electron Microscope Unit at the University of Cape Town on a FEI Field Emission Nova NanoSEM 230, using an Oxford X-Max detector and INCA software, at 30 kV. The samples were sprinkled onto a carbon tape and were ready for analysis. This technique was used to determine the Pt: Co ratio in the alloy.

4.5.3. Thermogravimetric analysis

Thermogravimetric analysis (TGA) was employed to confirm the weight percentage of the Pt/Pt_3Co in the prepared catalysts. Using the Mettler-Toledo TGA/SDTA851^e, the mass of a sample was monitored as a function of temperature.

The mass of the sample holder, i.e. a crucible and its lid, was determined initially. 2 to 3 mg of catalyst was placed in the weighed crucibles. The temperature of the sample was increased from 25 °C to 800 °C at 10 °C/min in an atmosphere of air. A corresponding mass was recorded for an increase in temperature. In this environment the carbon oxidises completely, leaving only the catalyst metal in the crucible. The mass of initial sample and the final metal mass are used to calculate the particle loading using the equation below:

$$\frac{Final\ sample\ mass}{Initial\ sample\ mass} \times 100 = \text{metal}\ loading\ wt.\% \tag{4.10}$$

4.5.4. X-ray diffraction

X-ray diffraction was used to determine the average crystallite size by line broadening analysis using the Scherer equation (Equation 4.11). Analysis was done on a Bruker D8 Advance diffractometer with a Cu Kα radiation source operating at 40 kV. The sample was placed in a sample holder and the x-ray angle (2θ) was increased from 20 ° to 130°.

$$< L >= \frac{\kappa\lambda}{\beta cos\theta} \tag{4.11}$$

Where: <L> is a measure for the dimension of the particle in the direction perpendicular to the reflecting plane; K is a dimensionless shape factor approximately equal to 1; λ is the X-ray wavelength; β is the peak width and θ is the angle between the beam and the normal on the reflecting plane.

5. Results and discussion

The following section describes the results from the physical and electrochemical characterisation that was carried out. Section 5.1 details the results from a benchmarking study of a commercial 40 wt. % Pt/C catalysts which was tested using the electrochemical setup described in Section 4 of this report. This was done to ensure the reproducibility of the results and to demonstrate that the system is functioning correctly. Section 5.2 shows the thermogravimetric analyses conducted on the precursors. Section 5.3 details the results of an ink drying optimisation procedure. Sections 5.4 details the results of the electrochemical and physical characterisation of the Pt/C catalysts prepared using thermally induced chemical deposition. Section 5.5 details the results of the Pt_3Co/C including the physical and electrochemical characterisation. Finally, Section 5.6 provides a comparison of the main findings from the Pt/C and the Pt_3Co/C catalysts that were prepared.

5.1. Benchmarking

Benchmarking experiments were conducted three times on a commercial 40 wt. % Pt/C catalyst using a 5 mm (OD) glassy carbon working electrode (Pine instruments, E3 Series) and as described in Section 4. These results are shown below.

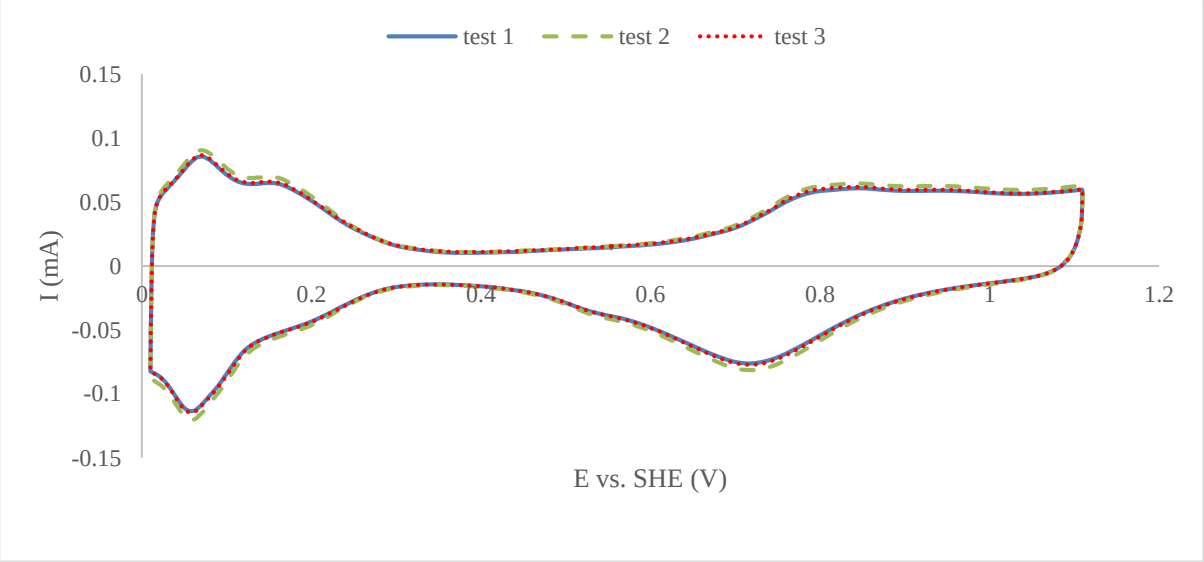

Figure 5.1: Three cyclic voltammetry experiments measured separately for a commercial 40 wt. % Pt/C catalyst. Cyclic voltammetry was carried out in an Ar saturated 0.1 M $HClO_4$ solution at room temperature at a sweep rate of 50 mV/s.

The results of three cyclic voltammetry experiments performed using a 40 wt. % Pt/C commercial catalyst are shown in Figure 5.1. The voltammograms are very similar. The experimentally calculated ECSA is shown in the Table 5.1. The ECSA values calculated are within a reasonable range from each demonstrating the reproducibility of the experiment.

Table 5.1: Experimental ECSA of a commercial catalyst

40 wt. % Commercial Catalyst	ECSA Experimental (m^2_{Pt}/g_{Pt})
Test 1	49.3
Test 2	52.7
Test 3	50.6

Figure 5.2 and Table 5.2 show the results of linear sweep voltammetry carried out on the commercial catalyst in an oxygen saturated 0.1 M $HClO_4$ solution at room temperature.

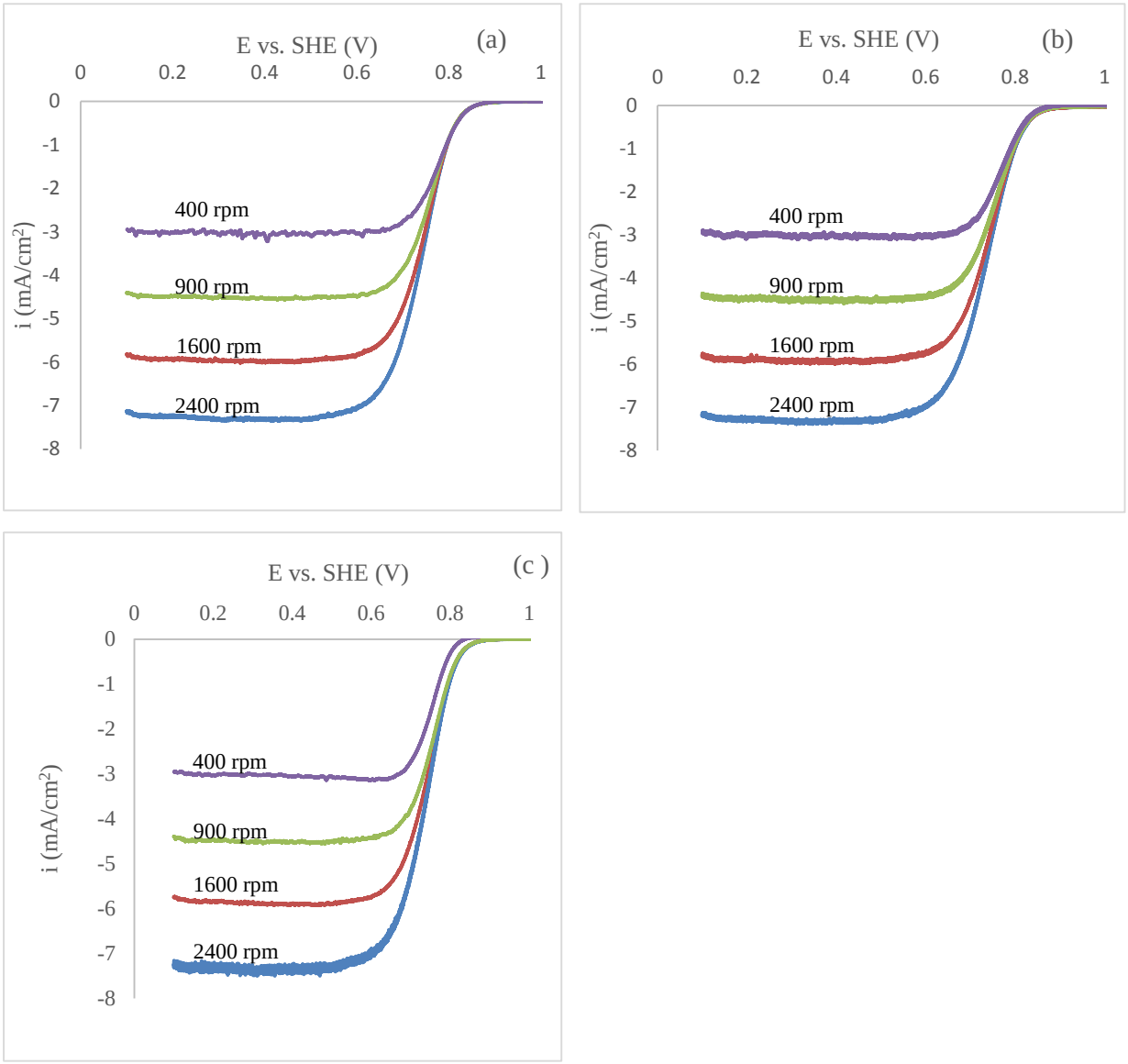

Figure 5.2: Linear sweep voltammetry of a commercial catalyst (a) test 1 (b) test 2 (c) test 3. The oxygen reduction current densities for the cathodic sweeps (5 mV/s, 1600 rpm) of the catalysts were recorded in an oxygen saturated 0.1 M $HClO_4$ solution at room temperature

Table 5.2 shows that the values for the diffusion limiting currents obtained for a commercial catalyst are comparable with each other and well within range of the theoretical diffusion limiting currents at varying rotation speeds. This demonstrates that the 0.1 M $HClO_4$ solution was sufficiently saturated with O_2 and further indicates that the system is reliable.

Table 5.2: Experimentally measured diffusion limiting current values of a 40 wt. % commercial catalyst compared to the theoretical values

	5 mm (OD)			
Rotation speed, ω (rpm)	**Theoretical i_d (mA/cm^2)**	**test 1 i_d (mA/cm^2)**	**test 2 i_d (mA/cm^2)**	**test 3 i_d (mA/cm^2)**
400	3.02	3.22	3.11	3.15
900	4.53	4.57	4.59	4.56
1600	6.04	6.02	6.00	6.21
2500	7.55	7.36	7.39	7.75

5.2. Thermogravimetric analyses (TGA) of precursors

In order to make the Pt/C catalysts via thermally induced chemical deposition, platinum acetylacetonate ($Pt(acac)_2$) was the metal organic precursor used. Its decomposition is shown in Figure 5.3 using thermogravimetric analysis in an inert atmosphere. From Figure 5.3 the decomposition window is 197 – 270 ° C was taken from the raw data. The mass loss observed in this temperature window corresponds with the mass loss from the initial amount of $Pt(acac)_2$ loaded to the corresponding Pt metal weight. Therefore the Pt/C catalysts were prepared in an inert environment (Ar) at 350 °C to ensure decomposition of the precursor.

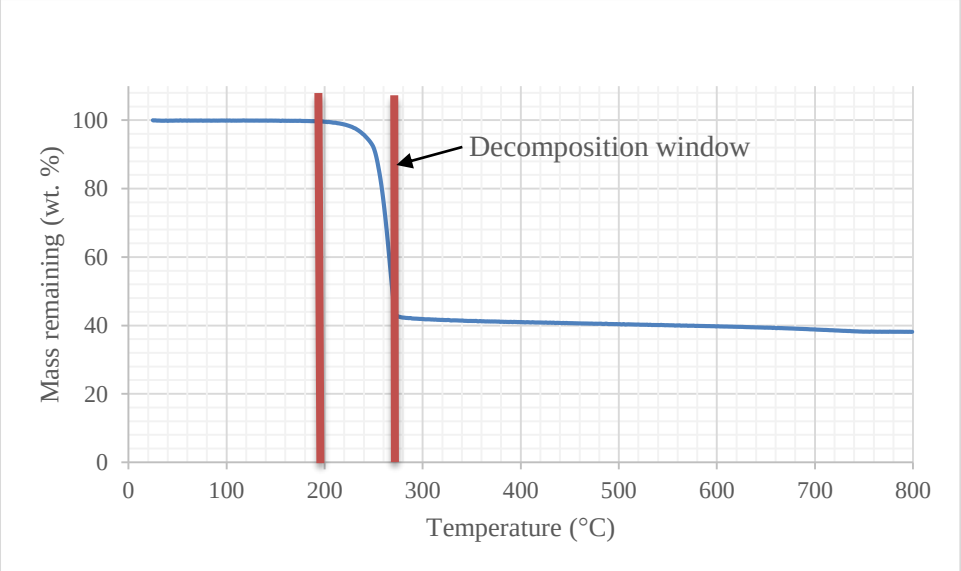

Figure 5.3: Thermogravimetric analysis of platinum acetylacetonate.

Figure 5.4 shows the thermogravimetric analysis of $CoCl_2.6H_2O$. The decomposition window is 57 – 187 ° C.

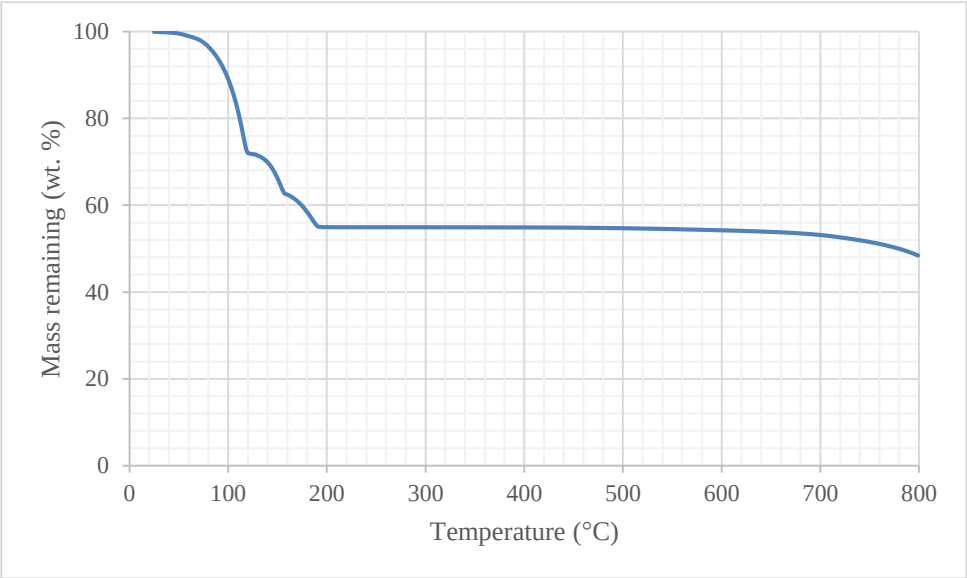

Figure 5.4: Thermogravimetric analysis of Cobalt (II) chloride hexahydrate

Other possible Co metal sources were also investigated. These are cobalt acetate and cobalt acetylacetonate. The thermogravimetric analyses of them is shown in Figure 5.5.

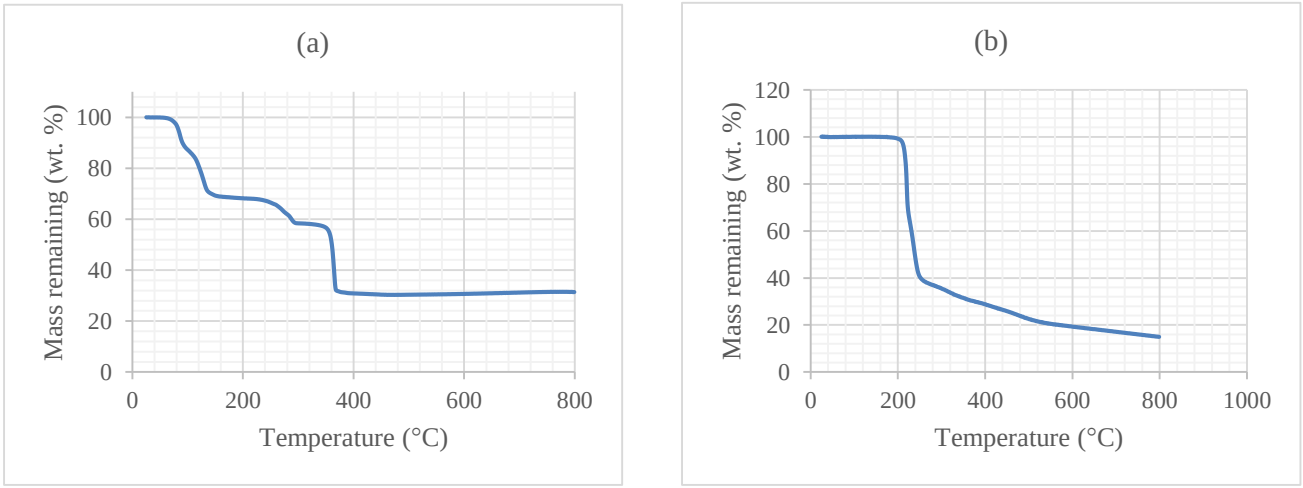

Figure 5.5: Thermogravimetric analysis of (a) Cobalt acetate (b) Cobalt acetylacetonate

Figure 5.5 shows that the decomposition of cobalt acetate occurs over a relatively wide temperature range (70 – 370 °C) compared to that of $Pt(acac)_2$ therefore it was not selected. The main decomposition window of cobalt acetylacetonate occurs in the narrow range of 202 – 252 °C. However the decomposition continues gradually beyond that temperature and even at 800 °C, the compound has not fully decomposed to Co metal therefore this precursor was not selected for the preparation of the alloys.

5.3. Optimisation of ink drying methodology

As explained in Section 4 before electrochemical characterisation could begin an electrode with a thin catalyst film needs to be prepared as described by Garsany et al. (2011). Section 4 describes the ink preparation and drying method used. Other drying methods were investigated to find the optimal drying method that would give consistently good films. The other drying methods that were explored were: in an oven at 60 ° C with a beaker over the electrode, on a rotating shaft at 700 rpm, in a fume hood with air flow and drying the ink with a beaker over the electrode. The images of the ink films produced are shown in Figure 5.6. Ink dried under a beaker on a lab bench gave the most reproducible results and consistently the largest ECSA. This was because the formation of a uniform film was made possible by slow evaporation of the solvents.

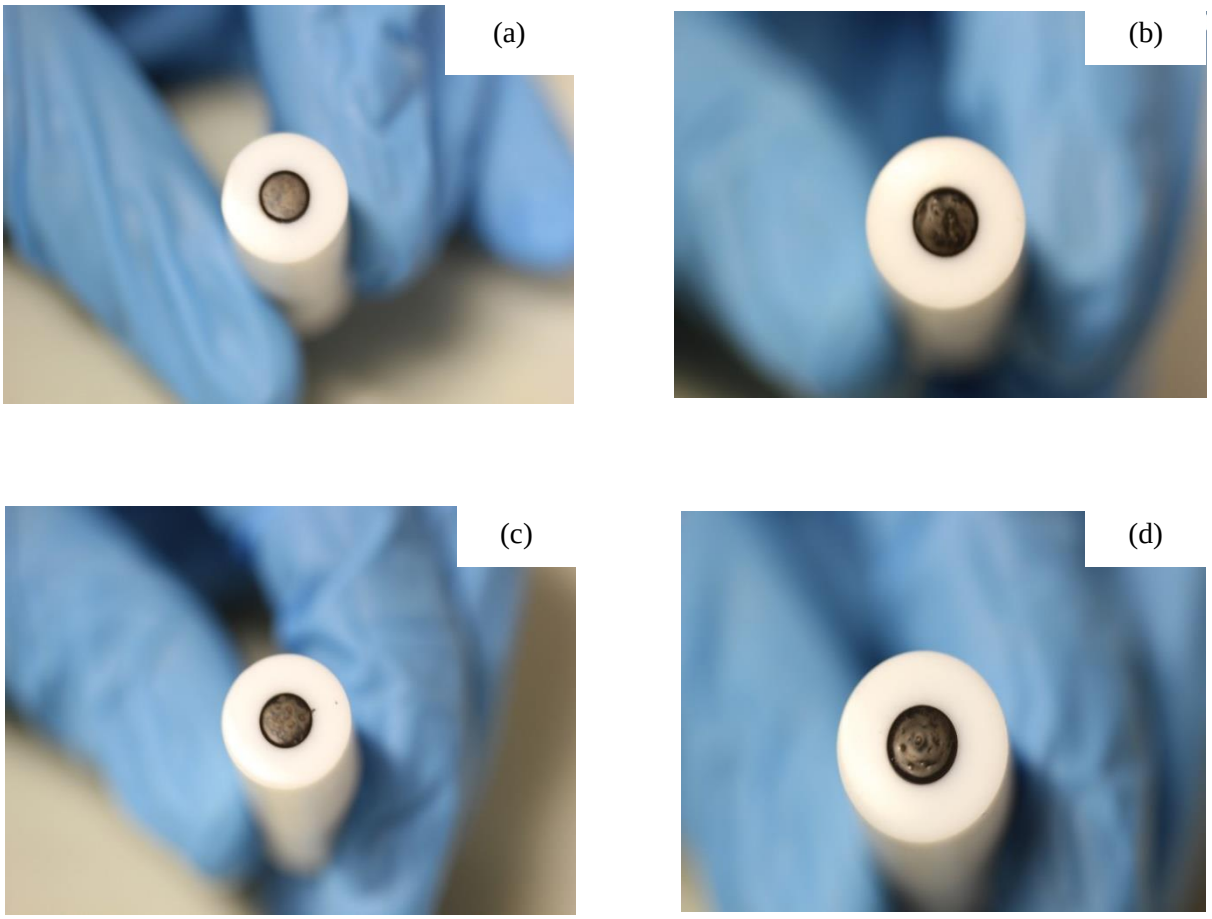

Figure 5.6: Results from ink drying experiment. (a) Ink dried on a lab bench with a beaker over the electrode. (b) Ink dried in a fume hood with hood pulled down to allow for air flow. (c) Ink dried in an oven at 60 °C with a beaker over the electrode. (d) Ink dried on a rotating shaft at 700 rpm.

5.4. Analyses of the Pt/C results

Section 5.4 presents the physical and electrochemical characterisation of the Pt/C catalysts which were prepared using thermally induced chemical deposition at varying loadings, i.e. 20, 40, 60 and 80 wt. %.

5.4.1. XRD

XRD analysis was carried out on the Pt/C catalyst. The results of the analyses are shown in Figure 5.7.

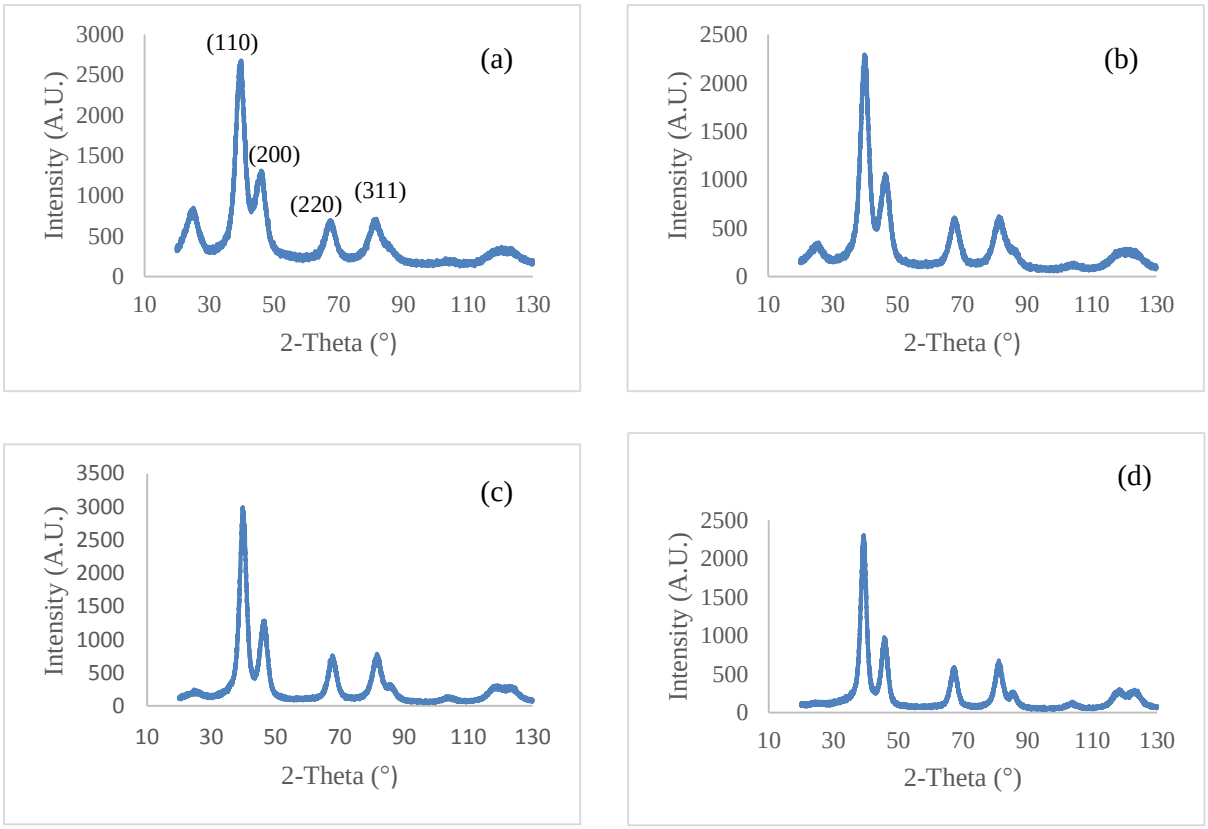

Figure 5.7: XRD graphs for Pt/C catalysts (a) 20 wt. % (b) 40 wt. % (c) 60. wt. % (d) 80 wt. %

The initial peak found at 25 ° (2-Theta) is associated with carbon and becomes relatively smaller with an increase in metal loading. The other peaks corresponding to the planes (110), (200), (220) and (311) as shown in Figure 5.7(a) were identified by comparison to values found in literature (Pozio et al., 2002). The d-spacings are shown in Table 5.3 . The literature value of the d-spacing of a Pt/C (110) plane is 2.27 Å (Pozio et al., 2002). The values in Table 5.3 are in close agreement with the literature value.

Table 5.3: D-spacings for the Pt/C catalysts

Pt (wt. %)	D-spacing (Å) Pt(110)
20	2.26806
40	2.26324
60	2.25838
80	2.27293

Using the Scherrer equation as described in Section 4, the particle sizes of the Pt/C catalysts were calculated and the results are shown on Table 5.4 below.

Table 5.4: Average crystallite size (nm) of Pt/C catalysts. Particle sizes calculated using the Scherrer equation.

Wt. % Pt	Average crystallite size from XRD (nm) (220)
20	2.77
40	2.89
60	3.39
80	3.50

The results from Table 5.4 show that the average crystallite size is increasing but not by a large margin as the loading of Pt is increased. This is as expected as at higher loadings there is a higher probability that particles agglomerate to form bigger ones.

5.4.2. TEM analysis

Figure 5.8 shows the TEM images for the different loadings.

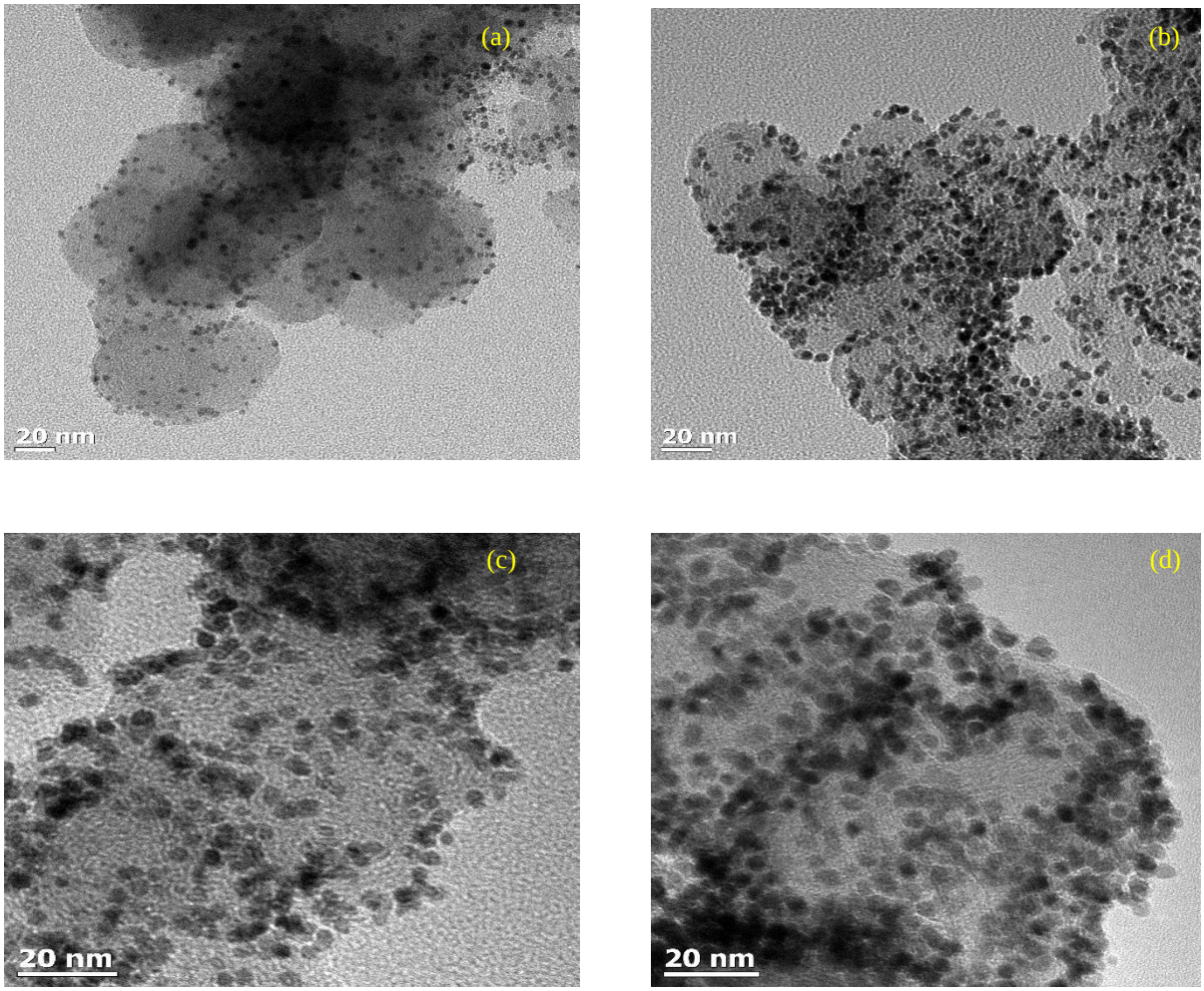

Figure 5.8: Tem images of Pt/C (a) 20 wt. % (b) 40 wt. % (c) 60 wt. % (d) 80 wt. %

The TEM images show that the Pt particles are homogenously spread across the carbon support. As the wt. % Pt is increased, there does not appear to be a significant amount of agglomeration occurring.

Figure 5.9 shows the particle size distribution of the Pt/C catalysts calculated using TEM images of the catalysts.

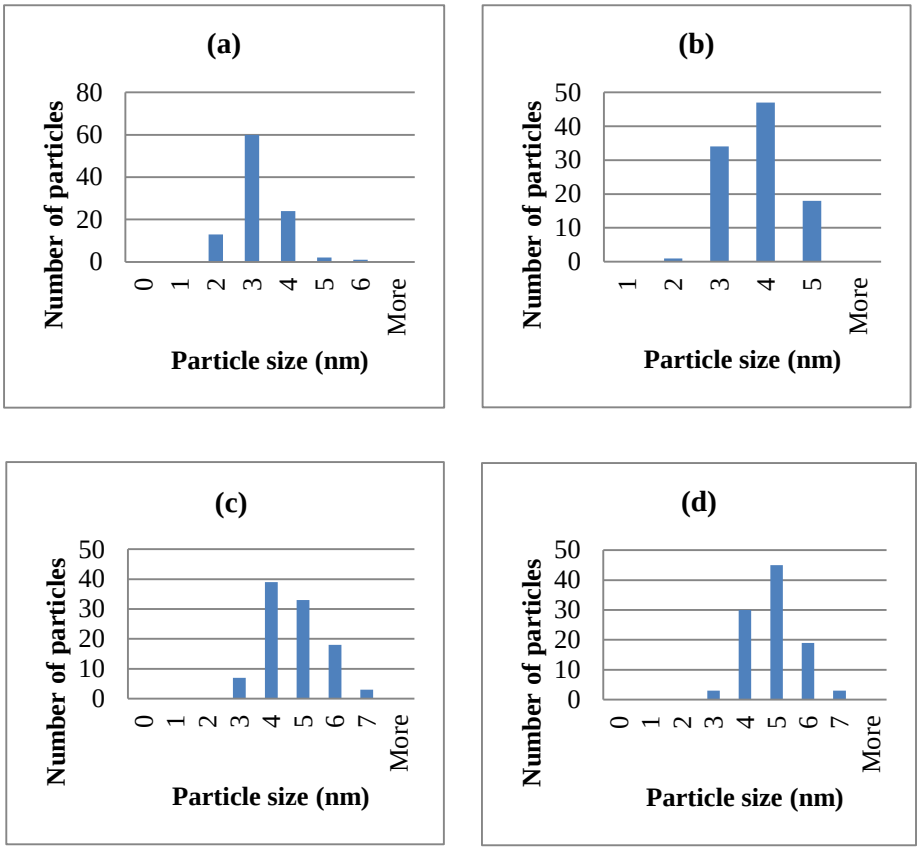

Figure 5.9: Histograms showing the particle size distribution of 100 Pt particles from Pt/C catalysts of loadings (a) 20 wt. % (b) 40 wt. % (c) 60 wt. % (d) 80 wt. %

By analysis of the particle size distribution, it is clear that the average particle size is increasing as the loading is increased. This assertion is further supported by the summary of TEM data in Table 5.5 showing the average particle size of a 100 particles. The mean particle size is increasing but not by a large amount. The results obtained are in line with what was seen from the XRD results.

Table 5.5: Summary of TEM data

	20 wt. % Pt/C (nm)	**40 wt.% Pt/C (nm)**	**60 wt.% Pt/C (nm)**	**80 wt.% Pt/C (nm)**
Mean	2.68	3.33	4.22	4.47
SD	0.640	0.662	0.953	0.836
Min	1.47	1.95	2.38	2.23
Max	5.27	4.99	6.57	6.65

It is worth noting that compared to previous studies in our group (Taylor et al., 2013) less agglomeration could be observed at the higher loadings. This is further confirmed by comparing the average particle size obtained by XRD and TEM. If agglomerates were present this would skew the volume averaged XRD data to higher values, which is not the case. Figure 5.10 shows a TEM image of a 60 wt. % Pt/C synthesized using a different reactor (Taylor et al., 2013).

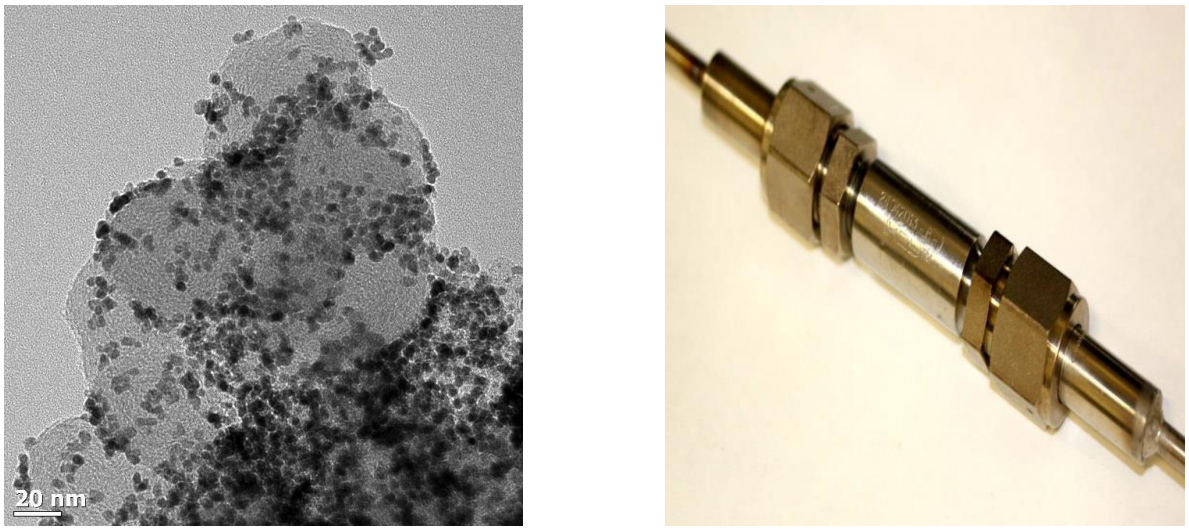

Figure 5.10: TEM image of a 60 wt. % Pt/C catalyst prepared used the reactor pictured in the image (Taylor et al., 2013)

Figure 5.10 shows clear agglomeration occurring within the surface of the catalyst. This is not seen with any of the catalysts synthesized within this report including the higher loading catalysts. This is because different reactor systems were used. The catalysts prepared for this report were made using a graphite boat inserted in a cylindrical (Stainless steel) reactor as described in Section 4 whereas the catalyst from Figure 5.10 is prepared using a metallic (Haynes alloy) tubular reactor. All other variables were kept constant, i.e. the furnace used and the amount of precursor measured. The only real difference in the reactor systems is the operating pressure of the systems. The reactor used in this report was operating at atmospheric pressure whereas the reactor shown in Figure 5.10 operates at approximately 2 bar.

5.4.3. Thermogravimetric analysis

The loading of the Pt/C catalysts was determined using TGA in air. Table 5.6 shows a summary of the TGA collected for the catalysts.

Table 5.6: TGA data collected for Pt/C catalysts.

Theoretical loading (wt. % Pt)	Actual average loading (wt. % Pt)	Loadings obtained by Tayler et al. (2013) (wt. % Pt)
20	19	18
40	36	46
60	52	59
80	64	79
80(2)	64	-

Table 5.6 shows that the TGA loading is within an acceptable range for the lower loading catalysts i.e. 20 and 40 wt. % Pt/C. However as the loading is increased the system does not reach the desired loadings. In order to test the reproducibility of the catalyst preparation system a second 80 wt. % Pt/C catalyst was prepared and the average measured TGA reading is given in the final row of Table 5.6. It shows that the catalyst preparation system makes reproducible results with regards to the catalyst loading. Compared to the study of Taylor et al. (2013), where a different reactor system was used as shown in Figure 5.10, this system gives less accurate loadings. This difference in loading may be a result of the change in operating pressure. It is possible that atmospheric pressure does not allow for efficient deposition at higher loadings. This further indicates that the reactor system plays an important role in the properties of the final catalyst.

5.4.4. Electrochemical characterisation

Figure 5.11 shows the cyclic voltammograms of the Pt/C catalysts. The corresponding ECSA data is shown in Table 5.7.

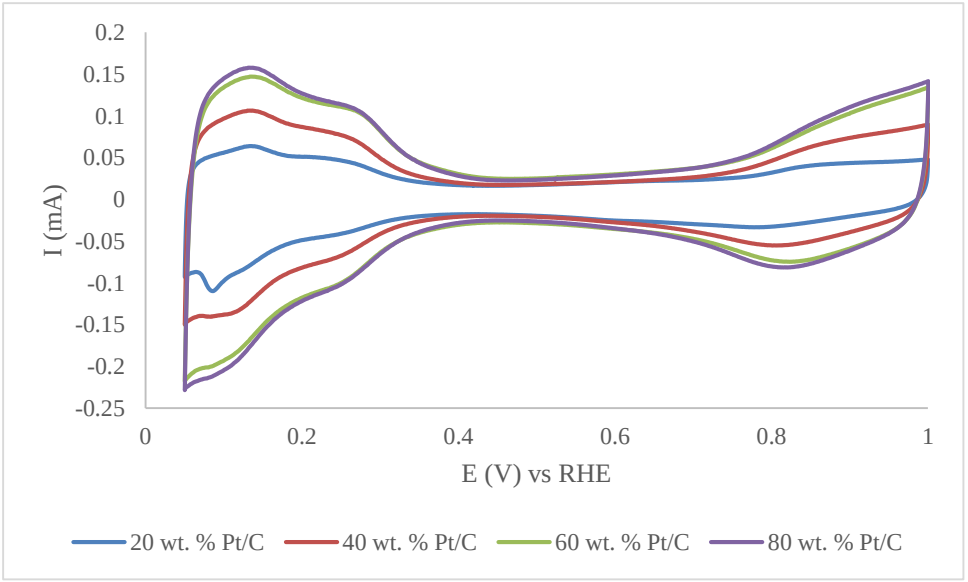

Figure 5.11: Cyclic voltammograms of Pt/C catalysts measured in an Ar saturated 0.1 M $HClO_4$ solution at a sweep rate of 50 mV/s using a 5.61 mm (OD) glassy carbon working electrode (Pine instruments, E7R9 Series).

Table 5.7: Experimental ECSA values for Pt/C catalysts

Wt. % Pt	ECSA (m^2/g_{pt})
20	46.9
40	46.5
60	43.8
80	36.1

The current measured increased as the loading was increased because the amount of Pt sites available on the carbon support increases. The ECSA values as shown in Table 5.7 decrease with an increase in loading. The trend is expected as mass the of Pt is increased from low loadings to higher loadings. Figure 5.12 below shows the CO stripping data collected for the Pt/C catalysts.

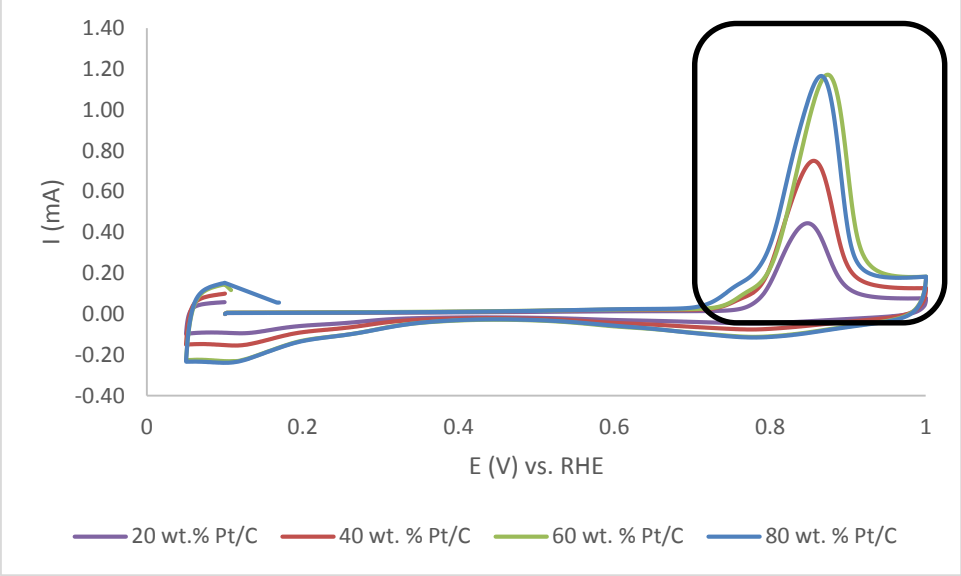

Figure 5.12: CO stripping data collected in an O_2 saturated 0.1 M $HClO_4$ solution at a sweep rate of 50 mV/s using a 5.61 mm (OD) glassy carbon working electrode (Pine instruments, E7R9 Series)

In Figure 5.12 the highlighted area between 0.7 – 0.9 V vs. RHE is the region in which we expect to observe double voltammeric peaks if the particles are agglomerating (Maillard et al., 2004). At 20 wt. % Pt there is no secondary peak. This is characteristic of a low loading catalyst because the inter-particle distance is large and no agglomeration between particles is expected. As the loading increased from 40 wt. % Pt and onwards a small secondary peak is observed at a lower potential. This indicates that some agglomeration is occurring as the inter-particle distance is decreasing. This corresponds to findings in

literature in which a secondary peak at low potential occurs as agglomeration occurs (Maillard et al., 2004). The high potential peak corresponds to isolated Pt particles.

The magnitude of the low potential peak is low indicating low levels of agglomeration. This correspond to the TEM data shown above in which not a lot of agglomeration was observed and although the particle size does increase due to agglomeration the increase is not significant.

Table 5.8 shows the CO stripping ECSA values measured. The values are larger than those calculated for cyclic voltammetry and the ratio of the two ECSA values in Table 5.8. It is expected that the CO stripping ECSA values will be larger than the CV ECSA. This is possibly because of the contribution of the capacitance of the carbon support for high surface catalysts and a change in saturation coverage with particle size (Mayrhofer et al., 2008). Additionally the 40 wt. % catalyst had the lowest ratio between the CO stripping ECSA and CV ECSA. This may be due to a particle size effect (Mayrhofer et al., 2008).

Table 5.8: CO stripping ECSA values

Wt. % Pt	CO stripping ECSA (m^2/g_{pt})	Ratio of CO stripping ECSA and CV ECSA
20	81.3	1.73
40	70.9	1.53
60	74.2	1.69
80	76.6	2.12

5.4.5. Activity of Pt/C catalysts

The rotating disk data was collected and is displayed in Figure 5.13. These curves were used to determine the diffusion limiting current and the activity of the catalysts as described in Section 4.

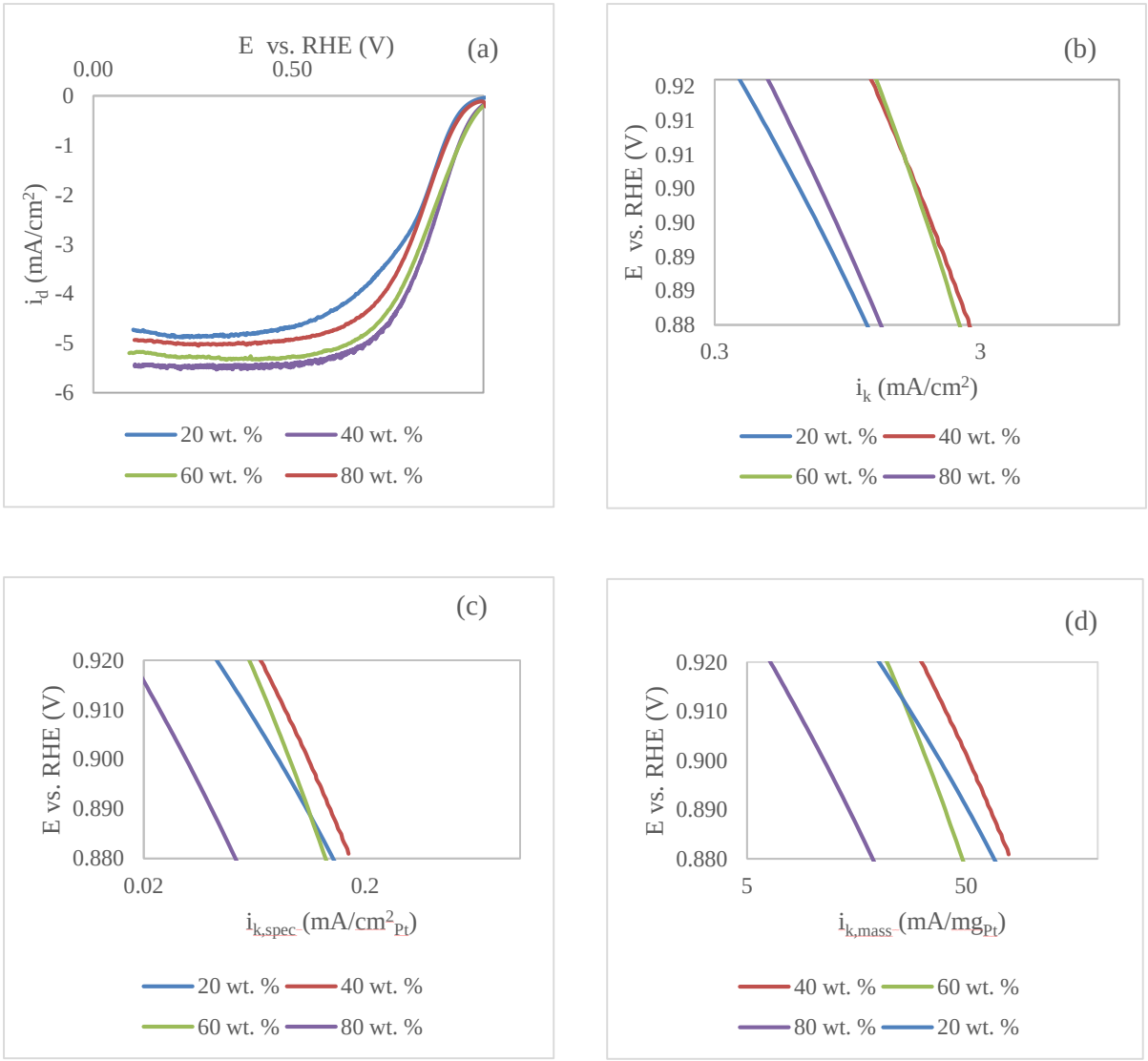

Figure 5.13: Cathodic sweep data at 1600 rpm data measured in an O_2 saturated 0.1 M $HClO_4$ solution at a sweep rate of 20 mV/s using a 5.61 mm (OD) glassy carbon working electrode (Pine instruments, E7R9 Series). (a) Rotating disk electrode curves. (b) Tafel plot showing mass transport corrected current densities (i_k) calculated using data from curves in (a). (c) Surface specific activity data corrected for Pt/C catalyst (a) Mass activity data corrected for Pt/C catalysts

The curves in Figure 5.13(a) do not reach the theoretical diffusion limiting current of 6.02 mA/cm^2. This was noted and in order to ensure once again that the system was still working properly various attempts to readjust and re-test the system were made. This included letting the O_2 bubble through the 0.1 M $HClO_4$ for longer than 30 minutes e.g. 45-60 minutes. The system was also checked for contaminants (in gases, glassware, and all solutions in contact with the system) and accounted for the effect of the quality of the catalyst film on the working electrode disk e.g. the use of a Pt disk working electrode to check the system. Some of these results are displayed in Table 5.9 below.

Table 5.9: Comparison of diffusion limiting current values of commercial catalysts and 5 mm (OD) Pt disks

	Diffusion limiting current (mA)	Diffusion limiting current (mA/cm^2)
commercial 40wt% Pt/C (1)	1.34	5.42
commercial 40wt% Pt/C (2)	1.05	4.25
commercial 40wt% Pt/C (3)	1.10	5.62
commercial 40wt% Pt/C (4)	1.08	5.53
5mm (OD) Pt disk (1)	1.10	5.64
5mm (OD) Pt disk (2)	1.00	5.12
5mm (OD) Pt disk (3)	1.14	5.83

From Table 5.9 it is clear that the theoretical limiting current is not reached however the system does get close to the theoretical value. Figure 5.13 (c) and (d) show the trends in the mass and specific activities of the catalysts and Table 5.10 shows the mass and specific activities calculated at 0.9 vs. RHE (V).

Table 5.10: Comparison of mass and surface specific activities of Pt/C catalysts at 0.9 vs. RHE (V)

Wt. % Pt	i_d (mA/cm^2)	$i_{k(0.9V)}$ (mA)	$i_{k,spec(0.9V)}$ (mA/cm^2_{Pt})	$i_{k,mass(0.9V)}$ (mA/mg_{Pt})
20	-5.17	0.199	0.092	43.4
40	-5.53	0.517	0.121	56.2
60	-5.33	0.451	0.090	32.7
80	-5.05	0.203	0.031	11.0

The surface specific activity of the 20 wt. % (Pt/C catalyst) and 60 wt. % are similar and the curves intersect. The 80 wt. % showed the lowest surface specific activity as well the lowest mass activity. The 40 wt. % shows the largest surface specific activity and mass activity. This may be due to the particle size effect. As the particles increases from low loading to high loading there is an ideal average particle size of approximately 3.33 nm coinciding with the 40 wt. % catalyst. It is difficult to extract a trend from the data however comparing the lowest loading with the highest loading there is a decrease in surface specific activity. This contradicts common literature because the expected trend is an increase in the surface specific activity with an increase in loading (Schwanitz et al., 2011). A possible explanation is that the lack of expected large agglomeration forming at higher loading. The trend in literature was seen for high loadings when agglomeration usually occurs (Fabbri et al., 2014). The lack of agglomeration affects the current measured and upsetting the expected trend. The kinetic currents

between the high and loading are comparable with each other and normally you would expect an increase in kinetic current from low to high loadings.

The mass activity overall decreases from low to high loadings with the exception of the 40 wt. % catalyst. This is the expected trend found in literature because the amount of metal is increasing as well as the particle size. Therefore there is a decrease in Pt utilisation per unit mass which leads to the trend observed.

5.4.6. Rotating ring disk results

The results from rotating ring disk experiments conducted simultaneously with the rotating disk experiments for the Pt/C catalysts are shown in Figure 5.14 below.

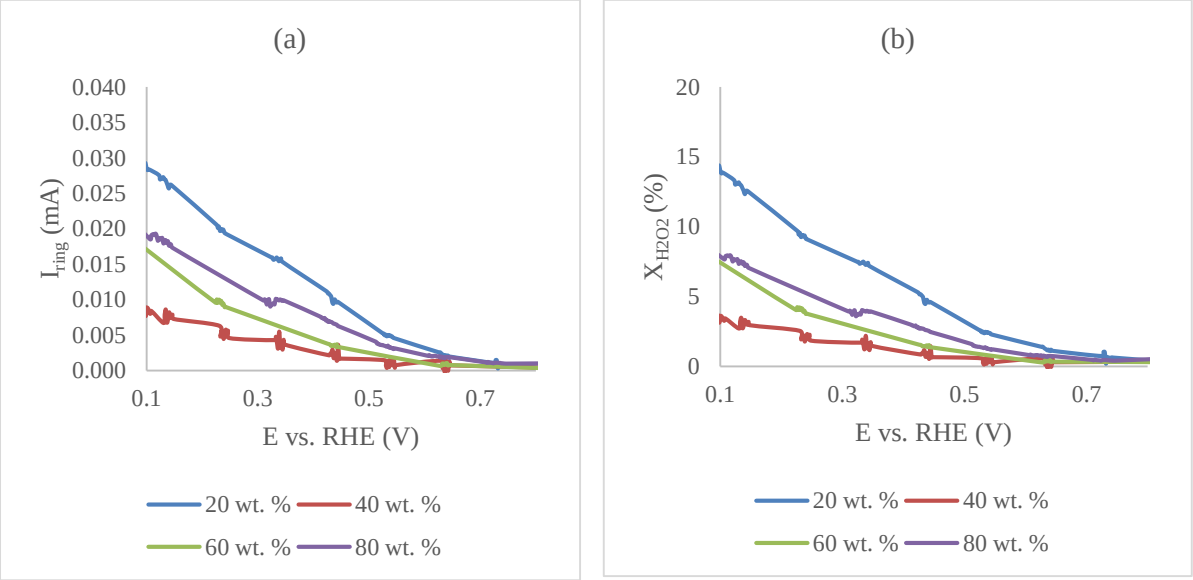

Figure 5.14: Rotating ring disk curves showing the hydrogen peroxide formation and the current collected by the ring. Results were obtained measured in an O_2 saturated 0.1 M $HClO_4$ solution at a sweep rate of 20 mV/s using a 5.61 mm working electrode (Pine instruments, E7R9 Series).

The 20 wt. % (Pt/C catalyst) showed the largest amount peroxide formation whilst the 60 and 80 wt. % had very similar hydrogen peroxide formation. The 40 wt. % had the lowest hydrogen peroxide formation. On repeated testing the 40 wt. % showed inconsistent results so reliable conclusions could not be made for this material. The expected result is more hydrogen peroxide formation at lower loadings than at higher loadings. Aside from the 40 wt. % the results follow that trend.

The high hydrogen peroxide formation at 20 wt. % supports the theory that the 2-elecron reaction pathway dominates at low loadings where there are isolated Pt nanoparticles. The H_2O_2 molecules are formed in the reaction pathway and then desorb and diffuse into the bulk solution. Since the Pt particles are isolated the H_2O_2 does not come into contact with another Pt molecule to be converted to H_2O thus reducing the efficiency of the ORR.

5.5. Analyses of the Pt_3Co/C results

The results of the physical and electrochemical characterisation conducted on the Pt alloys are detailed in this section. Analysis was conducted on the catalysts prepared using thermally induced chemical deposition at varying loadings, i.e. 20, 40, 60 and 80 wt. % Pt-Co metal. The alloys were also treated using heat treatment and leaching in 0.5 M H_2SO_4.

Physical characterisation was conducted after each treatment phase and the results are shown in this section.

5.5.1. Thermally induced chemical deposition of alloys

As detailed in Section 5.2 the metal precursors used to make the Pt alloys at varying loadings are platinum acetylacetonate ($Pt(acac)_2$) and cobalt chloride hexahydrate ($CoCl_2.6H_2O$). Initially they were prepared at 350 °C and held at that temperature for 1 hour like the Pt/C catalysts. This was done because from analysis of the TGA precursor data at this temperature both precursors should have fully decomposed, but by SEM-EDS analysis some chlorine (Cl) was still detected in the catalyst.

Therefore an investigation into the correct preparation methods to ensure the removal of chlorine was initiated. Various methods were employed to remove the chlorine. They are detailed in Table 5.11 along with their success rate determined on whether Cl was still present.

Table 5.11: Summary of Cl removal methods

Method	Comments
Acid wash of catalyst	Cl removed but some Co removed
Preparation at 350 °C for 2 hours	Cl still present
Preparation at 450 °C for 1 hour	Cl still present but at lower amounts
Preparation at 450 °C for 2 hours	No Cl

As shown in Table 5.11 an acid wash of the sample was conducted to remove the Cl. This was done by rinsing the powered catalyst at room temperature in 250 ml of 0.5 M H_2SO_4 solution and then in ultrapure water (18.2 MΩ.cm deionised water) several times. The Cl did wash out however a significant amount of Co also leached out of the sample.

Another method employed was to adjust the temperature and holding time in the furnace during the catalyst preparation. The possible conditions chosen were selected based on the aim of not increasing the holding time too much because of an assumption that the longer the holding time the more the catalyst agglomerates. Higher temperatures do not have as much of an effect on agglomeration as does the holding time on the catalyst powders. This assumption will be explained further and justified in Section 5.5.2 when we investigate the annealing conditions selected.

At 350 °C and after 2 hours, there was still Cl present, therefore a higher temperature of 450 °C and holding time of 1 hour was tested. At these conditions there was still Cl present but a reduced amount than previously observed. The holding time at 450 °C was then increased to 2 hours and analysis showed that the Cl was no longer present. Therefore the conditions for initial catalyst powder preparation was 450 °C and 2 hours.

5.5.2. Heat treatment

An intensive analysis on the effect of heat treatment on the Pt alloys was not within the scope of this report. However a short analysis was done based on the most popular heat treatment conditions found in literature. In the conditions considered the catalyst was annealed in a reducing atmosphere under the following time and temperature conditions:

- 500 °C for 4 hours (Wang et al., 2012)
- 800 °C for 7 hours (Oezeslan et al., (2012)
- 900 °C for 2 hours (Salgado et., 2004)

In the analyses only 40 wt. % Pt_3Co catalysts prepared using thermally induced chemical deposition were considered and no other loadings. This was done to reduce the variables of the system so that the results could be compared. After preparation by thermally induced chemical deposition the catalyst were heat treated using TPR as described in Section 4.

Figure 5.15 shows the TEM image and particle size distribution of a typical 40 wt. % Pt_3Co catalyst before any heat treatment.

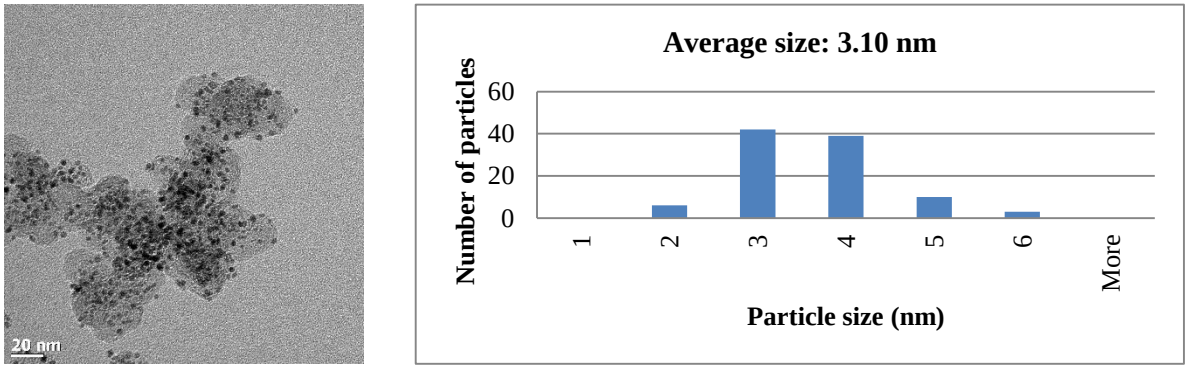

Figure 5.15: TEM image of a sample 40 wt. % Pt_3Co catalyst

The catalyst particles are homogenously spread out on the carbon support as shown by the TEM image in Figure 5.15. The particle size distribution shows that the average particle of the catalyst is between 3 – 4 nm. Figure 5.16 shows the TEM images of the 40 wt. % Pt_3Co catalyst after annealing.

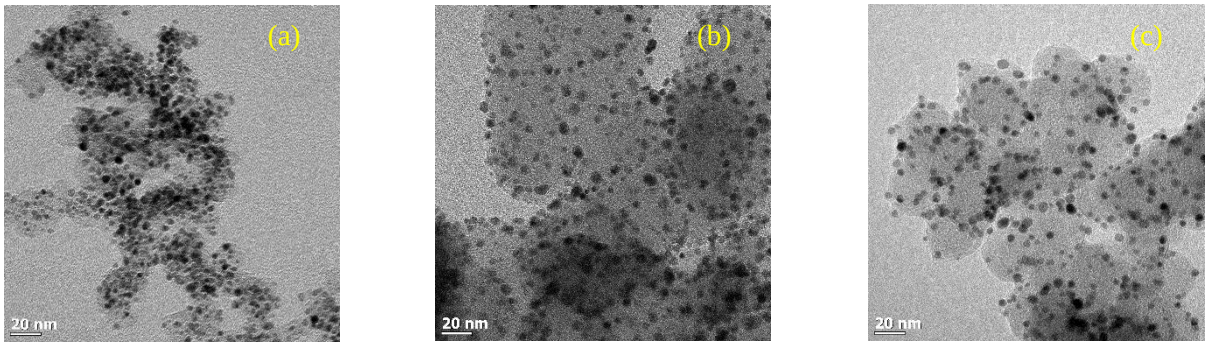

Figure 5.16: TEM images of samples after annealing in reducing atmosphere (a) 500 °C for 4 hours (b) 800 °C for 7 hours (c) 900 °C for 2 hours

From Figure 5.16 it is clear that the particles become larger after annealing. The particle growth for Figure 5.16(a) is however not as large as that of the higher temperature annealing samples. There is not a significant amount of agglomeration visible on the TEM images.

The particle size distribution of the annealed samples in shown in Figure 5.17.

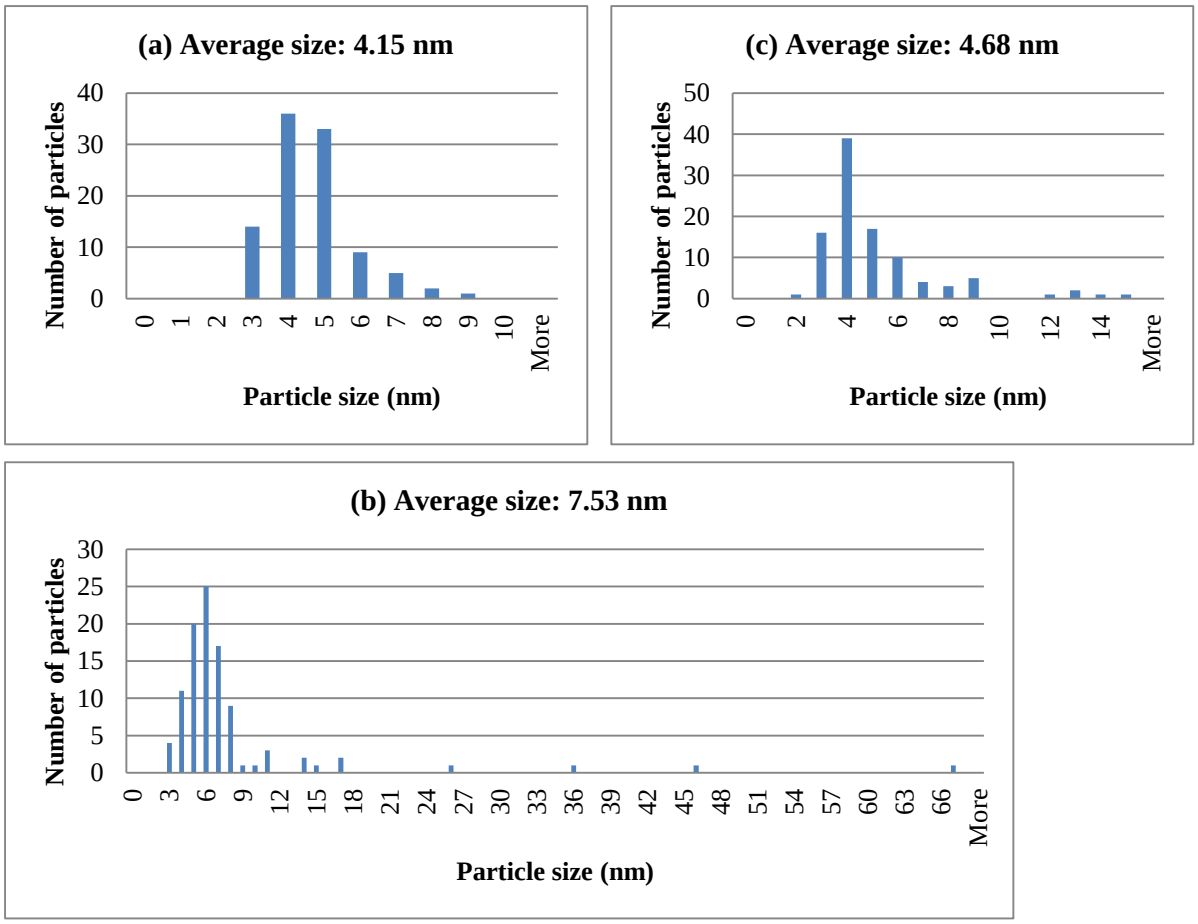

Figure 5.17: Particle size distribution of a 100 particles measured from TEM images for (a) 500 °C for 4 hours (b) 800 °C for 7 hours (c) 900 °C for 2 hours

By analysis of the particle size distribution of the annealed samples above it is clear that the lower temperature has on average a smaller particle size than the higher temperature. However, at 800 °C there is a greater presence of larger particles than at 900 °C. Since the two temperatures are comparable therefore the effect must be due to the varying holding time. The data indicates that the holding time greatly affects the amount of particle growth observed.

In order to determine the degree of alloying achieved at the varying annealing conditions XRD was used. XRD was also used to determine the average crystallite size as shown in Table 5.12.

Table 5.12: XRD average crystallite size (nm). Particle sizes calculated using the Scherrer equation.

Annealing Conditions	Average crystallite size (nm) (220)
No heat treatment	3.26
500 °C for 4 hours	2.74
800 °C for 7 hours	5.26
900 °C for 2 hours	4.96

From the XRD particle size data the samples treated at 800 °C has the highest average particle size thus in agreement with the TEM analysis. Figure 5.18 shows a comparison of the XRD curves before and after annealing at the various conditions.

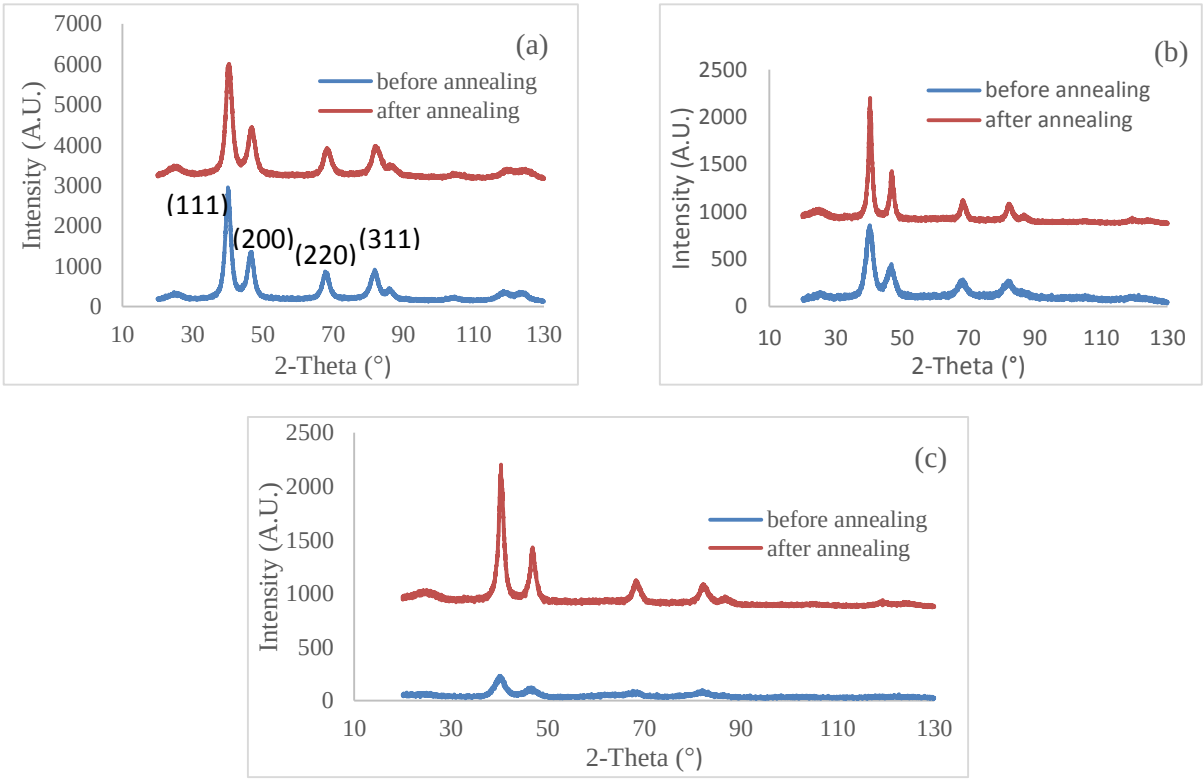

Figure 5.18:Comparison of XRD curves before and after annealing at (a) 500 °C for 4 hours (b) 800 °C for 7 hours (c) 900 °C for 2 hours

The XRD peak positions measured were within range of indexed diffraction peaks (110), (200), (220) and (311) for fcc- Pt_3Co (Schulenberg et al., 2010).There were no Co peaks observed confirming the integration of Co in Pt structure. The XRD curves above show that the peaks have shifted after treatment corresponding to a lattice contraction and the formation of an alloy as Co atoms are incorporated into the Pt lattice. The intensity of the peaks also increases indicating that the particle size increases after treatment.

The XRD curves show that there is some shift in the peaks particularly at the higher temperatures. The shift in the 500 °C peaks is not very clear. Therefore the change in lattice constants were calculated for the samples and the percent change for each annealing temperature is shown in Figure 5.19.

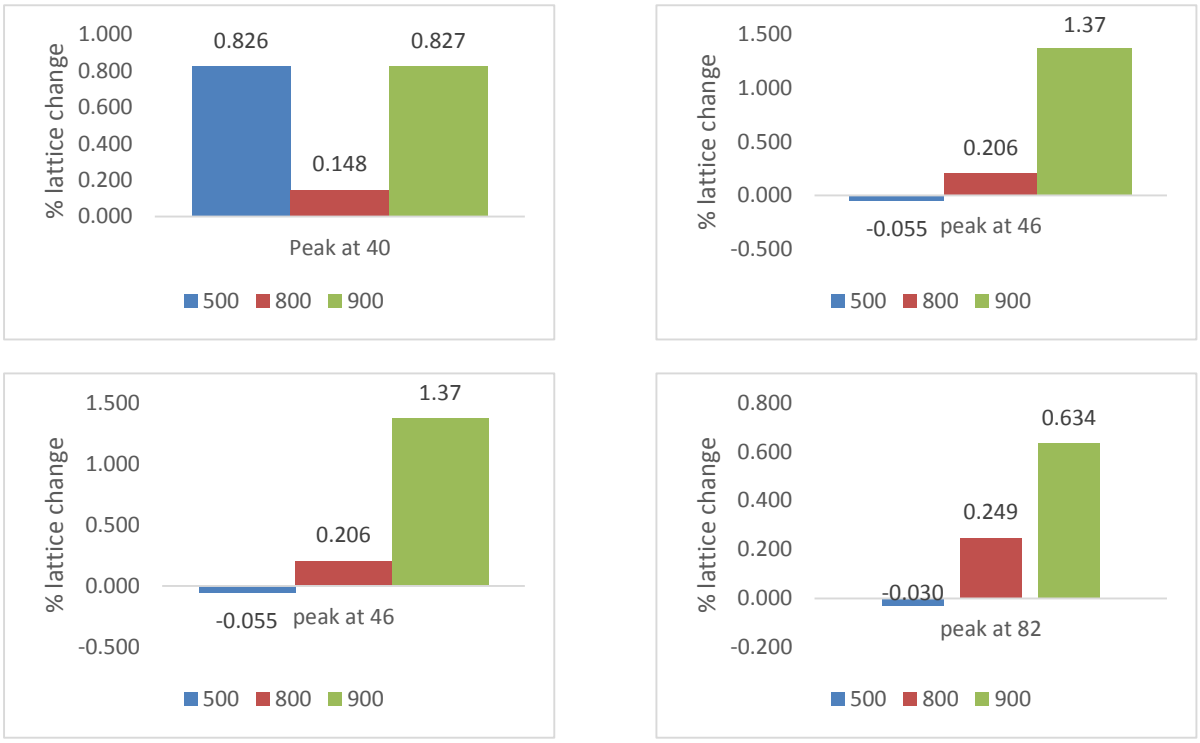

Figure 5.19: Comparison of the change in lattice constants before and after annealing at different XRD peaks

The change in lattice constants is greatest for the 900 °C indicating that this catalyst had the greatest degree of alloying. The 800 °C sample showed greater alloying than the 500 °C sample. Given that the 900 °C sample also had lower particle size data as shown by TEM particle size distribution and XRD crystallite size data, this was then the temperature used for annealing all the catalysts.

All samples where then heat treated at 900 °C followed by acid leaching to remove all unalloyed cobalt. (Gasteiger et al., 2005). The physical and electrochemical characterisation results of all materials are discussed below.

5.5.3. XRD data for heat treated and leached Pt_3Co/C

Using the Scherrer equation as described in Section 4, the particle sizes of the heat treated and leached Pt_3Co/C catalysts were calculated and the results are shown on Table 5.13.

Table 5.13: Average crystallite size (nm) of the Pt_3Co/C catalyst. Particle sizes calculated using the Scherrer equation.

Wt. % Pt_3Co	Average crystallite size from XRD (nm) Pt_3Co (220)
20	4.97
40	4.61
60	5.76
80	8.76

Figure 5.20 shows the XRD curves of the Pt alloy catalysts before and after annealing and leaching of the catalysts. The average crystallite size increased with an increase with loading which is expected. The 20 and 40 wt. % Pt_3Co/C showed very similar particle sizes with the 40 wt. % being marginally smaller. The average crystallite sizes were larger for the Pt_3Co/C catalysts than the Pt/C catalysts. This is because the Pt_3Co/C were subjected to heat treatment and leaching. Heat treatment increases the particle size as shown in Section 5.5.2.

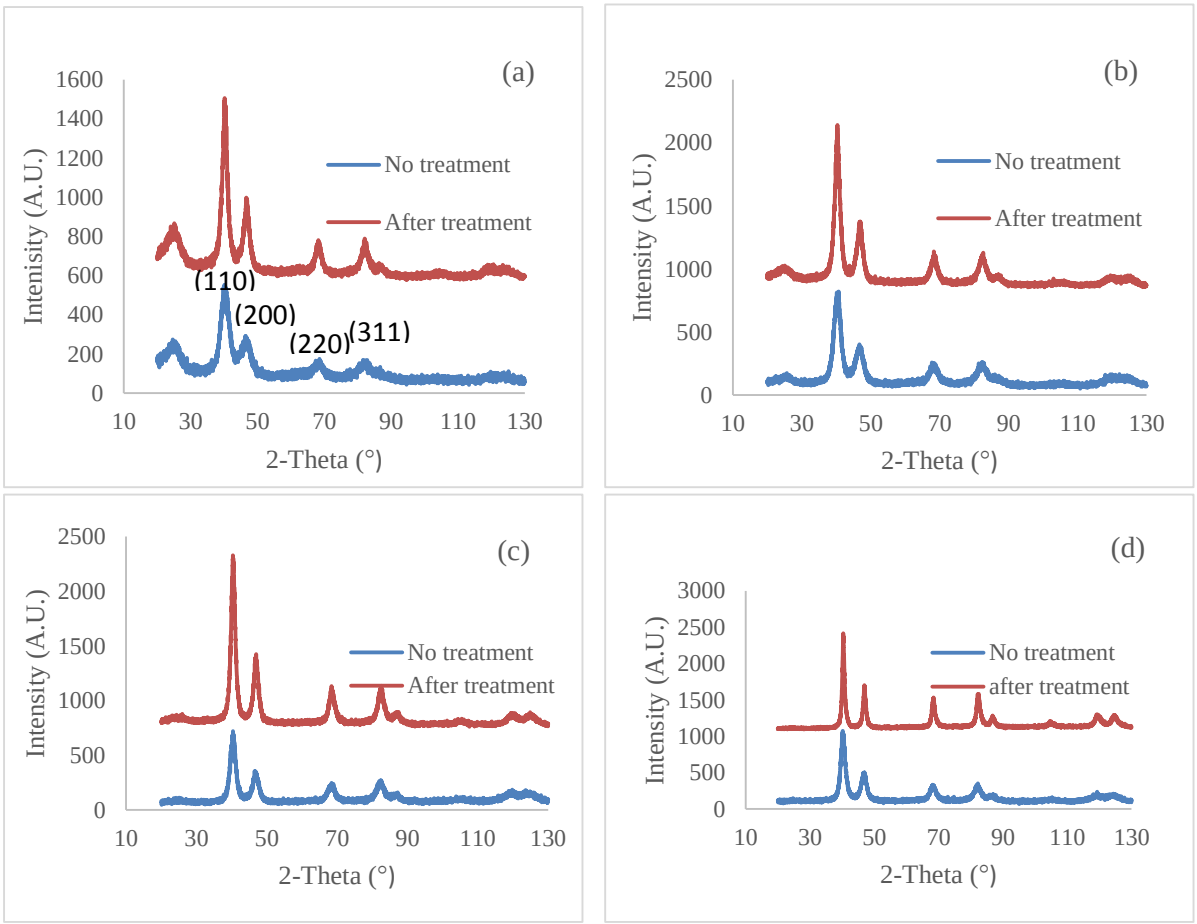

Figure 5.20: XRD curves for carbon supported Pt_3Co catalysts measured before and after treatment (annealing and leaching) (a) 20 wt. % (b) 40 wt. % (c) 60 wt. % (d) 80 wt. % Pt_3Co catalysts

The XRD peak positions measured were within range of indexed diffraction peaks (110), (200), (220) and (311) for fcc- Pt_3Co (Schulenberg et al., 2010).

The XRD curves above show that the peaks have shifted after treatment corresponding to a lattice contraction and the formation of an alloy as Co atoms are incorporated into the Pt lattice. The intensity of the peaks also increases indicating that the particle size increases after treatment.

The lattice constants for the annealed and leached samples are shown in the Table 5.14 below.

Table 5.14: Lattice constants for Pt_3Co/C catalysts

Wt. % Pt_3Co	Lattice Constants, $Pt_3Co(220)$ (Å)	Lattice Constants, $Pt_3Co(110)$ (Å)	D-spacing, $Pt_3Co(110)$ (Å)
20	3.8861	3.8839	2.2424
40	3.8798	3.8691	2.2338
60	3.8757	3.8669	2.2326
80	3.8737	3.8647	2.2313

The literature value for the lattice constant for fcc-Pt_3Co (Powder diffraction file 00-029-0499) is 3.85410 Å (Schulenberg et al., 2010). The lattice constants of the Pt_3Co (110) peaks are close to the literature value. The values of d-spacing are within range of those found in literature of 2.24 Å (Liu et al., 2008).

5.5.4. Particle size, distribution and composition via TEM and SEM

Figure 5.21 shows the TEM images of the Pt alloys after both heat treatment and leaching. Figure 5.22 shows the particle size distributions of the Pt_3Co/C catalysts after heat treatment and leaching. The TEM images and particle distributions of the untreated Pt alloys are found in Appendix A1.

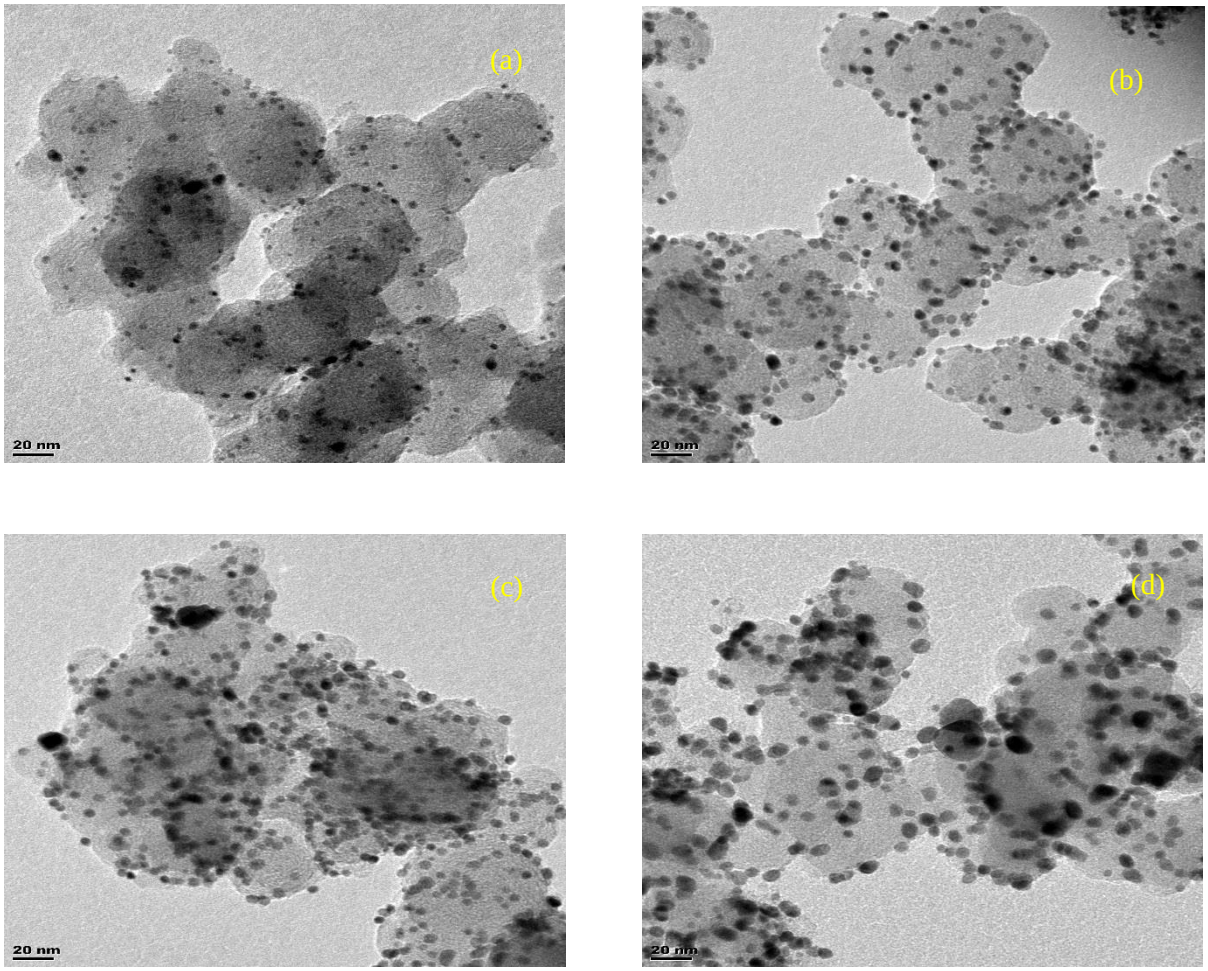

Figure 5.21: TEM images of heat treated and leached catalysts (a) 20 wt. % (b) 40 wt. % (c) 60 wt. % (d) 80 wt. % Pt_3Co catalysts

The TEM images in Figure 5.21 show that as the loading is increased the particle growth increases. There is also evidence of some agglomeration occurring. The particle size distribution is shown in Figure 5.22 . From the distribution data it is clear that the average particle size increases as the loading is increased. This is the expected trend as the loading is increased.

Even though the Pt_3Co/C catalysts were heat treated and leached the average particle sizes were relatively similar to those of the Pt/C catalysts particularly the 20 and 40 wt. % Pt_3Co/C. The higher loading Pt_3Co catalysts were larger than the Pt/C catalysts of similar loading but not by a very large margin.

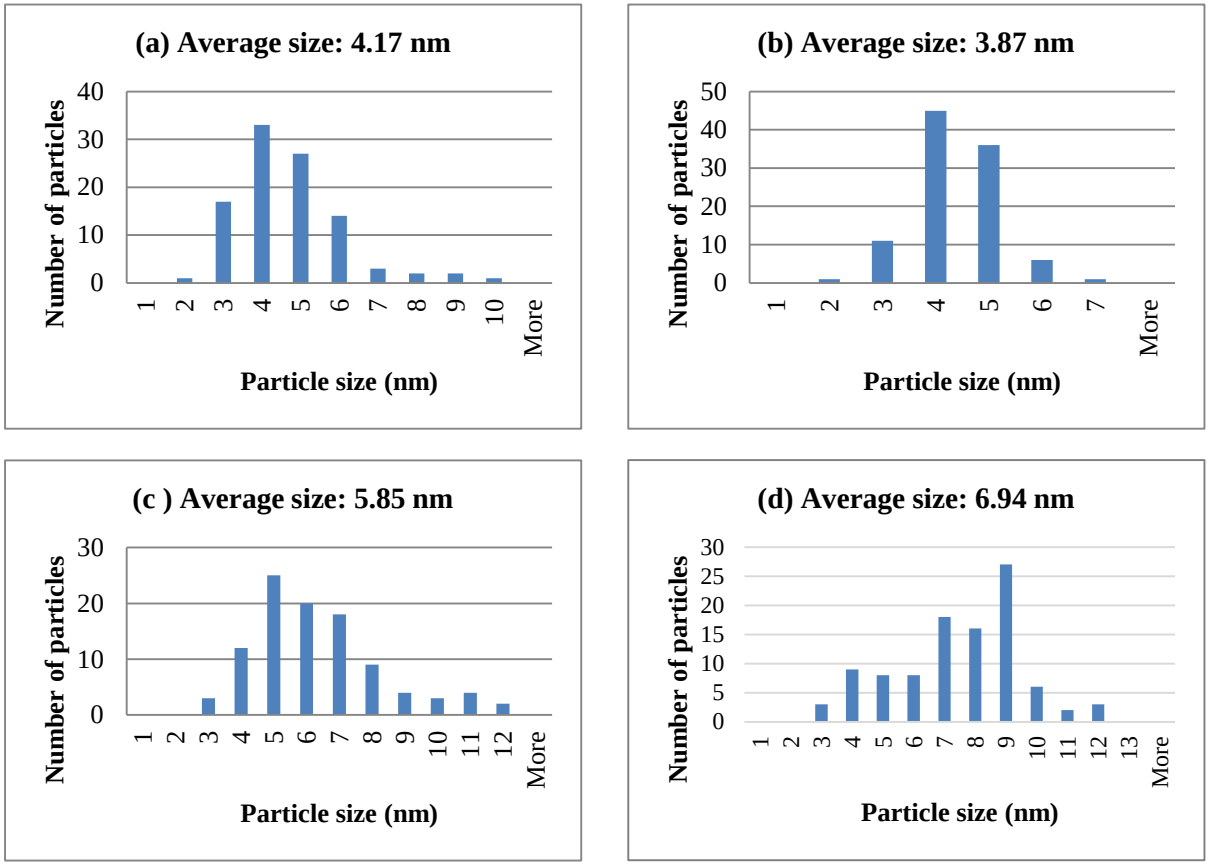

Figure 5.22: TEM particle size distribution for a 100 particles that have been heat treated and leached (a) 20 wt. % (b) 40 wt. % (c) 60 wt. % (d) 80 wt. % Pt_3Co/C catalysts

SEM-EDX was performed on the particles to get an indication of the average Pt: Co ratios. These results are shown in the Table 5.15 below:

Table 5.15: SEM-EDX values of Pt_3Co after heat treatment and leaching

Wt. % Pt_3Co	After heat treatment and leaching (Pt: Co) at. %
20	80.57 : 19.43
40	75.37 : 24.63
60	77.21 : 22.42
80	73.21 : 26.79

The SEM-EDX Pt:Co atomic % ratio is within reasonable range of the expected value of 75:25 (Pt:Co) despite the samples being heat treated and leached. Only the 20 wt. % catalyst showed a significant deviation indicating that more cobalt seem to have been leached out in that particular case.

5.5.5. Thermogravimetric analysis

The loading of the Pt_3Co/C catalysts was determined using TGA in air. Table 5.16 shows the TGA readings taken after each stage of treatment.

Table 5.16: TGA readings after each stage of treatment

Wt. % Pt_3Co	No treatment (Wt. %)	After heat treatment (Wt. %)	After leaching (Wt. %)
20	19	21	20
40	37	40	37
60	56	58	56
80	74	73	73

The TGA readings are all within a reasonable range of 10 % from the theoretical values. The values are also consistent after each stage of treatment showing the loadings were not affected by the treatments. The TGA loadings of the 60 and 80 wt. % Pt_3Co/C catalysts are closer to the expected loadings than the corresponding Pt/C catalysts. The 80 wt. % Pt_3Co/C catalyst TGA value in particular saw an increase of 10 wt. % compared to the corresponding Pt/C catalyst value of 64 wt. %.

5.5.6. Electrochemical characterisation

Figure 5.23 shows the cyclic voltammograms of the Pt_3Co/C catalysts. The corresponding ECSA data is shown in Table 5.17.

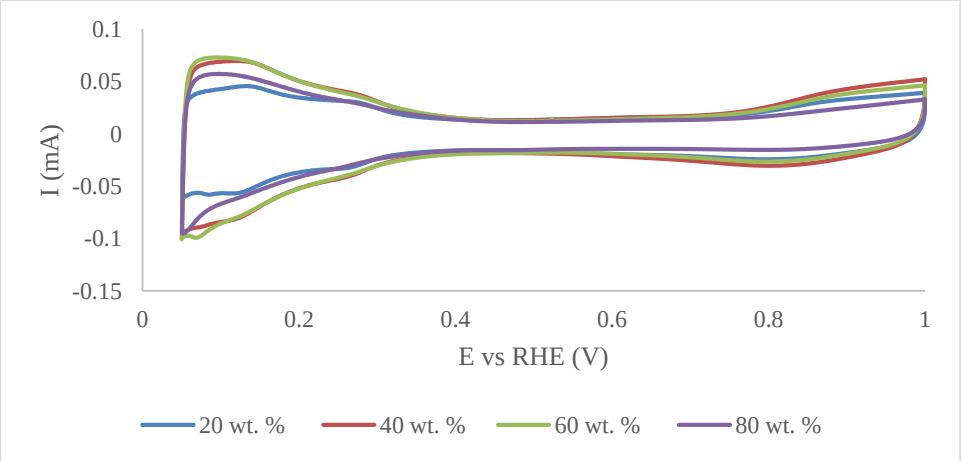

Figure 5.23: Cyclic voltammograms of Pt_3Co/C catalysts measured in an Ar saturated 0.1 M $HClO_4$ solution at a sweep rate of 50 mV/s using a 5.61 mm (OD) glassy carbon working electrode (Pine instruments, E7R9 Series).

Table 5.17: Experimental ECSA values for Pt_3Co/C catalysts

Wt. % Pt_3Co	ECSA (m^2/g_{Pt3Co})
20	32.7
40	28.2
60	19.6
80	10.9

From the data above the ECSA decreases with an increase in loading. The ECSA values are lower than that of Pt/C catalysts because there is less Pt on the carbon support surface since Co has been incorporated into the structure. Additionally the particle size is larger owing to heat treatment of the catalysts. This results in a loss of ECSA. The Figure 5.24 below shoes the Co stripping data collected.

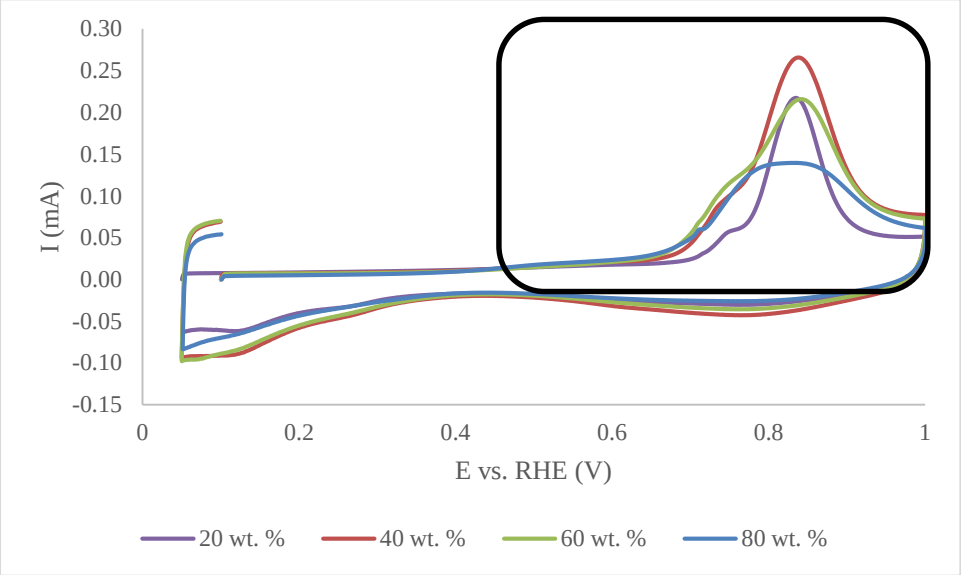

Figure 5.24: CO stripping data collected in an O_2 saturated 0.1 M $HClO_4$ solution at a sweep rate of 50 mV/s using a 5.61 mm (OD) glassy carbon working electrode (Pine instruments, E7R9 Series)

Double voltammeric peaks are seen between 0.5 – 0.9 (V) vs RHE which are characteristic of agglomeration as described in Section 2 (Maillard et al., 2004). The low potential peaks which gives an indication of agglomeration are again low however they are higher than that of Pt/C. This indicates that more agglomeration occurring for the Pt_3Co/C than the Pt/C catalysts. However the degree of agglomeration is still low despite annealing and heat treating the samples.

The ECSA calculated from CO stripping is larger than that calculated from cyclic voltammetry (CV) as is indicated from literature. The ratios of the ECSA values (CO stripping: CV) are shown in Table 5.18.

The ratio of the 80 wt. % Pt_3Co/C catalyst is the largest and close to double. The other lower loading catalysts have a similar ratio.

Table 5.18: CO stripping ECSA values

Wt. % Pt_3Co	CO stripping (m^2/g_{Pt3Co})	Ratio of CO stripping ECSA and CV ECSA
20	47.7	1.46
40	37.8	1.34
60	24.7	1.26
80	21.6	1.99

5.5.7. Activity of Pt_3Co/C catalysts

The rotating disk data was collected and is displayed in Figure 5.25. These curves were used to determine the diffusion limiting current and the activity of the catalysts as described in Section 4.

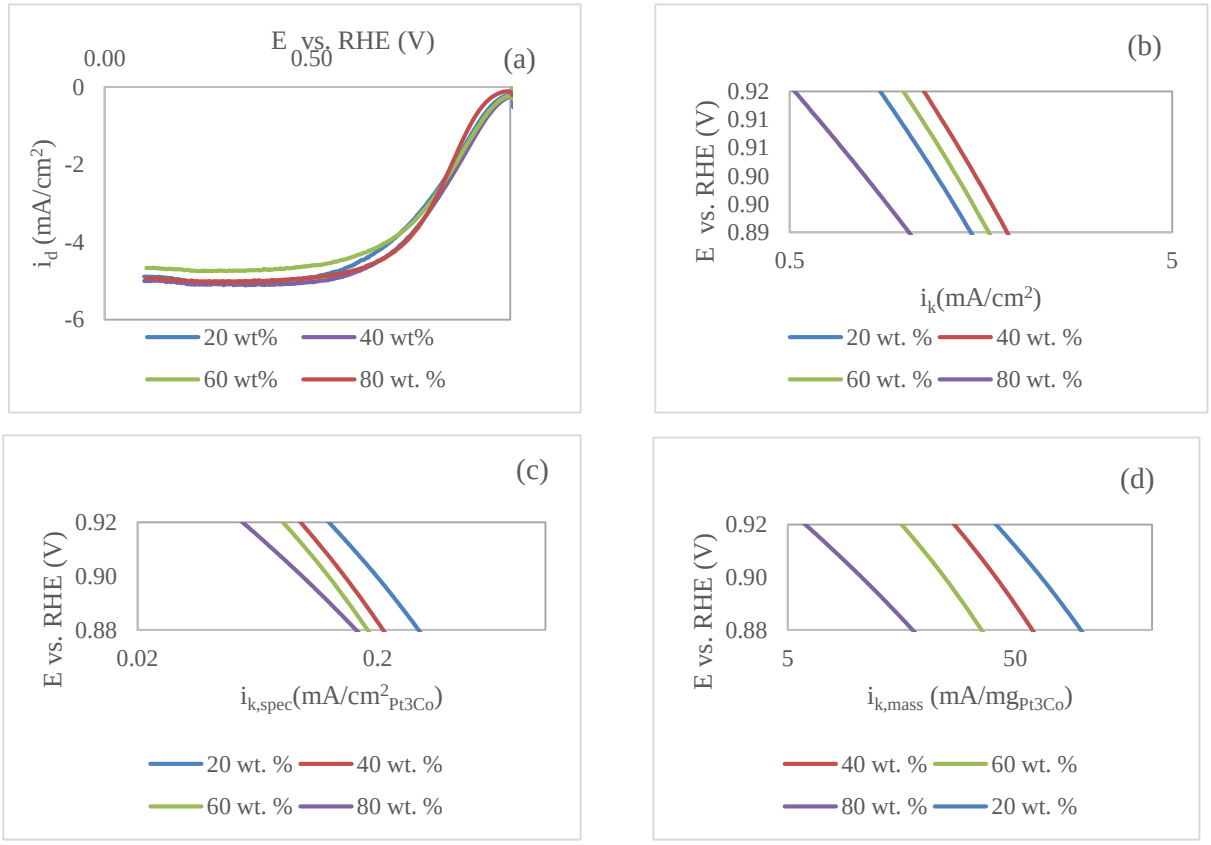

Figure 5.25: Cathodic sweep data at 1600 rpm data measured in an O_2 saturated 0.1 M $HClO_4$ solution at a sweep rate of 20 mV/s using a 5.61 mm (OD) glassy carbon working electrode (Pine instruments, E7R9 Series). (a)Rotating disk electrode curves. (b) Tafel plot showing mass transport corrected current densities (i_k) calculated using data from curves in (a). (c) Surface specific activity data corrected for Pt_3Co alloy (a) Mass activity data corrected for Pt_3Co alloy

The rotating disk electrode curves shown above indicate that the theoretical limiting current was not reached as was the case for the Pt/C catalysts. However, the limiting currents reached were similar. The mass and specific activities showed similar trends to the Pt/C catalysts. The lower loadings demonstrating higher mass and specific values. This is shown additionally in Table 5.19 where the mass and specific activities were calculated at 0.9 vs. RHE (V).

Table 5.19: Mass and Surface specific activity for cathodic sweep data of Pt_3Co/C catalysts at 0.9 vs. RHE (V) and 1600 rpm

wt.% Pt_3Co	I_d (mA/cm^2)	$i_{k(0.9\ V)}$ (mA)	$i_{k,spec(0.9\ V)}$ (mA/cm^2_{Pt3Co})	$i_{k,mass\ (0.9\ V)}$ (mA/mg_{Pt3Co})	$i_{k,spec\ (0.9\ V)}$ (mA/cm^2_{Pt})	$i_{k,mass\ (0.9\ V)}$ (mA/mg_{Pt})
20	-5.07	0.332	0.221	72.12	0.243	79.38
40	-5.11	0.409	0.158	44.53	0.174	49.02
60	-4.75	0.328	0.121	23.79	0.134	26.19
80	-5.05	0.192	0.096	10.47	0.106	11.52

Again the trend of decreasing surface specific activity is observed as the loading is increased. The Pt/C catalyst gave similar trends particularly comparing the 20 and 80 wt. % Pt/C catalysts. As explained previously in Section 5.4.5 these trends may be as a result of low particle agglomeration and therefore the morphology and catalyst structure being observed for both the Pt/C and Pt_3Co/C catalysts. This causes the current measured not to increase significantly with an increase in loading and therefore affecting the specific activity. In Table 5.19 the kinetic current of the 80 wt. % Pt_3Co/C actually decreased compared to 20 wt. % Pt_3Co/C. The surface specific activity of the Pt_3Co/C catalysts improved compared to the Pt/C catalysts. This is characteristic of alloys and literature shows that these catalysts in general perform better than their Pt/C counterparts. This will be further discussed in Section 5.6.

The mass activity showed a decrease in activity with an increase in loading as is found in literature. This is due to the reduction in Pt utilisation per unit mass as the amount of metal loading is increased. The larger particles for the higher loadings means that relatively less metal is on the surface as opposed to the bulk which then leads to lower mass activity.

5.5.8. Rotating ring disk results

Figure 5.26 shows the rotating ring disk results that were measured simultaneously with the rotating desk electrode measurements. The current collected on the ring and the H_2O_2 formation are shown in Figure 5.26.

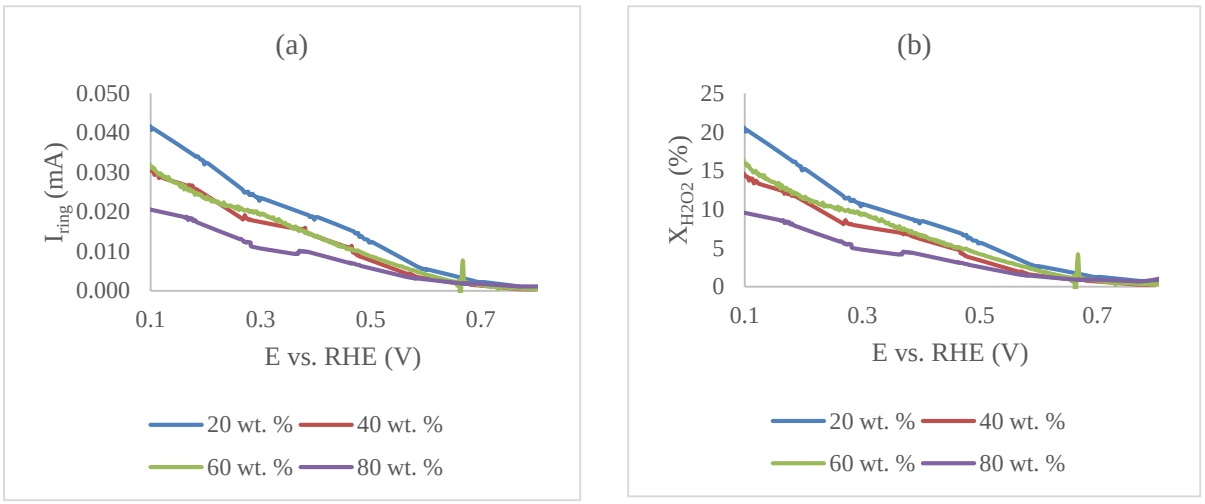

Figure 5.26: Rotating ring disk curves showing the hydrogen peroxide formation and the current collected by the ring. Results were obtained measured in an O_2 saturated 0.1 M $HClO_4$ solution at a sweep rate of 20 mV/s using a 5.61 mm working electrode (Pine instruments, E7R9 Series).

The 20 wt. % (Pt_3Co/C catalyst) gave the highest peroxide formation. The 40 wt. % and 60 wt. % gave similar H_2O_2 formation pattern which were lower than that of 20 wt. %. The 80 wt. % gave the lowest H_2O_2 formation. Compared to the Pt/C catalysts, the Pt_3Co/C give a more distinct trend in the peroxide formation. Low loadings correspond to higher peroxide formation. This can also be explained by the idea that the 2-electron process dominates at lower loadings where there are more isolated Pt/Pt_3Co particles. This phenomenon was explained in Section 5.4.6.

5.6. Summary of Pt_3Co/C and Pt/C results

The particle sizes of the Pt_3Co/C catalysts were on average larger than the Pt/C although for lower loadings (20 and 40 wt. % Metal) the particle size distribution was similar. This was observed despite the Pt_3Co/C catalysts being annealed at 900 °C and being leached.

The TGA loadings were similar at lower loadings (20 and 40 wt. %) whilst at higher loadings the wt. % loadings deviated from each other. The 80 wt. % Pt_3Co was closer to the theoretical loadings at 73 wt. % Pt_3Co than the Pt/C catalysts which gave 64 wt. % Pt. The difference between the two being 10 wt. % Metal. This indicates that the particular reactor system used seems to be more suited towards obtaining reliable loadings for alloy materials.

The CO stripping data, combined with results from TEM, showed that none of the catalysts experienced the level of agglomeration seen at comparable metal loadings with the reactor system used by Taylor et

al. (2013). This is an important finding as it shows that the reactor system and preparation method developed in this work can give access to catalyst with higher loading while limiting the level of agglomeration.

In order to compare the influence of the alloy on the activity the ratio of the surface specific and mass specific current of the Pt_3Co and Pt catalyst was calculated. An overview is given in Table 5.20.

Table 5.20: Comparison of mass and surface specific activity between Pt/C and Pt_3Co/C

Wt.% **Metal (Pt or Pt_3Co)**	**$i_{k,spec\ (0.9\ V)}$ ratio** **Pt_3Co:Pt**	**$i_{k,mass\ (0.9\ V)}$ ratio** **Pt_3Co:Pt**
20	2.40	1.66
40	1.30	0.79
60	1.35	0.73
80	3.11	0.95

From the ratios of Pt_3Co:Pt it is immediately clear that for all catalysts only when considering surface specific activity the alloy is much better with up to three times higher values obtained. This is in line with literature. The 20 wt. % and the 80 wt. % catalysts displayed the highest increases in surface specific activity (2.40 and 3.11 respectively) whilst for the intermediate loadings the increase was less and approximately 1.3.

The mass activity of the 20 wt. % showed the largest improvement while at all other loadings the mass activity showed no improvement. The mass activity result for the 80 wt. % catalyst shows that although there is less surface area due to larger particles the Pt_3Co catalysts remains as efficient per mass. This suggests that with a slightly better control on the particle size during the annealing phase, not in the scope of this work, the high loading Pt_3Co would be the most active catalyst.

Overall it can be seen that the 20 wt. % Pt_3Co loading shows the best improvement when considering the mass and surface specific activity as well the lower cost of the catalyst.

6. Conclusions

From the results discussed in Section 5 the following conclusions were drawn. The reactor system chosen plays an important role in the surface morphology of the catalysts synthesized. The reactor system developed for this work did not yield a significant amount of agglomeration of the Pt/Pt_3Co particles even at loadings as high as 70 wt. %. This is an important finding as with previous systems used in our group agglomeration was seen and therefore a system and a method has been developed to avoid agglomeration up to high loadings.

Particle growth occurred as the Pt/Pt_3Co loading was increased. The annealing of the Pt_3Co/C catalysts at 900 °C caused particle growth at higher loadings however at lower loadings the growth was minimal compared to Pt/C catalysts which were not heat treated.

The surface specific activity was improved by alloying the catalyst and leaching it. The improvement was three times larger for the 80 wt. % Pt_3Co loading and 2.64 times for the 20 wt. % Pt_3Co loading. The intermediate loadings had no significant improvement in surface specific activity between the Pt/C and Pt_3Co/C catalysts. The mass activity was not affected by alloying with the exception of the 20 wt. % Pt_3Co/C loading which outperformed its Pt/C counterpart by a factor of 1.66. Additionally the surface specific activity decreased with an increase in loading due to a lack of agglomeration as the loading was increased.

This leads to the conclusion that for alloy catalysts compared to pure Pt catalysts, intermediate loadings do not seem to be beneficial. One either needs to opt for a low loading alloy (20 wt. %) or a very high loading (80 wt. %) in order for the alloy material to exceed or equal the mass specific activity of the high loadings. Overall, from this work the 20 wt. % Pt_3Co/C catalysts showed the most favourable surface specific activity and mass activity compared to the other catalysts and utilised the least amount of Pt. Of course if mass transfer limitations might be an issue for a catalyst layer made from a low loading catalyst then the 80 wt. % Pt_3Co alloy might be a better alternative given that the particle size can be better controlled during annealing.

This leads immediately to new research questions that could be generated from this work. As just mentioned, the control of particle size during annealing for the materials prepared in this work can lead to very high surface and mass specific activities. Another important aspect is to investigate the exact differences in reaction conditions between the new reactor system developed in this work as opposed to the older, smaller and less flexible system used in previous studies.

7. References

Alia, S.M., Pylypenko, S., Neyerlin, K.C., Cullen, D.A., Kocha, S.S. & Pivovar, B.S. 2014. Platinum-Coated Cobalt Nanowires as Oxygen Reduction Reaction Electrocatalysts. ACS Catalysis. 4(8):2680-2686.

Antoine, O. & Durand, R. 2000. RRDE study of oxygen reduction on Pt nanoparticles inside Nafion®: H2O2 production in PEMFC cathode conditions. Journal of Applied Electrochemistry. 30(7):839-844.

Antolini, E., Salgado, J.R.C. & Gonzalez, E.R. 2006. The stability of Pt–M (M= first row transition metal) alloy catalysts and its effect on the activity in low temperature fuel cells: a literature review and tests on a Pt–Co catalyst. Journal of Power Sources. 160(2):957-968.

Ball, S.C., Hudson, S.L., Thompsett, D. & Theobald, B. 2007. An investigation into factors affecting the stability of carbons and carbon supported platinum and platinum/cobalt alloy catalysts during 1.2 V potentiostatic hold regimes at a range of temperatures. Journal of Power Sources. 171(1):18-25.

Borup, R., Meyers, J., Pivovar, B., Kim, Y.S., Mukundan, R., Garland, N., Myers, D., Wilson, M. et al. 2007. Scientific aspects of polymer electrolyte fuel cell durability and degradation. Chemical Reviews. 107(10):3904-3951.

Carlton, C.E., Chen, S., Ferreira, P.J., Allard, L.F. & Shao-Horn, Y. 2012. Sub-nanometer-resolution elemental mapping of “Pt3Co” nanoparticle catalyst degradation in proton-exchange membrane fuel cells. The Journal of Physical Chemistry Letters. 3(2):161-166.

Che, G., Lakshmi, B.B., Martin, C.R., Fisher, E.R. & Ruoff, R.S. 1998. Chemical Vapor Deposition Based Synthesis of Carbon Nanotubes and Nanofibers Using a Template Method. Chemistry of Materials. 10(1):260-267.

Chen, S., Sheng, W., Yabuuchi, N., Ferreira, P.J., Allard, L.F. & Shao-Horn, Y. 2008. Origin of oxygen reduction reaction activity on “Pt3Co” nanoparticles: atomically resolved chemical compositions and structures. The Journal of Physical Chemistry C. 113(3):1109-1125.

Choi, S., Lee, S., Kim, W.Y., Choi, R., Hong, K., Nam, K.M., Han, S.W. & Park, J.T. 2012. Composition-Controlled PtCo Alloy Nanocubes with Tuned Electrocatalytic Activity for Oxygen Reduction. ACS Applied Materials & Interfaces. 4(11):6228-6234.

Christ, J.M., Neyerlin, K.C., Wang, H., Richards, R. & Dinh, H.N. 2014. Impact of Polymer Electrolyte Membrane Degradation Products on Oxygen Reduction Reaction Activity for Platinum Electrocatalysts. Journal of the Electrochemical Society. 161(14):F1481-F1488.

Chu, H.P., Lei, L., Hu, X. & Yue, P. 1998. Metallo-Organic Chemical Vapor Deposition (MOCVD) for the Development of Heterogeneous Catalysts. Energy & Fuels. 12(6):1108-1113.

Climent, V. & Feliu, J.M. 2011. Thirty years of platinum single crystal electrochemistry. Journal of Solid State Electrochemistry. 15(7-8):1297-1315.

Collman, J.P. & Decreau, R.A. 2008. Functional biomimetic models for the active site in the respiratory enzyme cytochrome c oxidase. Chemical Communications. (41):5065-5076.

Colón-Mercado, H.R. & Popov, B.N. 2006. Stability of platinum based alloy cathode catalysts in PEM fuel cells. Journal of Power Sources. 155(2):253-263.

Debe, M.K., Schmoeckel, A.K., Vernstrom, G.D. & Atanasoski, R. 2006. High voltage stability of nanostructured thin film catalysts for PEM fuel cells. Journal of Power Sources. 161(2):1002-1011.

Dicks, A. L. 2006. The role of carbon in fuel cells. Journal of Power Sources. 156(2): 128-141.

Fabbri, E., Taylor, S., Rabis, A., Levecque, P., Conrad, O., Kötz, R. & Schmidt, T.J. 2014. The Effect of Platinum Nanoparticle Distribution on Oxygen Electroreduction Activity and Selectivity. Chemcatchem.

Gan, L., Heggen, M., O'Malley, R., Theobald, B. & Strasser, P. 2013. Understanding and controlling nanoporosity formation for improving the stability of bimetallic fuel cell catalysts. Nano Letters. 13(3):1131-1138.

Gancs, L., Kobayashi, T., Debe, M.K., Atanasoski, R. & Wieckowski, A. 2008. Crystallographic Characteristics of Nanostructured Thin-Film Fuel Cell Electrocatalysts: A HRTEM Study. Chemistry of Materials. 20(7):2444-2454.

Gasteiger, H.A., Kocha, S.S., Sompalli, B. & Wagner, F.T. 2005. Activity benchmarks and requirements for Pt, Pt-alloy, and non-Pt oxygen reduction catalysts for PEMFCs. Applied Catalysis B: Environmental. 56(1–2):9-35.

Gray, J.E. & Luan, B. 2002. Protective coatings on magnesium and its alloys — a critical review. Journal of Alloys and Compounds. 336(1–2):88-113.

Grimmer, C., Schenk, A., Pichler, B.E., Perchthaler, M. & Hacker, V. 2013. Manufacturing and Stabilization of PtCo/C Cocatalysts for PEM Fuel Cells. ECS Transactions. 58(1):753-759.

Gummalla, M., Ball, S.C., Condit, D.A., Rasouli, S., Yu, K., Ferreira, P.J., Myers, D.J. & Yang, Z. 2015. Effect of Particle Size and Operating Conditions on Pt3Co PEMFC Cathode Catalyst Durability. Catalysts. 5(2):926-948.

Haile, S.M. 2003. Fuel cell materials and components. Acta Materialia. 51(19):5981-6000.

Hierso, J., Feurer, J.R. & Kalck, P. 2000. Platinum and Palladium Films Obtained by Low-Temperature MOCVD for the Formation of Small Particles on Divided Supports as Catalytic Materials. Chemistry of Materials. 12(2):390-399.

Hitchcock, A.P., Berejnov, V., Lee, V., West, M., Colbow, V., Dutta, M. & Wessel, S. 2014. Carbon corrosion of proton exchange membrane fuel cell catalyst layers studied by scanning transmission X-ray microscopy. Journal of Power Sources. 266(0):66-78.

Holton, O.T. & Stevenson, J.W. 2013. The Role of Platinum in Proton Exchange Membrane Fuel Cells. United Kingdom: Johnson Matthey.

Huang, H. & Wang, X. 2014. Recent progress on carbon-based support materials for electrocatalysts of direct methanol fuel cells. Journal of Materials Chemistry A. 2(18):6266-6291.

Huang, Y., Garcia, M., Habib, S., Shui, J., Wagner, F.T., Zhang, J., Jorne, J. & Li, J.C.M. 2014. Dealloyed PtCo hollow nanowires with ultrathin wall thicknesses and their catalytic durability for the oxygen reduction reaction. Journal of Materials Chemistry A. 2(38):16175-16180.

Hwang, S.J., Kim, S., Lee, J., Lee, S., Jang, J.H., Kim, P., Lim, T., Sung, Y. et al. 2012. Role of Electronic Perturbation in Stability and Activity of Pt-Based Alloy Nanocatalysts for Oxygen Reduction. Journal of the American Chemical Society. 134(48):19508-19511.

Jayasayee, K., Veen, J.A.R., Manivasagam, T.G., Celebi, S., Hensen, E.J.M. & de Bruijn, F.A. 2012. Oxygen reduction reaction (ORR) activity and durability of carbon supported PtM (Co, Ni, Cu) alloys: Influence of particle size and non-noble metals. Applied Catalysis B: Environmental. 111–112(0):515-526.

Jeon, M.K. & McGinn, P.J. 2012. Co-alloying effect of Co and Cr with Pt for oxygen electro-reduction reaction. Electrochimica Acta. 64(0):147-153.

Jia, Q., Caldwell, K., Strickland, K., Ziegelbauer, J.M., Liu, z., Yu, Z., Ramaker, D.E. & Mukerjee, S. 2014. Improved Oxygen Reduction Activity and Durability of Dealloyed PtCox Catalysts for Proton Exchange Membrane Fuel Cells: Strain, Ligand, and Particle Size Effects. ACS Catalysis. 5(1):176-186.

Jourdan, M., Mounir, H. & El Marjani, A. 2014. Compilation of factors affecting durability of Proton Exchange Membrane Fuel Cell (PEMFC). Renewable and Sustainable Energy Conference (IRSEC), 2014 International. 17-19 Oct. 2014. IEEE. 542-547.

Koh, S., Toney, M.F. & Strasser, P. 2007. Activity–stability relationships of ordered and disordered alloy phases of Pt3Co electrocatalysts for the oxygen reduction reaction (ORR). Electrochimica Acta. 52(8):2765-2774.

Larsen, M.J. & Skou, E.M. 2012. ESR, XPS, and thin-film RRDE characterization of nano structured carbon materials for catalyst support in PEM fuel cells. Journal of Power Sources. 202(0):35-46.

Lebedeva, M.V., Pierron-Bohnes, V., Goyhenex, C., Papaefthimiou, V., Zafeiratos, S., Nazmutdinov, R.R., Da Costa, V., Acosta, M. et al. 2013. Effect of the chemical order on the electrocatalytic activity of model PtCo electrodes in the oxygen reduction reaction. Electrochimica Acta. 108(0):605-616.

Li, L., Linping, H., Jin, L. & Zidong, W. 2015. Enhanced stability of Pt nanoparticle electrocatalysts for fuel cells. Nano Research. 8(2):418-440.

Litster, S. & McLean, G. 2004. PEM fuel cell electrodes. Journal of Power Sources. 130(1–2):61-76.

Loukrakpam, R., Luo, J., He, T., Chen, Y., Xu, Z., Njoki, P.N., Wanjala, B.N., Fang, B. et al. 2011. Nanoengineered PtCo and PtNi Catalysts for Oxygen Reduction Reaction: An Assessment of the Structural and Electrocatalytic Properties. The Journal of Physical Chemistry C. 115(5):1682-1694.

Maillard, F., Schreier, S., Hanzlik, M., Savinova, E.R., Weinkauf, S. & Stimming, U. 2005. Influence of particle agglomeration on the catalytic activity of carbon-supported Pt nanoparticles in CO monolayer oxidation. Physical Chemistry Chemical Physics. 7(2):385-393.

Maillard, F., Dubau, L., Durst, J., Chatenet, M., André, J. & Rossinot, E. 2010. Durability of Pt3Co/C nanoparticles in a proton-exchange membrane fuel cell: Direct evidence of bulk Co segregation to the surface. Electrochemistry Communications. 12(9):1161-1164.

Mani, P., Srivastava, R. & Strasser, P. 2011. Dealloyed binary PtM3 (M = Cu, Co, Ni) and ternary PtNi3M (M = Cu, Co, Fe, Cr) electrocatalysts for the oxygen reduction reaction: Performance in polymer electrolyte membrane fuel cells. Journal of Power Sources. 196(2):666-673.

Markiewicz, M., Zalitis, C. & Kucernak, A. 2015. Performance measurements and modelling of the ORR on fuel cell electrocatalysts – the modified double trap model. Electrochimica Acta. (0):1-6.

Mayrhofer, K.J.J., Strmcnik, D., Blizanac, B.B., Stamenkovic, V.R., Arenz, M. & Markovic, N.M. 2008. Measurement of oxygen reduction activities via the rotating disc electrode method: From Pt model surfaces to carbon-supported high surface area catalysts. Electrochimica Acta. 53(7):3181-3188.

Min, M., Cho, J., Cho, K. & Kim, H. 2000. Particle size and alloying effects of Pt-based alloy catalysts for fuel cell applications. Eletrochimica Acta. 45:4211-4217.

Murkerjee, S. & Srinivasan, S. 1993. Enhanced electrocatalysis of oxyegen reduction on platinum alloys in proton exchange fuel cells. Journal of Electroanalytical Chemistry. 357:201-224.

Norskov, J.K., Rossmeisl, J., Logadottir, A. & Lindqvist, L. 2004. Origin of the Overpotential for Oxygen Reduction at a Fuel-Cell Cathode. Journal of Physical Chemistry. 108:17886-17892.

Oezaslan, M., Hasché, F. & Strasser, P. 2012. Oxygen electroreduction on PtCo3, PtCo and Pt3Co alloy nanoparticles for alkaline and acidic PEM fuel cells. Journal of the Electrochemical Society. 159(4):B394-B405.

Oezaslan, M. & Strasser, P. 2011. Activity of dealloyed PtCo3 and PtCu3 nanoparticle electrocatalyst for oxygen reduction reaction in polymer electrolyte membrane fuel cell. Journal of Power Sources. 196(12):5240-5249.

Okaya, K., Yano, H., Kakinuma, K., Watanabe, M. & Uchida, H. 2012. Temperature Dependence of Oxygen Reduction Reaction Activity at Stabilized Pt Skin-PtCo Alloy/Graphitized Carbon Black Catalysts Prepared by a Modified Nanocapsule Method. ACS Applied Materials & Interfaces. 4(12):6982-6991.

Omura, J., Yano, H., Tryk, D.A., Watanabe, M. & Uchida, H. 2014. Electrochemical Quartz Crystal Microbalance Analysis of the Oxygen Reduction Reaction on Pt-Based Electrodes. Part 2: Adsorption of Oxygen Species and ClO4– Anions on Pt and Pt–Co Alloy in HClO4 Solutions. American Chemical Society. 30(1):432-439.

Paddison, S.J. & Gasteiger, H.A. 2013. PEM Fuel Cells, Materials and Design Development Challenges. In Fuel Cells. K. Klaus-Dieter & R.A. Meyer, Eds. New York: Springer. 341-367.

Paulus, U.A., Wokaun, A., Scherer, G.G., Schmidt, T.J., Stamenkovic, V., Markovic, N.M. & Ross, P.N. 2002. Oxygen reduction on high surface area Pt-based alloy catalysts in comparison to well defined smooth bulk alloy electrodes. Eletrochimica Acta. 47:3787-3798.

Paulus, U.A., Schmidt, T.J., Gasteiger, H.A. & Behm, R.J. 2001. Oxygen reduction on a high-surface area Pt/Vulcan carbon catalyst: a thin-film rotating ring-disk electrode study. Journal of Electroanalytical Chemistry. 495(2):134-145.

Pedersen, C.M., Escudero-Escribano, M., Velázquez-Palenzuela, A., Christensen, L.H., Chorkendorff, I. & Stephens, I.E.L. 2015. Benchmarking Pt-based electrocatalysts for low temperature fuel cell reactions with the rotating disk electrode: oxygen reduction and hydrogen oxidation in the presence of CO (review article). Electrochimica Acta. (0)

Pozio, A., De Francesco, M., Cemmi, A., Cardellini, F. & Giorgi, L. 2002. Comparison of high surface Pt/C catalysts by cyclic voltammetry. Journal of Power Sources. 105(1):13-19.

Rabis, A., Rodriguez, P. & Schmidt, T.J. 2012. Electrocatalysis for Polymer Electrolyte Fuel Cells: Recent Achievements and Future Challenges. -ACS Catalysis. (-5):864-890.

Rabis, A., Rodriguez, P. & Schmidt, T.J. 2012. Electrocatalysis for polymer electrolyte fuel cells: recent achievements and future challenges. Acs Catalysis. 2(5):864-890.

Ren, B., Yao, J.L., She, C.X., Huang, Q.J. & Tian, Z.Q. 2004. Surface Raman Spectroscopy Techniques on Transition Metals. The Internet Journal of Vibrational Spectroscopy. 4.

Salgado, J.R.C., Antolini, E. & Gonzalez, E.R. 2005. Carbon supported Pt–Co alloys as methanol-resistant oxygen-reduction electrocatalysts for direct methanol fuel cells. Applied Catalysis B: Environmental. 57(4):283-290.

Schulenburg, H., Durst, J., Müller, E., Wokaun, A. & Scherer, G. 2010. Real surface area measurements of Pt 3 Co/C catalysts. Journal of Electroanalytical Chemistry. 642(1):52-60.

Schwanitz, B., Rabis, A., Horisberger, M., Scherer, G. & Schmidt, T. 2011. Particle size effect on magnetron sputtered cathodes. Paul Scherer Institut.

Shao, Y., Yin, G. & Gao, Y. 2007. Understanding and approaches for the durability issues of Pt-based catalysts for PEM fuel cell. Journal of Power Sources. 171(2):558-566.

Shinozaki, K., Hatanaka, T. & Morimoto, Y. 2007. Pt utilization analysis using CO adsorption. ECS Transactions. 11(1):497-507.

Sinha, P.K., Gu, W., Kongkanand, & Thompson, E. 2011. Performance of Nano Structured Thin Film (NSTF) Electrodes under Partially-Humidified Conditions. Journal of the Electrochemical Society. 158(7):B831-B840.

Spanos, I., Rellán, C.P., Altmann, L., Bäumer, M. & Arenz, M. 2014. PtxCo1−x alloy NPs prepared by colloidal tool-box synthesis: The effect of de-alloying on the oxygen reduction reaction activity. International Journal of Hydrogen Energy. 39(17):9143-9148.

Stamenkovic, V., Mun, B.S., Mayrhofer, K.J.J., Ross, P.N., Markovic, N.M., Rossmeisl, J., Greeley, J. & Norskov, J.K. 2006. Changing the Activity of Electrocatalysts for Oxygen Reduction by Tuning the Surface Electronic Structure. Angewandte Chemie International Edition. 45:2897-2901.

Stephens, I.E., Bondarenko, A.S., Grønbjerg, U., Rossmeisl, J. & Chorkendorff, I. 2012. Understanding the electrocatalysis of oxygen reduction on platinum and its alloys. Energy & Environmental Science. 5(5):6744-6762.

Studebaker, D.B., Neumayer, D.A., Hinds, B.J., Stern, C.L. & Marks, T.J. 2000. Encapsulating Bis (β-Ketoiminato) Polyethers. Volatile, Fluorine-Free Barium Precursors for Metal-Organic Chemical Vapor Deposition. Inorganic Chemistry. 39(15):3148-3157.

Sun, S., Zhang, G., Geng, D., Chen, Y., Li, R., Cai, M. & Sun, X. 2011. A highly durable platinum nanocatalyst for proton exchange membrane fuel cells: multiarmed starlike nanowire single crystal. Angewandte Chemie. 123(2):442-446.

Tabet-Aoul, A. & Mohamedi, M. 2012. Interrelated functionalities of hierarchically CNT/CeO2/Pt nanostructured layers: synthesis, characterization, and electroactivity. Physical Chemistry Chemical Physics. 14:4463–4474.

Trasatti, S. & Petrii, O.A. 1991. Real Surface Area Measurements in Electrochemistry. International Union of Pure and Applied Chemistry. 63:711-734.

U.S. Department of Energy 2015. U.S. Department of Energy. Available: http://energy.gov/sites/prod/files/2014/02/f8/fctt_roadmap_june2013.pdf.

van der Vliet, D., Wang, C., Debe, M., Atanasoski, R., Markovic, N.M. & Stamenkovic, V.R. 2011. Platinum-alloy nanostructured thin film catalysts for the oxygen reduction reaction. Electrochimica Acta. 56(24):8695-8699

Wakisaka, M., Morishima, S., Tryk, D.A., Uchida, H. & Watanabe, M. 2014. (Invited) Enhanced Activities for the Oxygen Reduction Reaction at Pt-Skin Layers on Pt-Co Alloy Single-Crystal Electrodes. ECS Transactions. 64(3):75-79.

Wang, C., Chi, M., Li, D., Strmcnik, D., van der Vliet, D., Wang, G., Komanicky, V., Chang, K. et al. 2011. Design and Synthesis of Bimetallic Electrocatalyst with Multilayered Pt-Skin Surfaces. -Ournal of the American Chemical Society. 133(36):14396-14403.

Wang, C., Chi, M., Li, D., van der Vliet, D., Wang, G., Lin, Q., F. Mitchell, J., More, K.L. et al. 2011. Synthesis of homogeneous Pt-bimetallic nanoparticles as highly efficient electrocatalysts. Acs Catalysis. 1(10):1355-1359.

Wang, C., Markovic, N.M. & Stamenkovic, V.R. 2012 (2). Advanced platinum alloy electrocatalysts for the oxygen reduction reaction. ACS Catalysis. 2(5):891-898.

Wang, C., Wang, G., van der Vliet, D., Chang, K., Markovic, N.M. & Stamenkovic, V.R. 2010. Monodisperse Pt3Co nanoparticles as electrocatalyst: the effects of particle size and pretreatment on electrocatalytic reduction of oxygen. Physical Chemistry Chemical Physics. 12(26):6933- 6939.

Wang, D., Xin, H.L., Hovden, R., Wang, H., Yu, Y., Muller, D.A., DiSalvo, F.J. & Abruña, H.D. 2013. Structurally ordered intermetallic platinum–cobalt core–shell nanoparticles with enhanced activity and stability as oxygen reduction electrocatalysts. Nature Materials. 12(1):81-87.

Wang, Y., Wilkinson, D.P. & Zhang, J. 2011. Noncarbon support materials for polymer electrolyte membrane fuel cell electrocatalysts. Chemical Reviews. 111(12):7625-7651.

Wang, Y., Wilkinson, D.P. & Zhang, J. 2011. Noncarbon support materials for polymer electrolyte membrane fuel cell electrocatalysts. Chemical Reviews. 111(12):7625-7651.

Wang, H., Yuan, X. & Li, H. Eds. 2012 (1). Pem fuel cell diagnostic tools. United States of America: CRC Press.

Wang, H., Yuan, X., Li, D. & Gu, X. 2012. Dendritic PtCo alloy nanoparticles as high performance oxygen reduction catalysts. Journal of Colloid and Interface Science. 384(1):105-109.

Wang, Y., Chen, K.S., Mishler, J., Cho, S.C. & Adroher, X.C. 2011. A review of polymer electrolyte membrane fuel cells: Technology, applications, and needs on fundamental research. Applied Energy. 88(4):981-1007.

Wu, J., Yuan, X.Z., Martin, J.J., Wang, H., Zhang, J., Shen, J., Wu, S. & Merida, W. 2008. A review of PEM fuel cell durability: Degradation mechanisms and mitigation strategies. Journal of Power Sources. 184(1):104-119.

Wu, J., Yuan, X.Z., Wang, H., Blanco, M., Martin, J.J. & Zhang, J. 2008. Diagnostic tools in PEM fuel cell research: Part I Electrochemical techniques. International Journal of Hydrogen Energy. 33(6):1735-1746.

Xu, Z., Zhang, H., Zhong, H., Lu, Q., Wang, Y. & Su, D. 2012. Effect of particle size on the activity and durability of the Pt/C electrocatalyst for proton exchange membrane fuel cells. Applied Catalysis B: Environmental. 111–112(0):264-270.

Yin, Z., Hu, T., Wang, J., Wang, C., Liu, Z. & Guo, J. 2014. Preparation of highly active and stable polyaniline-cobalt-carbon nanotube electrocatalyst for oxygen reduction reaction in polymer electrolyte membrane fuel cell. Electrochimica Acta. 119(0):144-154.

Yuan, X., Li, H., Zhang, S., Martin, J. & Wang, H. 2011. A review of polymer electrolyte membrane fuel cell durability test protocols. Journal of Power Sources. 196(22):9107-9116.

Yue, Q., Zhang, K., Chen, X., Wang, L., Zhao, J., Liu, J. & Jia, J. 2010. Generation of OH radicals in oxygen reduction reaction at Pt–Co nanoparticles supported on graphene in alkaline solutions. Chemical Communications. 46(19):3369-3371.

Zhang, J. Ed. 2008. PEM Fuel Cell Electrocatalysts and Catalyst Layers. London: Springer.

Zhang, S., Shao, Y., Yin, G. & Lin, Y. 2013. Recent progress in nanostructured electrocatalysts for PEM fuel cells. Journal of Materials Chemistry A. 1(15):4631-4641. [22 April 2014].

Zhang, S., Yuan, X., Wang, H., Mérida, W., Zhu, H., Shen, J., Wu, S. & Zhang, J. 2009. A review of accelerated stress tests of MEA durability in PEM fuel cells. International Journal of Hydrogen Energy. 34(1):388-404

Zhao, X., Chen, S., Fang, Z., Ding, J., Sang, W., Wang, Y., Zhao, J., Peng, Z. et al. 2015. Octahedral Pd@ Pt1. 8Ni Core-Shell Nanocrystals with Ultrathin PtNi Alloy Shells as Active Catalysts for Oxygen Reduction Reaction. Journal of the American Chemical Society.

8. Appendices

A1. TEM analysis of Pt_3Co/C catalyst

The TEM images of the Pt_3Co/C catalyst before any treatment.

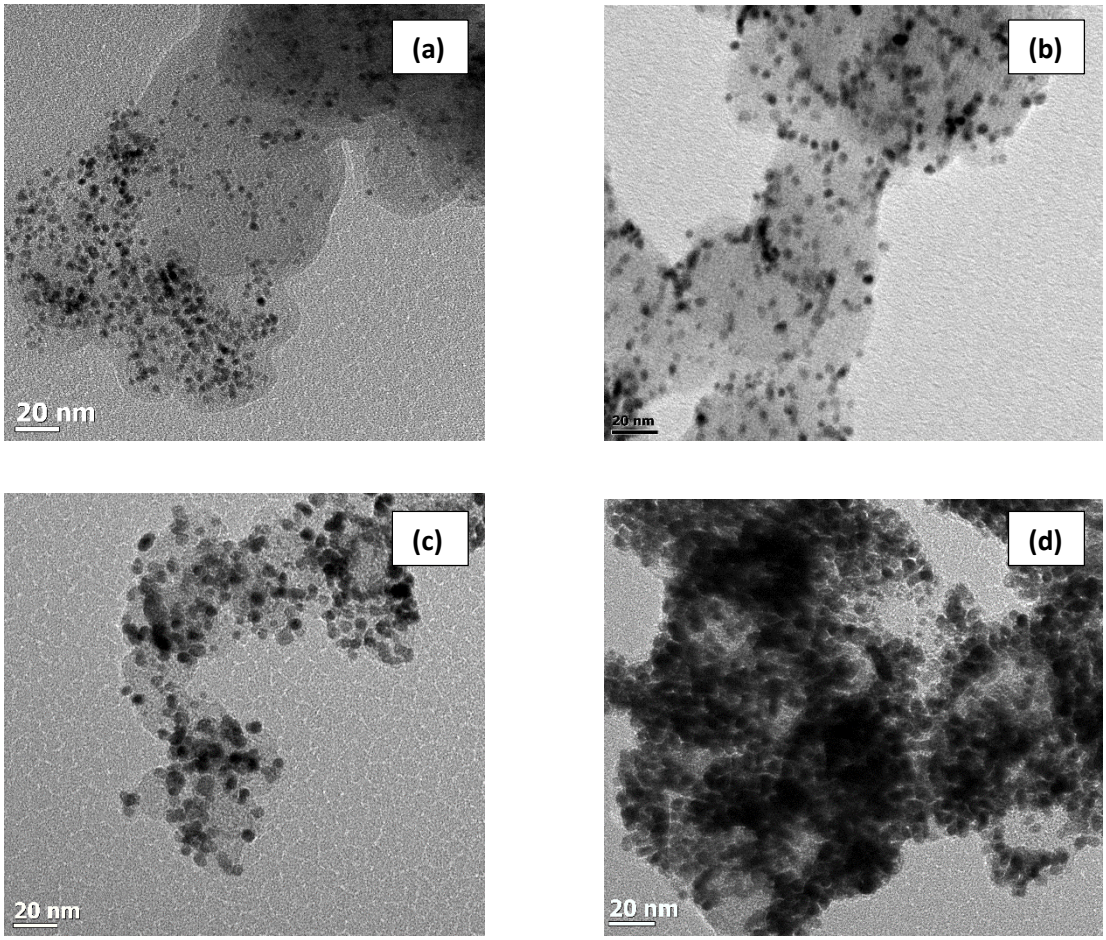

Figure 8.1: TEM images of Pt_3Co/C catalysts with no treatment (a) 20 wt. % (b) 40 wt. % (c) 60 wt. % (d) 80 wt. %

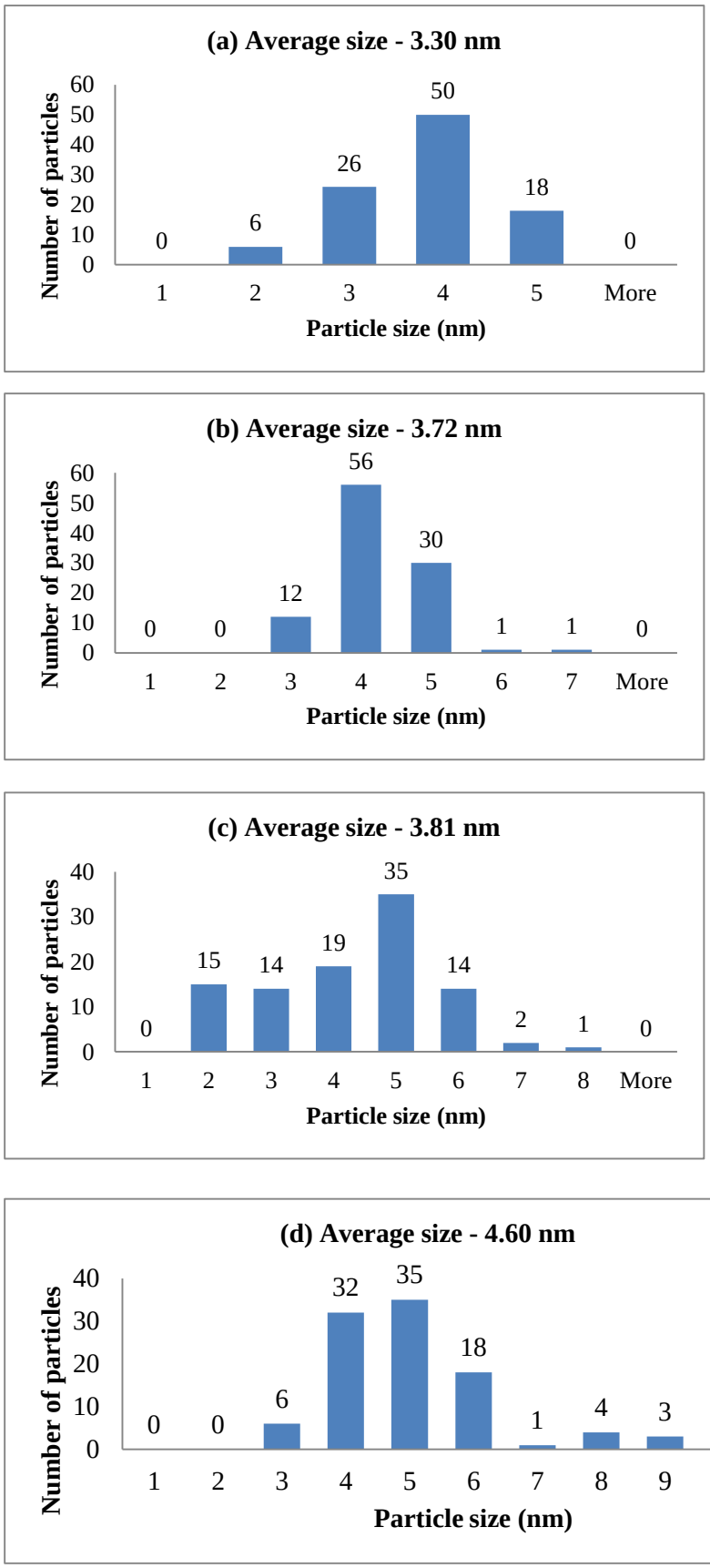

Figure 8.2: Particle size distribution of Pt_3Co/C catalyst before treatment